CHARACTERIZATION AND COMPARISON OF PIEZOELECTRIC MATERIALS FOR TRANSDUCING POWER FROM A THERMOACOUSTIC ENGINE

By

ANDREW BRIAN EVANS WEKIN

A thesis submitted in partial fulfillment of
the requirements for the degree of

MASTER OF SCIENCE IN MECHANICAL ENGINEERING

WASHINGTON STATE UNIVERSITY
School of Mechanical and Materials Engineering

AUGUST 2008

To the Faculty of Washington State University:

The members of the Committee appointed to examine the thesis of ANDREW BRIAN EVANS WEKIN find it satisfactory and recommend that it be accepted.

_____
Chair

_____

_____

ACKNOWLEDGEMENT

I would like to thank Dr. Cill Richards for her help and patience over the past two years as my advisor and mentor. I would also like to thank the other members of my committee for all of their help: Dr. Konstantin Matveev and Dr. Michael Anderson. I would like to thank all of my colleagues who have helped with this research especially: John Youngsman, Hamzeh Bardhaweel, Najmeddin Shafiei-Tehrany, HoKi Lee, Leland Weiss, Jeong Cho, and Michelle Robinson. I would also like to thank my family for all of their support.

CHARACTERIZATION AND COMPARISON OF PIEZOELECTRIC MATERIALS FOR TRANSDUCING POWER FROM A THERMOACOUSTIC ENGINE

Abstract

by Andrew Brian Evans Wekin, M.S.
Washington State University
August 2008

Chair: Cecilia D. Richards

There is a growing need for small, reliable sources of electric power. A piezoelectric transducer coupled to a small scale thermoacoustic engine has the potential of producing high density power in a compact, lightweight system with no moving parts. The goal of this study is to identify and characterize some potential piezoelectric transducers for use in this thermoacoustic piezoelectric system.

Four piezoelectric transducers are presented which represent a range of stiffness and electromechanical properties. All samples are tested to characterize their electrical and mechanical parameters and then driven by an acoustic device, or sound tube, over a range of frequencies and acoustic pressures to determine the operating conditions for maximum power output. One open and one closed standing wave thermoacoustic engine is also employed to generate power with each sample and these results are shown to correlate with the power output data from the sound tube. All results are tabulated to facilitate prediction of power output for any sample under given conditions.

For open conditions, the most compliant sample has the highest power output. The 12x20mm PVDF (polyvinylidene fluoride) sample generates 12 μW on the open

sound tube at a resonant frequency of 140 Hz with an acoustic pressure of 38.2 Pa RMS. This sample has an electromechanical coupling k^2 of 0.0014, a mechanical Q of 16.84, a stiffness of 15.5 N/m and a power density of 250 W/m^3.

For closed conditions, the sample with the highest coupling has the highest power output. On the closed sound tube, the 15mm diameter PZT (lead zirconate titanate) disk generates 2.22 μW at a resonant frequency of 1500 Hz, with an acoustic pressure of 38.2 Pa RMS and an acoustic to electric efficiency of 17.2%. This sample has an electromechanical coupling k^2 of 0.0319, a mechanical Q of 4.9137, a stiffness of 11600 N/m and a power density of 122.8 W/m^3. This sample also generates the most power from the closed thermoacoustic engine: 177 μW at 470 Hz and 796 Pa RMS.

The results show that mechanical Q is significantly lower for closed conditions for all samples; coupling coefficient k^2 is higher for the closed conditions for the PZT disk and the PVDF samples but lower for the other samples; and the stiffness, resonant frequency, and damping of all samples are significantly higher in the closed conditions.

TABLE OF CONTENTS

Page

LIST OF FIGURES

LIST OF TABLES

Dedication

I would like to dedicate this work to Jori. She is the most amazing person I know; she is a wonderful wife, an incredible mother, my best friend and my confidante. Without her encouragement and assistance, this would not have been possible. Thank you for motivating me to attempt this and thank you for allowing me the time to accomplish it. I dedicate my life's work to you.

CHAPTER 1

INTRODUCTION

1.1 Motivation for Thermoacoustic Piezoelectric System

As more systems contain electronic components, the need to supply those electrical components with reliable electric power is of paramount importance. For many applications, those systems may be embedded or remote and so conventional sources of electric power are less viable. Batteries are often toxic and have a limited life, fuel powered generators are often complex and prone to failure, while other sources of power such as photovoltaic don't have the power density to supply enough power in a small enough package. For applications such as embedded electronics, remote sensors, and spacecraft, there exists a need for power generation in a small, robust package. The main benefits of an electric power generator consisting of a thermoacoustic engine coupled to a piezoelectric element are the following: small size, light weight, no moving parts and no toxic chemicals. A thermoacoustic engine can extract waste heat or solar heat and generate an intense acoustic vibration which can then be turned into useful electrical power with a piezoelectric element.

1.2 Thermoacoustic Effect

1.2.1 History of Thermoacoustic Effect

Sound waves have both pressure and temperature oscillations. In most audible sounds, temperature fluctuations are so small as to be difficult to measure and considered much smaller than the mean value. Under certain conditions, however, the temperature

gradient and the geometry conspire to create powerful heat-sound interactions, leading to thermoacoustic phenomena.

One of the earliest recordings of the thermoacoustic effect was in 1850 when Sondhauss recorded an effect that glassblowers had noticed [1.1, 1.2]. When a hot piece of glass came in contact with a cool glass tube with one open, it produced a pure tone. The frequency of the sound produced corresponded with the natural frequency of the tube. These Sondhauss tubes or singing glass tubes were not much more than a curious natural phenomenon. Then in 1859 Rijke discovered that sound was produced by hot gauze when it was located in the lower half of an open-ended vertical tube [1.3]. Sound oscillations were greatest when the hot gauze was positioned one quarter of the distance from the bottom of the tube. It was postulated that the sound was caused because of the expansion of air at the gauze and the subsequent contraction of the air as it cooled toward the top of the tube. However, this hypothesis couldn't sufficiently explain the magnitude of the oscillations. Soon after these discoveries were reported, Lord Rayleigh proposed a qualitative description to explain the thermoacoustic instabilities which cause these phenomena: "If heat be given to the air at the moment of greatest condensation, or be taken from it at the moment of greatest rarefaction, the vibration is encouraged. On the other hand, if heat be given at the moment of greatest rarefaction, or abstracted at the moment of greatest condensation, the vibration is discouraged." [1.4]

All of these findings were from experiments and the explanations were empirical and qualitative in nature. It wasn't until Rott made quantitative calculations in the 1960s that the phenomena became better understood and engineers began to attempt to harness these effects for commercial application [1.5, 1.6, 1.7].

1.2.2 Classifications of Thermoacoustic Systems

Thermoacoustic systems can be broadly viewed in two groups: engines (or prime movers) and refrigerators (or heat pumps) as seen in Figure 1.2.1.

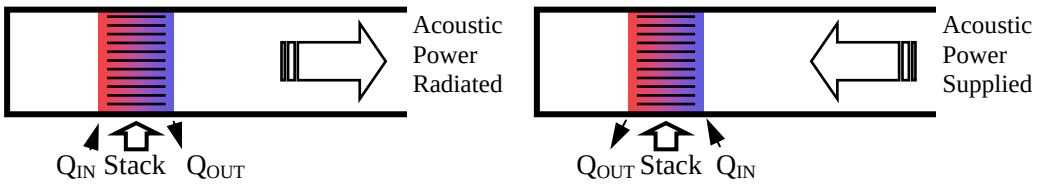

Figure 1.2.1 Thermoacoustic engine and refrigerator

In a thermoacoustic engine, a temperature differential is maintained across the stack. This creates pressure oscillations which radiate from the stack and manifest as sound waves. In a thermoacoustic refrigerator, sound or pressure waves are pushed across the stack. This moves heat from one side of the stack to the other, effectively cooling one side of the stack. This is equivalent to a heat pump.

Both types of thermoacoustic systems can also be operated by a standing wave or a more complex traveling wave. The standing wave thermoacoustic engine is the simplest type and it can be a completely closed chamber (closed-closed) or open at one end (closed-open) as seen in Figure 1.2.2.

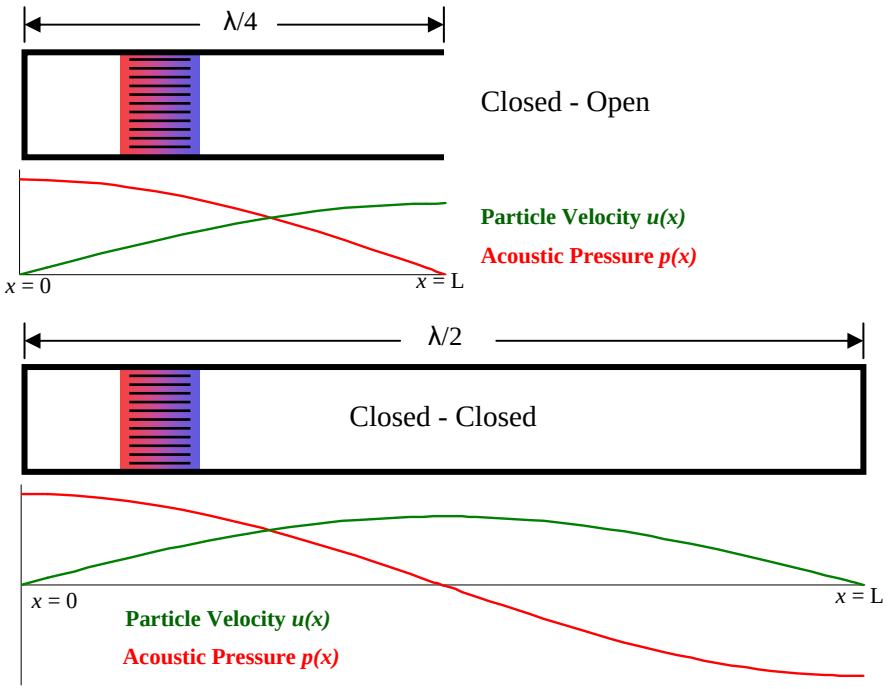

Figure 1.2.2 Open and closed standing wave engines

Below each engine shown in Figure 1.2.2 there is a qualitative graph of the particle velocity and the acoustic pressure of the standing wave within the engine. Note that at the open end there is a pressure release so pressure is minimized and particle velocity is at a maximum. This corresponds to the conditions found at the middle (x/2) of the closed engine.

The traveling wave thermoacoustic engine consists of a closed loop and is based on the Stirling cycle as seen in Figure 1.2.3 [1.8]. The traveling wave type is more complicated than the standing wave, but has the advantage of being more efficient.

Figure 1.2.3 Traveling wave thermoacoustic engine [1.8]

The field of thermoacoustics has made major advances in the past 20 years. Large scale commercial refrigeration has been developed with thermoacoustic technology [1.9, 1.10]. Also, the efficiency limitations inherent in the simple standing wave engines have been addressed by construction of closed loop traveling wave engines on the scale of meters producing 1kW of acoustic power [1.11]. The large size of this engine has also been shown to scale well to a scale of centimeters producing 100W acoustic power. This meso-scale thermoacoustic engine has an overall length of 16cm and weighs 900g [1.12, 1.13]. Most of the work done with thermoacoustics has been done at the large or medium scale. Recently there has been an interest in miniaturizing thermoacoustic refrigerators and due to the higher frequencies involved in a smaller resonating chamber, traditional linear motors lose efficiency and require increasing input power. This has driven research in piezoelectric drivers for small scale thermoacoustic refrigerators [1.14, 1.15].

1.2.3 Efforts to Transduce Electric Power from Acoustic Power

There are some projects to date which transduce electric power from a thermoacoustic prime mover including some which operate with a magnetohydrodynamic

(liquid metal) transducer [1.16]. A project coupling a thermoacoustic engine to a linear electric alternator was designed and built by Los Alamos National Laboratory to be sent into space with NASA [1.17, 1.18, 1.19]. This consists of a traveling wave engine with an efficiency of 30%. The device measures 25cm long and produces 100W electrical power. Another well documented project to produce electric power from a thermoacoustic engine is the master's thesis of Mark Telesz [1.20]. This project is based on the design from LANL [1.17] but is designed to produce 100 Watts of electrical power at 20% thermal to electrical efficiency. The engine itself is quite compact with an overall length of 16 inches. However, the electric generators which are coupled to the engine are quite large in comparison. Two linear alternators (motors) are used for vibration balancing each of which is 102mm in diameter and 81mm long without piston and weighs 1.8kgs [1.21]. A rough comparison of the size of the engine and the size of the alternators gives the following: the engine is 0.9 kg while the alternators are 3.6 kg, which is four times more massive. Comparing volumes, the engine is roughly 0.001 m^3 vs. 0.01 m^3 for the alternators. Considering the twin alternators are significantly larger and more massive than the engine itself, it would be beneficial to design an alternative power transducer that would be much smaller and lighter. Additionally, there have been some efforts to transduce electric power from a thermoacoustic engine, thought these appear mostly in patent searches [1.22, 1.23].

1.3 Piezoelectric Effect

1.3.1 History of Piezoelectric Materials

The piezoelectric effect was first recorded by Jacques and Pierre Curie in 1880 [1.24]. Naturally occurring crystals were discovered to generate an electric potential when a mechanical stressed was applied. Quartz crystals and Rochelle salt were found to have the strongest electrical effect due to this phenomenon. It was named piezoelectric after the Greek word piezien meaning to press or squeeze. Interestingly, the Curie brothers did not realize that there is a converse effect. This was mathematically derived from thermodynamics in 1881 by Gabriel Lippmann [1.24]. The Curie brothers then experimentally confirmed the converse piezoelectric effect and demonstrated the reversibility of these mechanical-electrical coupled effects. Piezoelectricity remained an obscure phenomenon until the end of World War I. In 1917 Paul Langevin was able to use the piezoelectric effect of quartz crystals to generate an underwater ultrasonic pulse that became the first sonar [1.25]. The utility of this application led to an intense amount of research into other uses for the piezoelectric effect including igniters for lighters, phonograph cartridges, piezoelectric buzzers and transducers and ultrasound transducers. During this period, researchers discovered a class of manmade materials that exhibit piezoelectric effects hundreds of times greater than naturally occurring materials and these were classified as ferroelectric materials due to their intrinsic polarization [1.26].

1.3.2 Explanation of Piezoelectric Effect

Piezoelectric materials generate a dipole moment (or an electrical potential) across their crystal structure when subjected to a mechanical force as seen in Figure 1.3.1 [1.26]. Ferroelectric materials are a special class of piezoelectrics which have an intrinsic dipole moment [1.26]. In order to align the domains, these materials need to be poled. In

general they must be subjected to a high DC voltage while heated just below the Curie temperature. The Curie temperature is the temperature above which they lose their ferroelectric properties [1.27]. This procedure aligns the atoms so that the electrical domains are not randomly distributed and is analogous to magnetizing steel.

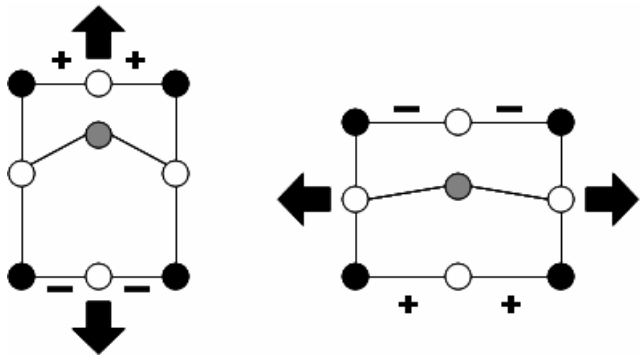

Figure 1.3.1 Piezoelectric effect

Piezoelectric materials are generally categorized as crystals, ceramics or polymers. Crystals include quartz, aluminum orthophosphate, gallium orthophosphate, tourmaline, potassium sodium tartrate (Rochelle salt) and apatite. Ceramics include aluminum nitride, barium titanate, lead zirconate titanate (PZT), bismuth ferrite, lithium niobate, and lithium tantalate. Polymers include polyvinylidene fluoride (PVDF) [1.25]. There are also single crystal materials grown which include lead magnesium niobate/lead titanate (PMN-PT), lead zirconate niobate/lead titanate (PZN-PT) and lithium niobate ($LiNbO_3$) [1.27]. Of these materials, PZT has been extensively studied and is gaining widespread commercial use for its high electromechanical coupling properties [1.27]. PVDF is currently being studied as a lead free alternative to other piezoelectrics. As a

polymer, it is more compliant than piezoelectric ceramics and it has one of the highest electromechanical coupling factors of any polymer [1.28].

PZT is a ceramic with a tetragonal Perovskite structure and has a general composition of $PbZr_xTi_{1-x}O_3$ [1.29]. PZT exhibits strong ferroelectric properties below its Curie temperature because the zirconium or titanium atom is not axially symmetric.

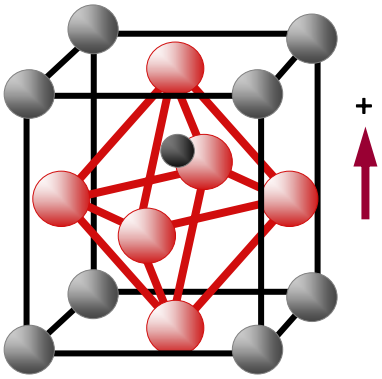

Figure 1.3.2 PZT lattice structure

In Figure 1.3.2 the grey atoms of the outer cube are lead, the red atoms of the inner tetrahedron are oxygen and the center black atom is either zirconium or titanium. Because this structure is not symmetric in all planes, it has an intrinsic dipole, and by physically deforming the lattice, the zirconium or titanium will move within the structure, which increases the dipole in the material, causing an electrical potential difference. A list of its properties can be found at [1.30].

PVDF is different from PZT in that it is a long chain polymer which is transparent and semi-crystalline [1.31]. To polarize the film and align the domains, it is heated, mechanically stretched, and subjected to a DC voltage. This aligns the molecules as seen

in Figure 1.3.3 and this arrangement of PVDF is considered ferroelectric [1.32]. Here carbon is represented by C, fluorine is F and hydrogen is H.

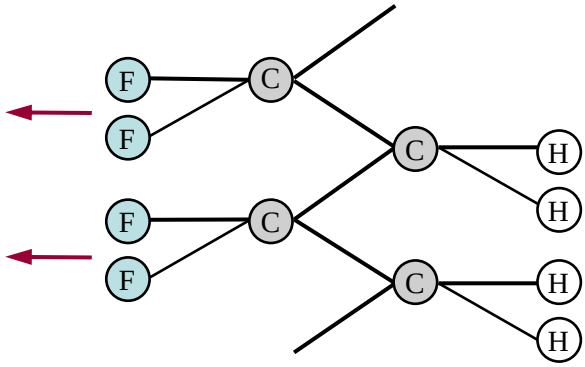

Figure 1.3.3 PVDF lattice structure

The amount of charge or voltage that can be generated from a mechanical force can be quantified for each material. The piezoelectric charge constant *d* is the electrical displacement generated by a mechanical stress or alternately the electrical displacement needed to generate a stress. The piezoelectric voltage constant *g* is the electrical field generated by a mechanical stress or alternately the electrical field needed to generate a stress [1.29]. In general, the charge constant is useful when considering actuator applications and the voltage constant is useful when considering sensor applications.

Because piezoelectric materials are poled, there is an orientation to their polarity and to their charge and voltage constants. This affects how the material responds to mechanical forces in different planes. Figure 1.3.4 illustrates how the axes are labeled for a given sample. Here the gray layer represents the piezoelectric material and the orange is the substrate.

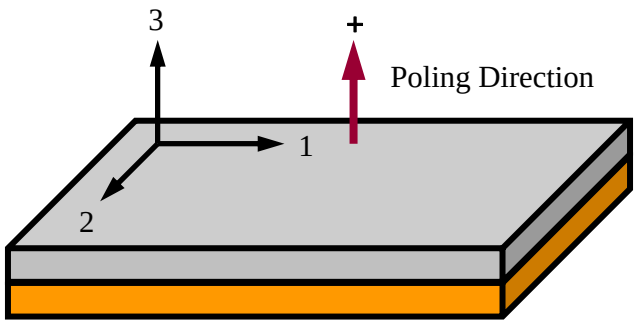

Figure 1.3.4 Axis nomenclature

For example, on a cantilever an applied force in the z (3) direction is translated into a strain along the x (1) axis and because the sample is poled in the 3 direction then the voltage will be taken off in the 3 direction, so the piezoelectric charge constant d_{31} is employed.

1.4 Energy Harvesting

Energy harvesting is capturing ambient energy and transforming it into useful energy usually in the form of electricity. Medium to large scale technologies are well known and are commercially mature. These include wind, solar, hydro and geothermal. For small scale systems however, there is an emerging field of research to generate electricity from the surrounding environment [1.33]. Electrical energy has been harvested from mechanical vibration [1.34], motion [1.35, 1.36, 1.37], heat differences [1.38, 1.39], potential to kinetic energy [1.40, 1.41], and pressure differences [1.42]. To transform these forms of energy into something useful, many different transducers are being developed including electrostatic [1.43], thermoelectric [1.39], electromagnetic [1.44] and piezoelectric [1.45].

Piezoelectric materials are of great interest in small scale energy harvesting because of their compact nature, lack of moving parts and high reliability in converting mechanical energy to electrical energy. Much has been done with piezoelectric elements as transducers to harvest energy from ambient vibrations [1.46] and also kinetic energy [1.47]. Studies have also investigated harvesting ambient acoustic energy using piezoelectric elements coupled to a Helmholtz resonator [1.42].

1.5 Purpose of Study

In the research literature, no publication compares the efficiency and relative merits of different piezoelectric materials as a transducer for a small-scale thermoacoustic engine. This is the primary focus of this research. To achieve this goal important material properties and geometries are considered, representative samples are gathered and characterized, and testing is conducted using an experimental setup to evaluate the samples. Materials are chosen for their stiffness, their coupling coefficient and their quality factor. The materials considered in this study are PZT and PVDF and are described in more detail in Chapter 4. The individual samples are chosen for their geometry and their resonant frequency.

One goal of this study is to match a piezoelectric transducer to an experimental small scale open standing wave thermoacoustic engine with a projected resonance near 1000Hz and a diameter of 14mm which is being concurrently developed [1.49]. Based on the estimated frequency and size of the thermoacoustic engine, piezoelectric samples are investigated with a surface area approximately 78.5mm^2 (0.00785m^2) and whose natural

frequency is on the order of 1000Hz. These samples are also chosen to represent a range of piezoelectric materials and with a range of stiffness and coupling coefficients.

Two operating conditions are considered in this study to simulate the operating conditions of an open standing wave thermoacoustic engine and a closed standing wave thermoacoustic engine. These operating conditions are described in Chapter 2.

Characterization of the electromechanical properties of the chosen samples is performed and an experimental setup is designed to approximate the acoustic output of the thermoacoustic engine. For this, two sound tubes are fabricated with a wide frequency and amplitude range. The samples are mounted to the sound tubes and tests are performed to determine resonant frequency, frequency response, pressure response and power output. These sound tubes and the experimental setups are discussed in Chapter 2.

To verify that the sound tubes results are comparable to expected results from a thermoacoustic engine, two thermoacoustic demonstration engines are fabricated. One is an open standing wave thermoacoustic engine with an acoustic output of 89 Pa RMS at 430 Hz. The other is a closed standing wave thermoacoustic engine operating at 796 Pa RMS at 470 Hz. These two engines are described in detail in Chapter 2. The samples are coupled to these thermoacoustic engines to calculate their power output under these conditions and compared to the sound tube results. The results are presented in Chapter 7 along with an analysis of the data.

1.6 Research Objectives

It is the focus of this study to compare the efficiency and relative merits of different piezoelectric materials as a transducer for a small-scale thermoacoustic engine. The objectives of this work are the following:

- Identify appropriate piezoelectric materials for comparison
- Characterize these different piezoelectric candidates
- Design an experimental setup to simulate thermoacoustic engine conditions
- Measure power output from all samples under varying frequencies and pressures
- Measure power output from two demonstration thermoacoustic engines
- Tabulate results for all samples as a reference to be able to predict power output
- Compare all samples to determine best candidate for given conditions

1.7 References

[1.1] K. T. Feldman. Review of the literature on Sondhauss thermoacoustic phenomena. *Journal of Sound and Vibration*, 7:71—82, 1968

[1.2] C. Sondhauss, Ueber dei Schallschwingungen der Luft in erhitzten Glasrhren und in gedeckten Pfeifen von ungleicher Weite. *Annalen der Physik und Chemie* 79, 1850

[1.3] K. T. Feldman. Review of the literature on Rijke thermoacoustic phenomena. *Journal of Sound and Vibration*, 7:83—89, 1968

[1.4] Lord Rayleigh. The explanation of certain acoustical phenomena, *Nature*, 18:319—321, 1878

[1.5] N. Rott. Damped and thermally driven acoustic oscillations in wide and narrow tubes. Z. Angew. *Math. Phys.*, 20:230—243, 1969

[1.6] N. Rott. Thermally driven acoustic oscillations, part III: Second-order heat flux. Z. Angew. *Math. Phys.*, 26:43—49, 1975

[1.7] N. Rott. Thermoacoustics. *Advanced Applied Mechanics*, 20:135—175, 1980

[1.8] P. Ceperley, A Pistonless Stirling engine – The traveling wave heat engine. *Journal of Acoustical Society of America*, Vol. 77, pp. 1239-1244, 1979

[1.9] R. Radebaugh, A Review of Pulse Tube Refrigeration. *Advanced Cryogenic Engineering*, 35:1191-1205, 1990

[1.10] website http://www.acs.psu.edu/thermoacoustics/refrigeration/benandjerrys.htm

[1.11] S. Backhaus, and G. Swift "A thermoacoustic-Stirling heat engine: Detailed Study," *Journal of Acoustical Society of America*, 107:3148-3166, 2000

[1.12] S. Backhaus, E. Tward, and M. Petach, Thermoacoustic Power Systems for Space Applications, *Space Technology and Applications International*, 2002

[1.13] M. Petach, E. Tward, and S. Backhaus, "Design of a High Efficiency Power Source (HEPS) Based on Thermoacoustic Technology," Final report, NASA contract no. NAS3-01103, 2004

[1.14] O. Symko, E. Abdel-Rahman, Y. Kwon, M. Emmi, and R. Behunin, "Application of thermoacoustic engines to heat transfer in microcircuits." *Thermal Challenges in Next Generation Electronic Systems*, Joshi and Garimella (eds.) 2002.

[1.15] R. Chen, C. Chen, and J. DeNatale, Study of a Miniature Thermoacoustic Refrigerator, IMECE 2002-33342, 2002

[1.16] A. Castrejon-Pita and G. Huelsz, Heat to electricity thermoacoustic magneto-hydrodynamic conversion, *Applied Physics Letters*, 2007 downloaded 1/28/2008

[1.17] S. Backhaus, E. Tward, and M. Petach, "Traveling-wave thermoacoustic electric generator," *Applied Physics Letters*, 2004

[1.18] P. Schewe, and P. Stein, "Acoustically Powered Deep-Space Electric Generator," www.aip.org/pnu/2004/split/695-2.html

[1.19] T. Hanson, "A traveling-wave engine to power deep space travel," www.lanl.gov/worldview/news/releases/archive/04-078.shtml

[1.20] M. Telesz, Design and Testing of a Thermoacoustic Power Converter, MS thesis Georgia Institute of Technology, 2006

[1.21] Data taken from website: www.qdrive.com/index.php?id=63

[1.22] O. Symko, M. Emmi, R. Behunin, and Y. Kwon, "High Frequency Thermoacoustic Energy Converter," International patent 12 June 2003

[1.23] R. Keolian, and K. Bastyr, Thermoacoustic Piezoelectric Generator, United States Patent Office, July 25, 2006

[1.24] W. Mason, Piezoelectricity, its history and applications, *Journal of Acoustic Society of America*, 70:1561-1566, 1981

[1.25] W. Mason, Applications of acoustical phenomena, *Journal of Acoustic Society of America*, 68:53-63, 1980

[1.26] J. Philips, Piezoelectric Technology Primer, CTS Wireless Components, downloaded May 16, 2007

[1.27] Piezoelectric Ceramics: Principles and Applications, APC International, Ltd. Downloaded May 17, 2007

[1.28] Piezo Film Sensors Technical Manual, Measurement Specialties downloaded April 15, 2007

[1.29] S.O. Kasap, *Principles of Electonic Materials and Devices, Third Edition.* McGraw Hill, 2006

[1.30] Downloaded from website http://www.efunda.com/materials/piezo/material_data/matdata_output.cfm?Material_ID=PZT-5A on April 11, 2008

[1.31] Downloaded from website http://en.wikipedia.org/wiki/Polyvinylidene_fluoride April 11, 2008

[1.32] G.M. Garner and K.J. Humphrey, Ch 5 Ferroelectric Polymers, J.A. Chilton and M.T. Goosey (eds.) *Special Polymers for Electronics and Optoelectronics*, Chapman and Hall, 1995

[1.33] H. Sodano, J. Lloyd, and D. Inman, An experimental comparison between several active composite actuators for power generation. *Smart Materials and Structures*, 15:1211-1216, 2006

[1.34] S. Anton, and H. Sodano, A Review of power harvesting using piezoelectric materials 2003-2006, *Smart Materials and Structures*, 16:R1-21, 2007

[1.35] J. Kymisis, C. Kendall, J. Paradiso, and N. Gershenfeld, "Parasitic power harvesting in shoes," 2nd IEEE International Conference on Wearable Computing, pp. 132 – 137, 1998

[1.36] E. Hausler, and E. Stein, "Implantable physiological power supply with PVDF film," *Ferroelectronics*, 60:277-282, 1984

[1.37] J. J. Allen and A. J. Smits, "Energy harvesting eel," *Journal of Fluids and Structures*, 15:1 – 12, 2001

[1.38] S. Whalen, M. Thompson, D. Bahr, C. Richards and R. Richards, Design, fabrication and testing of the P^3 micro heat engine, *Sensors and Actuators, A: Physical*, 104:290-298, 2003

[1.39] Downloaded from http://www.micropelt.com/applications/power_bolt.php

[1.40] R. Guigon, J. Chaillout, T. Jager, and G. Despesse, Harvesting raindrop energy: theory. *Smart Materials and Structures*, Vol. 17, 2008

[1.41] R. Guigon, J. Chaillout, T. Jager, and G. Despesse, Harvesting raindrop energy: experimental study. *Smart Materials and Structures*, Vol. 17, 2008

[1.42] S. Horowitz, A. Kasyap, F. Liu, D. Johnson, T. Nishida, K. Ngo, M. Sheplak, and L. Cattafesta, Technology development for self-powered sensors, AIAA-2002-2702, 1st Flow Control Conference, June 2002

[1.43] P. Mitcheson, P. Miao, B. Stark, E. Yeatman, A. Holmes and T. Green, MEMS electrostatic micro-power generator for low frequency operation, *Sensors Actuators* A 115:523–529, 2004

[1.44] P. Glynne-Jones, M. Tudor, S Beeby and N White, An electromagnetic, vibration-powered generator for intelligent sensor systems *Sensors Actuators* A 110:344–339, 2004

[1.45] C. Richards, M. Anderson, D. Bahr, and R. Richards, Efficiency of energy conversion for devices containing a piezoelectric component, *Journal of Micromechanics and Microengineering*, 14:717-721, 2004

[1.46] S. Roundy, P. Wright, J. Rabaey, A study of low level vibrations as a power source for wireless sensor nodes, *Computer communications*, 26:1131-1144, 2003

[1.47] S. Meninger, J. Mur-Miranda, R. Amirtharajah, A. Chandrakasan, and A. Lang, Vibration to Electric Energy Conversion *IEEE Transactions on VLSI Systems* Vol. 9 pp. 64-76 (2001)

[1.48] M. Ericka, D. Vasic, F. Costa and G. Poulain, "Predictive energy harvesting from mechanical vibration using circular piezoelectric membrane," IEEE Ultrasonics Symposium, pp. 946-949, 2005

[1.49] N. Shafiei-Tehrany, Development of small-scale thermoacoustic engine and thermoacoustic cooling demonstrator, Masters Thesis WSU, 2008

CHAPTER 2

CHARACTERIZATION EQUIPMENT

In this chapter, the experimental setups are briefly described and all equipment needed for those experiments are presented. Each piece of equipment is introduced with a description and a short explanation of its use. A summary of its specifications are also given. Chapter 3 gives a more detailed explanation of the experimental setup and the operating procedures for each apparatus.

2.1 Operating Conditions

To simulate the operating conditions for both an open ended and a closed ended standing wave thermoacoustic engine, fixtures are fabricated for both methods of operations. The fixtures are designed to work with both the sound tube and the thermoacoustic engine to ensure that the operating conditions are constant for all tests.

For the open condition, the samples are clamped on one edge using an aluminum clamp. This creates a cantilevered arrangement of the sample as seen in Figure 2.1.1.

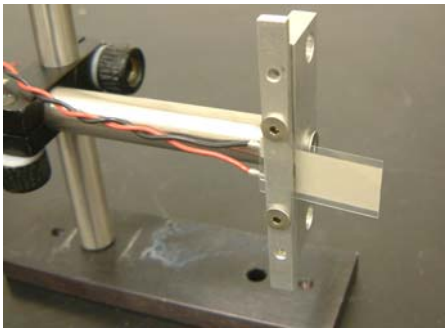

Figure 2.1.1 Open condition cantilever clamping

This same fixture is used to clamp all samples for both the open sound tube and the open thermoacoustic engine experiments. The sound tube and the thermoacoustic engines are described in more detail in Section 2.

For the closed condition, the samples are fastened along their entire perimeter to the acrylic end wall which serves as the termination for both the sound tube and the thermoacoustic engine. Tape is used to fasten the samples to ensure a complete seal. This creates a fully constrained membrane as seen in Figure 2.1.2.

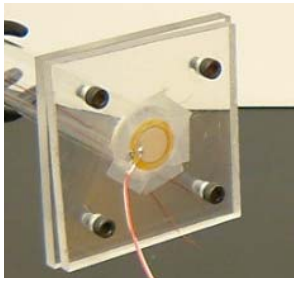

Figure 2.1.2 Closed condition fully constrained clamping

This same method is used for both the closed sound tube and the closed thermoacoustic engine. These devices are described in more detail in Section 2.

2.2 Experimental Setup

2.2.1 Characterization

To assess the performance of each of the piezoelectric samples chosen, they are first characterized by their electromechanical properties. Because these materials are electrical and mechanical in nature, it is necessary to establish equivalent parameters.

The equivalent circuit parameters are discussed in detail in Chapter 3. To determine the electrical parameters of each sample, an electrical impedance test is performed using an impedance analyzer. This test returns the phase and electrical impedance over a frequency range and is described in detail in Chapter 3. An independent measurement of mechanical stiffness is also performed on each sample using a bulge test and a mechanical deflection test. These are both described in Chapter 3. This data is then used to determine all electrical and mechanical parameters for each sample.

2.2.2 Sound Tube

Once the electromechanical properties of the sample have been established, the power output is determined experimentally using a sound tube as seen in Figure 2.2.1. The resonant frequency of each sample is already known from the impedance analyzer, so the sound tube is used to provide an acoustic signal to drive the sample over a range of frequencies above, below and at resonance. This gives a frequency response curve for the sample. The sound tube is also used to drive the sample over a range of acoustic pressures to determine how the pressure amplitude affects the power output of the sample. The procedure for testing the samples on the sound tube and calculating power output is described in detail in Chapter 3.

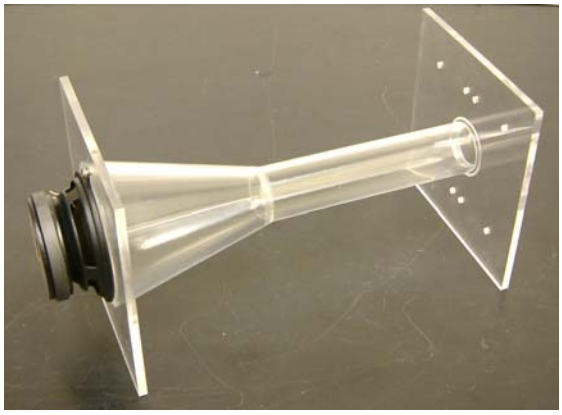

Figure 2.2.1 High frequency sound tube

Two sound tubes are designed and fabricated, one for high frequencies and one for low frequencies. To sustain an acoustic plane wave within the tube, the wavelength must be much greater than the inner diameter of the tube: $\lambda > 1.71d$ where d is diameter and $\lambda=c/\omega$ [2.1]. The cutoff frequency is then calculated for each tube:

$$2\pi f < \frac{1.842c}{a} \tag{2.1}$$

Here c = 343m/s and a = radius in m.

For frequencies below 2000 Hz (the cutoff frequency), a large sound tube is fabricated with radius a = 0.0625m. For higher frequencies, the small tube has radius a = 0.015m giving it a cutoff frequency of 7000 Hz. Each of these sound tubes consist of an acrylic tube with a speaker mounted at one end and a rigid wall at the other end with openings to accept a pressure transducer and a piezoelectric membrane. The samples are mounted on the 10mm diameter opening for the closed conditions and for the open conditions the end wall is removed and the samples are clamped with the aluminum fixture as described above. The dimensions of both sound tubes are given in Figure 2.2.2.

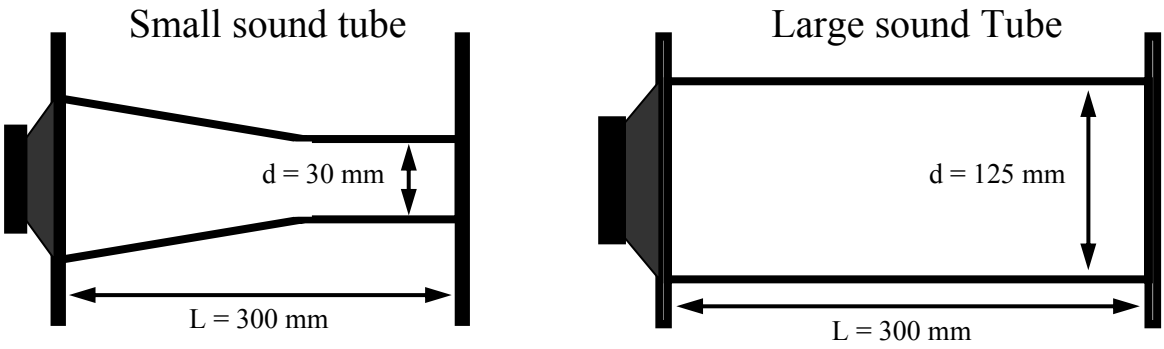

Figure 2.2.2 Geometry of large and small sound tubes

2.2.3 Thermoacoustic Engine

Once the samples have been tested on the sound tube, they are tested on two thermoacoustic engines. The samples are coupled to each thermoacoustic engine using the same method as used with the sound tubes, and the power output for each sample is obtained. The procedure for testing the samples on the thermoacoustic engine and calculating power output is described in detail in Chapter 3.

An open standing wave demonstration thermoacoustic engine is fabricated to specifications from the Penn State acoustics program [2.2]. A number of similar engines are constructed and tested to obtain a range of output amplitudes and frequencies. These simple standing wave thermoacoustic engines are closed on one end and open on the other end (closed-open) and are heat driven engines or prime-movers. They consist of a glass tube with one open end, a stack made of a porous ceramic material and a nichrome (NiCr) wire heating element. The heating element is on the end of the stack that is facing the closed end of the glass tube and the stack is placed approximately 1/3 the length of the tube near the closed end. Figure 2.2.3 shows the large open thermoacoustic engine and the stack.

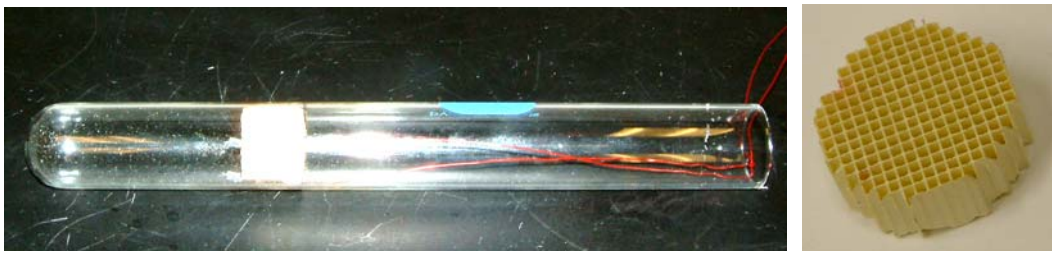

Figure 2.2.3 Large open thermoacoustic engine and stack

A closed-closed standing wave demonstration thermoacoustic engine is also fabricated. The engine consists of the same components as the open engines, but an acrylic fixture is fabricated and clamped over the open end of the engine. This changes the resonant frequency of the engine by a factor of two (the length is now equal to $\lambda/2$) and the stack position is now approximately 1/6 of the tube length. Figure 2.2.4 shows the long closed thermoacoustic engine.

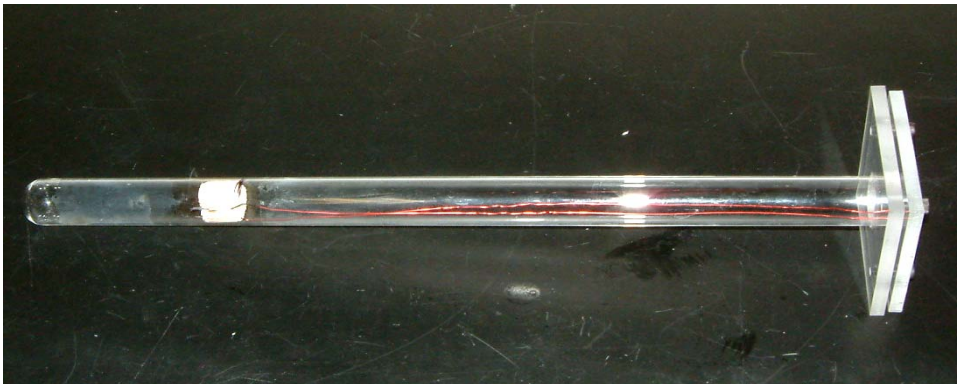

Figure 2.2.4 Long closed thermoacoustic engine

The geometry and resonant frequency is unique for each engine and all are listed in Table 2.2.1. The pressure is reported in Pa RMS and the sound pressure SPL is in dB re 20 μPa. All engines are closed-open standing wave thermoacoustic engines except for

the long closed which is a closed-closed standing wave engine. The thermoacoustic engines chosen for this study are the large open engine seen in Figure 2.2.3 and the long closed engine seen in Figure 2.2.4. Also listed are the two experimental engines which were tested. These are designated by open short and open long and are the final two entries in Table 2.2.1.

TA Engine	ID mm	Length mm	Frequency Hz	Pressure Pa	SPL dB
Small	12.5	125	694.4	72	131.1
Medium	18	147	581	90	133.1
Large	22.5	200	416.7	89	133.0
Long	22.5	375	227.3	98	133.8
Long closed	22.5	375	470	796	152.0
Open Short	14	58	1250	62	129.8
Open Long	14	93	830	60	129.6

Table 2.2.1 Thermoacoustic engines

To determine the operating pressure amplitude and frequency, a pressure transducer is used which is connected to an oscilloscope. The pressure transducer is placed in front of the opening at 0^o incidence and placed at 10mm distance from the opening. The frequency is read off of the oscilloscope and the pressure amplitude is calculated from the microphone sensitivity given.

It is recognized that taking the measurement in this manner affects the sound field generated by the thermoacoustic engine, but it is assumed that during operation and testing a piezoelectric sample will be placed in front of the opening and so the conditions of measurement and experiment are considered similar. This does not account for the

difference in acoustic impedance between the microphone used to measure the pressure amplitude and the piezoelectric sample used to generate electric power.

2.3 Impedance Analyzer

To find the electrical impedance, all samples are tested on an Agilent 4294A Precision Impedance Analyzer as shown in Figure 2.3.1.

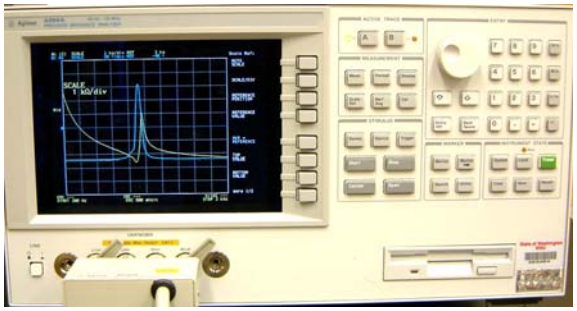

Figure 2.3.1 Agilent 4294A Precision Impedance Analyzer

This device excites the mechanical-electrical piezoelectric device with an input signal and reads the resultant signal to analyze the device's electrical impedance. It has a frequency range of 40Hz – 110GHz and a source voltage of OSC 1mV – 1V [2.3]. Data traces are recorded of complex impedance Z-Y and also of impedance magnitude and phase |Z|-θ. The impedance analyzer saves the data traces as text files, which can then be imported into Matlab or other programs to evaluate.

2.4 Function Generator

To drive the sound tube, two different function generators are used: a Tektronix AFG 310 arbitrary function generator and a B+K Precision 4011A 5MHz function generator as shown in Fig. 2.4.1.

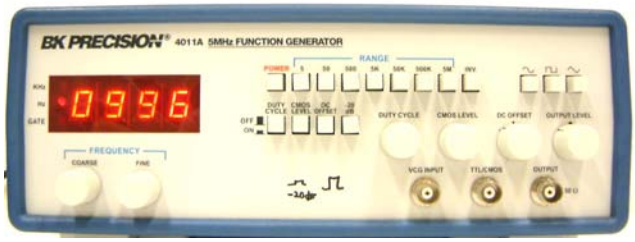

Figure 2.4.1 Function Generator

Each of these devices allows for a wide frequency range, a variable output voltage (amplitude), variable duty cycle and the choice of square, pyramidal and sinusoidal waveforms. For all of the samples and tests, the duty cycle is chosen to be 50% and a sinusoidal wave is chosen. This produces a pure sinusoidal wave tone which produces a single frequency sound wave. To generate large enough amplitude, the output signal from these function generators often needs to be amplified, and so the signal was sent to a signal amplifier.

2.5 Signal Amplifier

To amplify the signal produced by the function generator, two different pieces of equipment are used: a Harman/Kardon model hk330Vi stereophonic amplifier as seen in Figure 2.5.1 and a Stanford Research Systems Model SR560 low noise preamplifier.

Figure 2.5.1 Harmon/Kardon model hk330Vi amplifier

The Harmon Kardon amplifier has a continuous output of 25 Watts [2.4] but introduces some noise into the signal. The Stanford preamplifier in contrast does not have as much amplification, but the output signal is very clean. The Stanford preamplifier also has a number of settings for a high-pass and low-pass filter.

2.6 Pressure Transducer

To determine the pressure amplitude and the frequency of the sound waves produced a pressure transducer is used which is essentially a sensitive microphone. The pressure transducer used for all tests is a Bruel & Kjaer pressure-field ½" microphone type 4134. The sensitivity of this microphone is calibrated to be 11.1 mV/Pa [2.5]. The microphone is shown in Figure 2.6.1 attached to a preamplifier and a power supply.

Figure 2.6.1 B&K pressure transducer

2.7 Laser Vibrometer

For measuring displacement and velocity of the samples a laser vibrometer is used which operates on the principle of Doppler shift. The laser vibrometer consists of a Polytec OFV-511 sensor head and a Polytec OFV-5000 controller. The sensor head emits a Helium-Neon laser beam which is reflected off the sample and back into the sensor head. By using wave interference and fringe counting, the controller compares the phase shift and frequency of the reflected laser wave to the emitted wave. This information is used to measure the displacement and velocity of the sample. The displacement is calculated from the phase shift and the velocity is calculated from the frequency shift. This equipment is very sensitive and has a user-defined resolution of 4µm- 1280µm or 4µm/s - 1280µm/s [2.6]. Figure 2.7.1 shows a schematic of the laser vibrometer and its components.

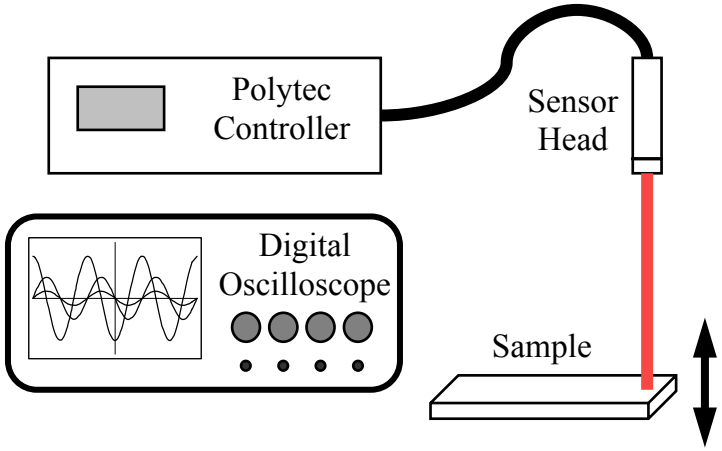

Figure 2.7.1 Schematic of Laser Vibrometer

2.8 Oscilloscope

For signal processing and data acquisition, a digital oscilloscope is used as seen in Figure 2.8.1. All data is captured using a Tektronix TDS 420A and a GW Instek GDS-2204 digital real-time oscilloscope and this data is recorded to computer in a comma separated value (CSV) file. Both oscilloscopes have 4 input channels, a bandwidth of 100MHz and a maximum sample rate of 1GS/s [2.7, 2.8]. The data signal is captured to computer via a GPBIP cable and imported using WaveStar software for the Tektronix and for the Instek the data is sent via a USB cable and imported as a CSV file.

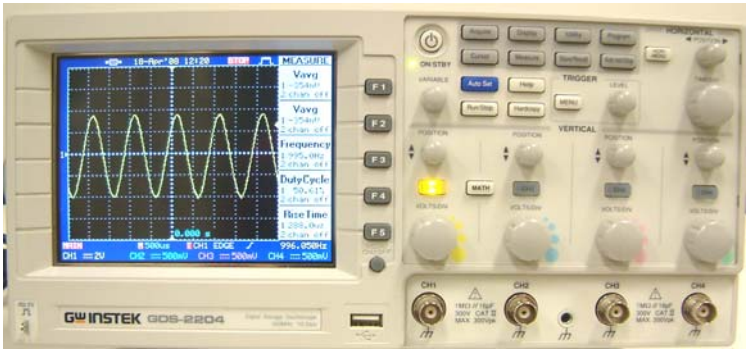

Figure 2.8.1 GW Instek GDS-2204 Digital Oscilloscope

2.9 Multimeter

For electrical power measurements, RMS voltage needs to be recorded. To simplify the measurement and calculation of power, a Fluke 189 True RMS digital multimeter is used as seen in Figure 2.9.1.

Figure 2.9.1 Fluke 189 true RMS multimeter

The multimeter measures AC voltage from 2.4mV to 1000V with a 100 kHz bandwidth and a maximum resolution of 0.001mV [2.9]. Readings are recorded directly into a spreadsheet to calculate power output.

2.10 Power Supply

To heat the nichrome wire used drive the thermoacoustic engines, a power supply was needed. The power supply used was a Xantrex XHR 150-7 DC power supply as seen in figure 2.10.1. The specifications of the output range are 0-150 Volts and 0-7 Amperes.

Figure 2.10.1 Xantrex XHR 150-7 DC Power Supply

2.11 Vacuum Chamber

To obtain impedance data for the samples in a vacuum, a vacuum chamber is used as seen in Figure 2.11.1. This chamber is large enough to accommodate all samples in the same fixture used for the experiments. The sample is placed inside the chamber and the chamber is attached to a Welch W Series Model 3 high vacuum pump which has an ultimate pressure $3x10^{-4}$ torr. The chamber is allowed to pump down for a minimum of 15 minutes to evacuate the chamber of air.

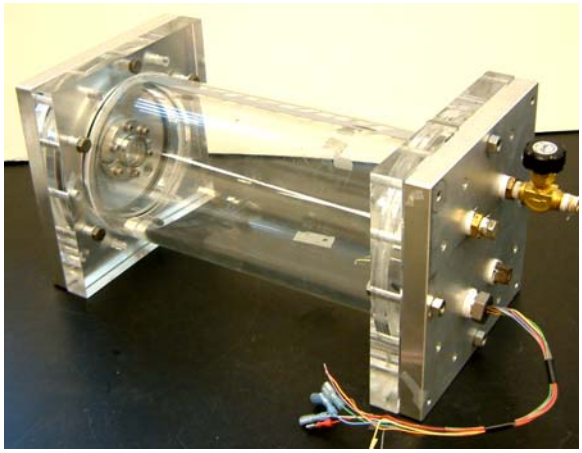

Figure 2.11.1 Vacuum chamber

2.12 References:

[2.1] L. Kinsler, A. Frey, A. Coppens and J. Sanders, Fundamentals of Acoustics Fourth Edition, 2000

[2.2] From http://www.acs.psu.edu/thermoacoustics/refrigeration/laserdemo.htm

[2.3] Agilent 4294A Precision Impedance Analyzer Operation Manual, Agilent Technologies, 2003

[2.4] Harmon Kardon hk330Vi Manual

[2.5] Data sheet downloaded from website http://www.bksv.com/3034.asp

[2.6] Vibrometer Controller OFV-5000, Polytec Manual

[2.7] Tektronix TDS 420A Manual

[2.8] GW Instek GDS 2204 Users Manual

[2.9] Fluke Model 179 & 189 Users Manual, 2002

CHAPTER 3

METHODS TO OBTAIN PARAMETERS AND DATA

In this chapter, all experimental procedures are described. First the characterization equipment and tests are explained, along with a representative example of the procedure followed for each sample. Next the sound tube experimental setup is described in detail including the procedures followed to obtain power output for each sample. The thermoacoustic engine experimental setup is described as well. Error in the experimental setup and measurements is discussed and the calculation is given.

3.1 Equivalent Circuit Model

Piezoelectric materials are electromechanical in nature and so they exhibit both electrical and mechanical properties. Because of this it is useful to develop an equivalent circuit model which equates electrical parameters with mechanical ones. Table 3.1.1 lists the equivalent parameters for the electrical and mechanical domains [3.1].

Electrical Domain	**Mechanical Domain**
Voltage (V) – V	Force – N
Current (i) – A	Velocity – m/s
Charge (Q) – C	Displacement – m
Capacitance (C_o) – F	Compliance (C_m) – m/N
Inductance (L) – H	Mass – kg
Impedance (Z_e) – Ω	Impedance – Z_m

Table 3.1.1 Electrical and mechanical equivalence

Once the equivalent parameters have been established, a circuit model can be constructed for the piezoelectric device. Figure 3.1.1 shows a generic RCL circuit for PZT. This generalized model can be applied to any piezoelectric sample.

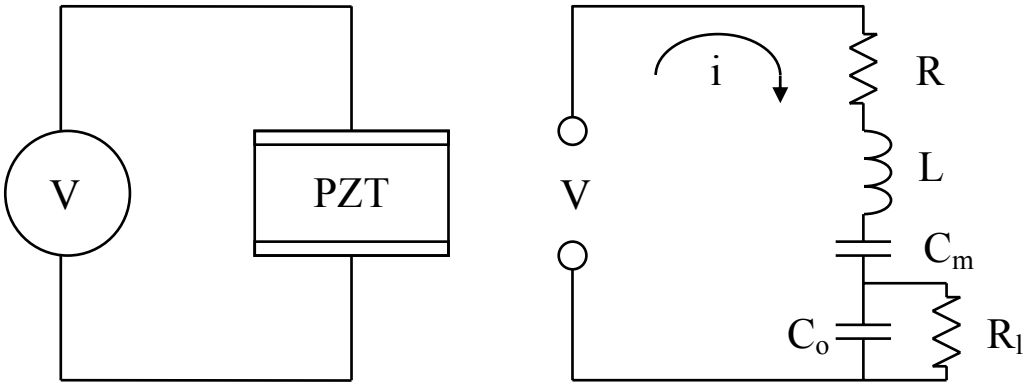

Figure 3.1.1 PZT RCL equivalent circuit

Here C_o is the shunt capacitance or the electrical capacitance of the sample, R_l is the load resistance, R is the resistance which is analogous to mechanical damping, L is the inductance which is analogous to mass, and C_m is mechanical capacitance which is analogous to the inverse of stiffness. Once these parameters have been measured, a number of other properties of the sample can be calculated [3.2]. Because piezoelectric devices are coupling electrical and mechanical domains, one important property is called the electromechanical coupling coefficient, k^2 which is defined as the following:

$$k^2 = \frac{\textit{Mechanical energy converted to electrical energy}}{\textit{Input of mechanical energy}} = \frac{C_m}{C_o + C_m} \tag{3.1}$$

Resonant frequency, f_n, is given as the following:

$$f_n = \frac{1}{2\pi\sqrt{LC_m}} \tag{3.2}$$

And the mechanical quality factor Q is the following:

$$Q = \frac{1}{2\pi f_n RC} \tag{3.3}$$

3.2 Electrical Impedance

The following procedure refers specifically to the 11x30mm PZT bender, but it is the same general procedure used to test all samples. To begin, the Agilent 4294A Precision Impedance Analyzer is fully warmed up (for 30 minutes) and calibrated prior to testing. The sample is clamped to the experimental fixture, secured in place and the impedance analyzer probes are attached to the sample as seen in Figure 3.2.1.

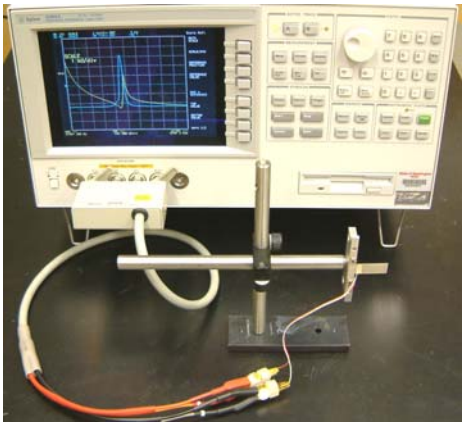

Figure 3.2.1 Impedance Analyzer

Care must be taken to isolate the sample from ambient vibrations to obtain the most accurate results. To implement this, the sample should be isolated from test equipment and other sources of vibrations. For the boundary conditions to remain the

same during testing, ideally the sample will be tested in situ. This means that the experiment to be run should be set up and then the impedance test is performed immediately before or after the other test is run. To perform the impedance test, the source or input voltage is set high enough to excite the sample for a good response while low enough to avoid non-linear effects. In the case of the PZT bender sample, the OSC voltage is set at 500mV. The sweep frequency is chosen first over a large range (40Hz-10000Hz) to identify the resonant frequency modes. It is important to determine the fundamental frequency mode for analysis. For the PZT bender that is tested, the fundamental resonant frequency is found to be just above 200 Hz so the sweep range is adjusted to zoom in on this region (189Hz-250Hz). Once the domain and range have been determined, the number of data points acquired is changed to the maximum (800 points) and one final frequency sweep is completed as seen in Figure 3.2.2 (a) for complex impedance (Z - Y) and Figure 3.2.2 (b) for impedance magnitude and phase (|Z|- θ).

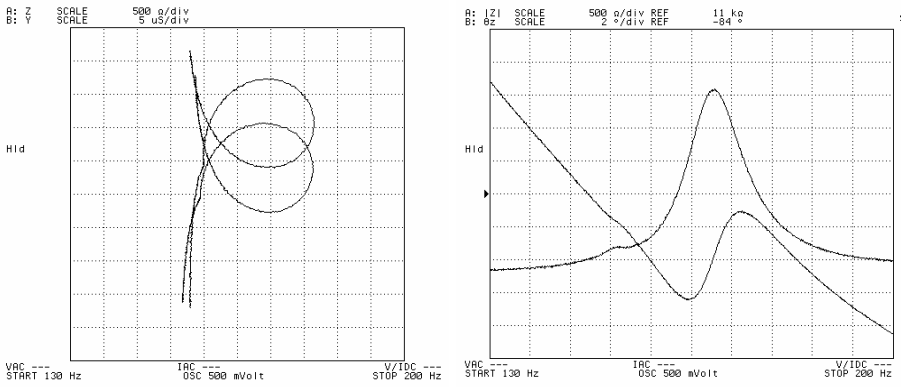

Figure 3.2.2 (a) Complex impedance data from the impedance analyzer

(b) Magnitude impedance and phase data from the impedance analyzer

Both of these data sets are then saved to ASCII files. The complex impedance file is saved for the verification step. The magnitude phase data ASCII file is then used as the input for a MATLAB code that creates a curve of best fit to determine the electrical impedance parameters as seen in Figure 3.2.3.

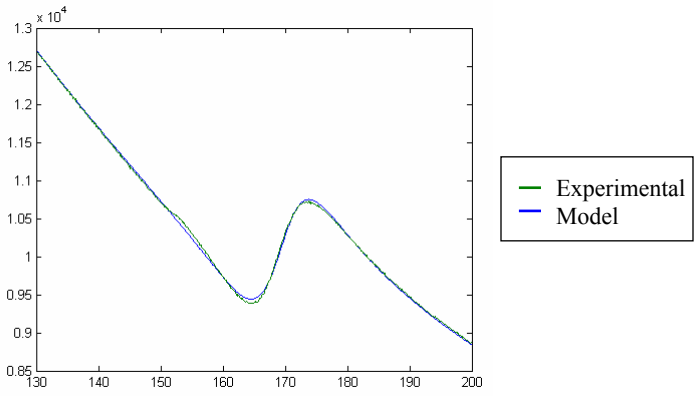

Figure 3.2.3 MATLAB curve fit output

The code requires user input for an approximation of the resonant frequency and then utilizes the method of least squares to fit the data [3.3].

From this analysis the parameters C_o, R, L, C_m, k^2, f_n, and Q are obtained. The output parameters for this sample are then imported to an Excel spreadsheet to calculate the other parameters as described below. This procedure is performed in air and also in vacuum by placing the sample under the same clamping conditions in the vacuum chamber described in Chapter 2.

3.3 Stiffness Measurement

A measurement of stiffness is obtained by the following methods: for the closed condition (fully clamped) a bulge test is used and for the open condition (simply clamped) a mechanical load test is performed. These results are verified with an electromechanical ring-out test.

The bulge test is a static measurement of the deflection of the membrane at a given pressure. The experimental setup is shown in Figure 3.3.1.

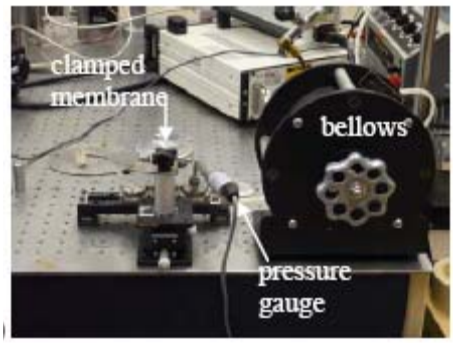

Figure 3.3.1 Bulge test for closed stiffness [3.4]

This data is obtained by clamping the sample down on an aluminum puck which is attached to a pneumatic line, applying pressure with the bellows and measuring the deflection of the sample with the laser vibrometer [3.4]. The data from these tests is captured with LabView and analyzed using Excel as seen in Figure 3.3.2.

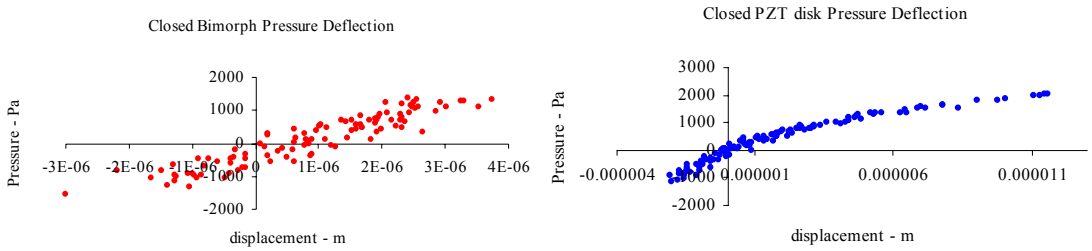

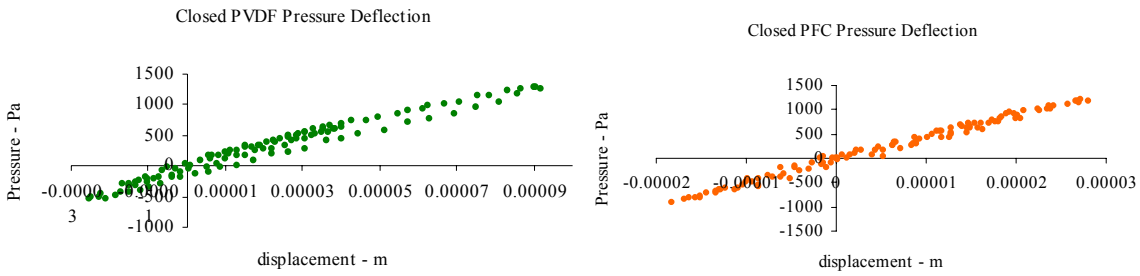

Figure 3.3.2 Closed condition pressure displacement graphs

Stiffness has units N/m and is calculated as the slope of the line of the pressure-deflection curve normalized by the area of the membrane. Restated this means stiffness $\bar{s}$ equals pressure *P* divided by displacement *d* multiplied by area A.

$$\bar{s} = \frac{P}{d} A \tag{3.4}$$

For the open condition, the sample is considered a simply clamped cantilever and so a straightforward force deflection test is performed as seen in Figure 3.3.3.

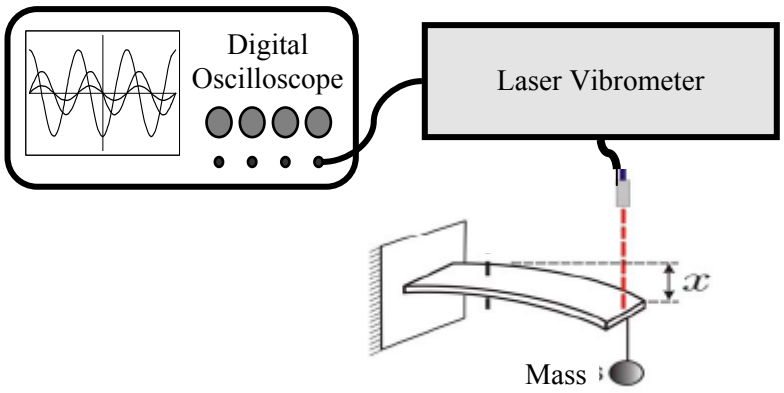

Figure 3.3.3 Schematic of stiffness measurement

The sample is clamped at one end and a known force is applied to the free end on the center line of the transducer and the deflection is measured at that point. Four objects of different masses are measured and the force they exert is calculated as F=m*g where g is gravity 9.81 m/s^2.

Object	Mass	Force
Mass 1	0.44 g	0.0043 N
Mass 2	0.79 g	0.0077 N
Mass 3	1.25 g	0.0122 N
Mass 4	1.61 g	0.0158 N

Table 3.3.1 Known masses for stiffness test

These masses are then suspended from the end of the cantilever and deflection is measured using the laser vibrometer. The results are then graphed as shown in Figure 3.3.4. The slope of the line gives the relationship Force/deflection, which is stiffness of the sample in N/m.

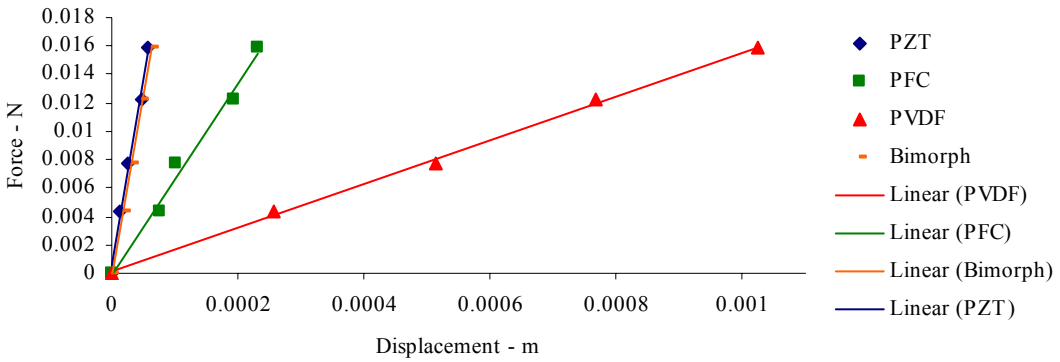

Figure 3.3.4 Force displacement measurements for all samples

This measurement was validated using another method of obtaining stiffness by performing a ring-out test. The ring-out test is a measurement of the mechanical deflection of the sample for a given electrical impulse. In this experimental setup a function generator sends a pulse of known voltage and duration to the sample which rings-out or vibrates at its fundamental resonant frequency and the deflection is measured with the laser vibrometer. With the electrical parameters obtained from the impedance analyzer and the data taken from the ring-out test, the electro-mechanical coupling ψ and stiffness $\bar{s}$ can be calculated from the following formulas [3.5]:

$$\psi = \frac{V_0 T}{2\pi L f_n x^*}\left[1 - \frac{\pi\xi}{2}\right] \qquad \text{where} \quad \xi = \frac{R}{2\sqrt{LC}} \quad \text{and} \quad \bar{s} = \frac{\psi^2}{C_m} \tag{3.5}$$

Here T is the time of input pulse in seconds of and x^* is the distance of deflection from baseline in meters.

3.4 Mass and Other Calculated Parameters

From the parameters obtained above, we can now calculate effective mass m, damping coefficient b, and electro mechanical coupling ψ^2. The units for these parameters are: m in kg, b in kg/s, and ψ^2 is nondimensional. The equations used are as follows [3.2]:

$$f = \frac{\sqrt{\bar{s}/\mathrm{m}}}{2\pi} \qquad \text{or} \qquad m = \frac{\bar{s}}{(2\pi f)^2} \tag{3.6}$$

$$b = \frac{\sqrt{\bar{s}m}}{Q} \tag{3.7}$$

$$\psi^2 = C_m \bar{s} \tag{3.8}$$

3.5 Sound Tube and Thermoacoustic Engine

Once all of the samples have been characterized with the previous tests, data is taken on their frequency response, pressure response and peak power output. These tests are performed on the variable sound tubes as described in Chapter 2. Using the sound tube, the pressure and frequency of the driving signal can be independently controlled by means of a function generator and a signal amplifier, and a load and a multimeter is attached to the sample to measure electrical power as seen schematically in Figure 3.5.1.

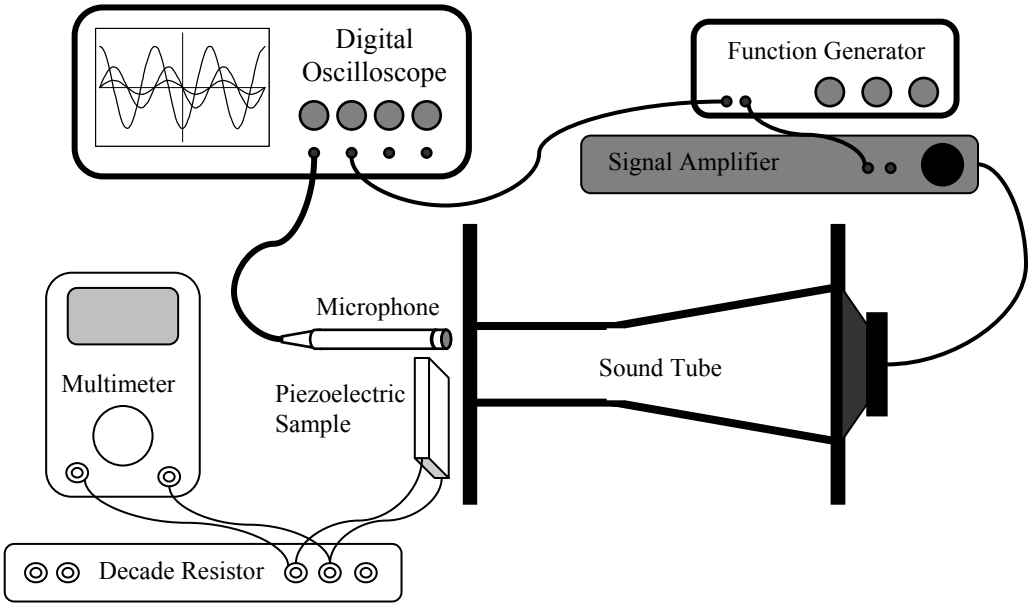

Figure 3.5.1 Schematic of Sound tube experiment

The experimental setup for open conditions is shown in Figure 3.5.2 (a) and for closed conditions is shown in Figure 3.5.2 (b).

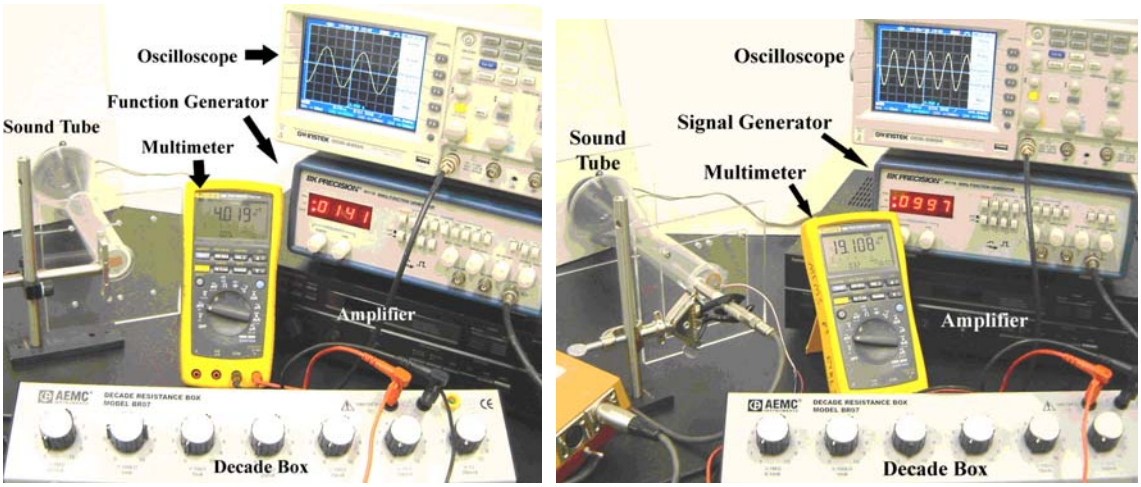

Figure 3.5.2 (a) Open (b) Closed sound tube experiment

The sound tube signal is generated by the function generator which controls frequency and the pressure amplitude is controlled by the signal amplifier. Measurements of acoustic pressure are made at the other end of the sound tube with the pressure transducer or microphone attached to the oscilloscope. The sample is mounted adjacent and parallel with the microphone at the end of the sound tube. It is important that both the sample and the microphone are in the same plane and this plane is parallel to the incident acoustic plane waves. In the open condition, the samples are held 5mm away from the open end of the sound tube and are clamped on one side by means of a straight clamping fixture as shown in Figure 3.5.3.

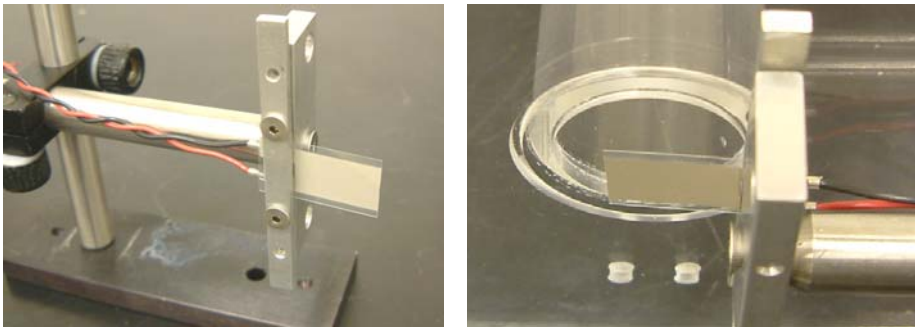

Figure 3.5.3 Open condition fixture

In the closed condition, the samples are fully constrained onto a 10mm diameter opening by means of a clamped fixture as shown in Figure 3.5.4.

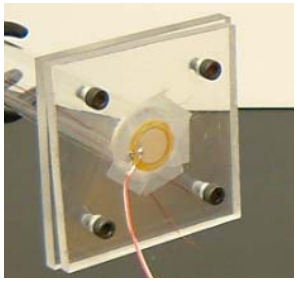

Figure 3.5.4 Closed condition fixture

For the open thermoacoustic engine, the fixture used to clamp the samples for the sound tube is again used to hold the samples 5mm away from the open end of the thermoacoustic engine. The engine used in these tests is the large open thermoacoustic engine described in Chapter 2. This setup produces acoustic power at a frequency of 430 Hz and a pressure amplitude of 89 Pa or an SPL of 113 dB re 20μPa. For the closed thermoacoustic engine, an acrylic carrier is used which has a 10mm opening and the samples are mounted identically to the closed sound tube conditions. The engine used in these tests is the long closed thermoacoustic engine described in Chapter 2. This setup produces acoustic power at a frequency of 470 Hz and a pressure amplitude of 796 Pa or SPL of 132 dB re 20μPa.

3.6 Power Measurements

Power is measured in all tests by attaching the sample to a variable load resistor (decade box) and measuring the voltage across the sample as seen in Figure 3.6.1.

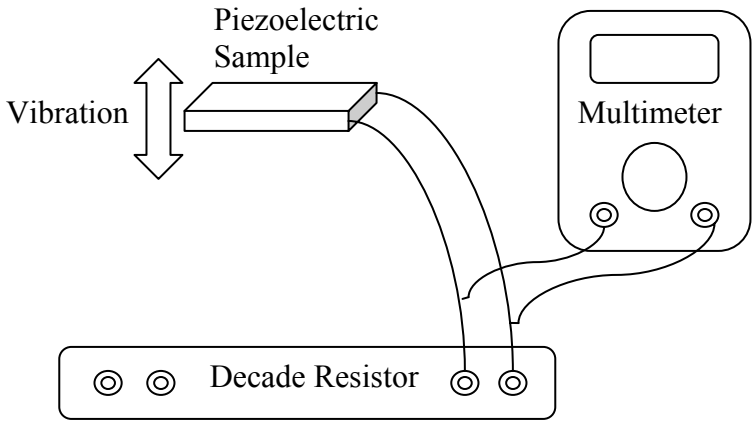

Figure 3.6.1 Schematic of power measurement

The sample to be tested is fixed in the experimental setup and the electric leads are attached to the decade box. The Fluke 189 True RMS multimeter is then attached in parallel to measure the voltage generated by the sample with the given load.

The sound tube or thermoacoustic engine is turned on to give a driving signal to the sample and the change in AC RMS voltage output from ambient is measured. The following formula is used to calculate the power produced [3.6]:

$$\Pi_{electric} = \frac{V_{rms}^2}{R_L} \tag{3.9}$$

Here Π is electric power in Watts, V_{rms} is voltage in Volts and R is resistance in Ohms. With the known resistance and the measured RMS voltage, power is calculated. A complete description of the electric power calculation is given in Appendix B.

The error of this measurement is also calculated. The decade box has an accuracy of 1% and the multimeter has an accuracy of 0.4%. Because of the fluctuations in the voltage readings from the sample, the measurements were generally truncated and rounded to the nearest 1mV. Based on these numbers and using a weighted average

formula, error is calculated for each sample and is reported in Chapter 6 for all results. The full calculation is reported in Appendix A.

3.7 References:

[3.1] J. Philips, Piezoelectric Technology Primer, CTS Wireless Components, downloaded May 16, 2007

[3.2] S.O. Kasap, Principles of Electonic Materials and Devices, Third Edition, McGraw Hill, 2006

[3.3] J. Cho, Electro-Mechanical Characterization of piezoelectrics for MEMS Power, M.S. Thesis, WSU, Department of Mechanical Engineering, 2004

[3.4] M. Robinson, Microstructural and Geometric Effects on the Piezoelectric Performance of PZT MEMS, PhD Dissertation, WSU, Department of Material Science Engineering, 2007

[3.5] H. Bardaweel, Dynamic Characterization of a Micro Heat Engine, MS Thesis, WSU, Department of Mechanical Engineering, 2007

[3.6] T. Trick, Introduction to Circuit Analysis, John Wiley & Sons, 1977

CHAPTER 4

MATERIAL PROPERTIES

In this chapter, the results from the characterization tests are presented. Tables of all measured and calculated parameters are given for all samples. Each sample tested in this study is described and a summary of its physical and electromechanical properties is given.

4.1 Table of Properties

As described in Chapter 3, all samples are fully characterized and the electromechanical parameters are reported below. These include the electrical parameters measured on the impedance analyzer, the electromechanical parameters calculated from the MATLAB code, the stiffness calculation performed and the other derived parameters that are calculated. All electrical and mechanical properties are tabulated, first for the open conditions and next for the closed conditions. Worth noting on this table are the resonant frequency, the coupling coefficient, the quality factor and stiffness. These are figures of merit for the ability of the sample to transduce mechanical to electrical energy and also the conditions (frequency and compliance) under which the sample can operate effectively. These samples have been chosen for this study to compare samples with different stiffness, resonant frequency and coupling characteristics. A more detailed description of each sample and its characteristics is given in Section 2.

4.1.1 Open Conditions

Sample	P3 PZT	PZT disk	PZT bender	PVDF	PFC
Area	5x5mm	15mm	11x30mm	12x20mm	10x30mm
Co - nF	27.427	20.814	93.819	0.832	0.504
R – kΩ	23.105	107.51	61.458	53436.0	70690.0
L – H	33.126	891.02	1919.3	962640	2885000
Cm - nF	0.0198	0.26304	0.78732	0.0018900	0.00038669
k^2	0.0007214	0.0125	0.0083	0.0014	0.0007663
f_n – Hz	6214.5	328.75	129.47	148.74	150.67
Q	55.98	17.12	25.4	16.84	38.64
$\bar{s}$ – N/m	881	258.7	253	15.5	67.6
1/s	0.00113507	0.00386548	0.00395257	0.06451613	0.0147929
S - m^2	0.000025	0.00017671	0.00033	0.00024	0.0003
m – kg	5.78E-07	6.04E-05	2.2523E-04	1.77E-05	7.54E-05
b - kg/s	0.00040304	0.00768372	0.017598	0.00098488	0.001848
ψ^2- N^2/V^2	1.74E-08	9.71E-08	3.36E-07	2.93E-11	2.61E-11

Table 4.1.1 Comparison of samples for open conditions

As Table 4.1.1 shows, each sample is listed by its name and area. C_o is the shunt capacitance and is measured in Farads. R is the electrical resistance measured in Ohms. L is the electrical load measured in Henrys. C_m is the mechanical capacitance measured in Farads. The electromechanical coupling is given as k^2 and is nondimensional. The natural frequency or resonant frequency is f_n and is given in Hertz. This can also be reported as ω_n which is radians/sec and is given by $\omega_n = 2\pi f_n$. Q is the mechanical quality factor and is nondimensional. Stiffness, s is measured in N/m and compliance is the inverse of stiffness. Area, S is measured in m^2. Effective mass m is given in kg. The damping coefficient, b is given in kg/s and ψ^2 is given in N^2/V^2.

4.1.2 Closed Conditions

Sample	P3 PZT	PZT disk	PZT bender	PVDF	PFC
Area	5x5mm	15mm	11x30mm	12x20mm	10x30mm
Co - nF	27.427	20.1	79.7	0.81	0.4802
R - kΩ	23.105	31.7	28.4	43597.0	10828.0
L - H	33.126	16.1169	4.3318	12628.0	5198.9
Cm - nF	0.0198	0.665	0.225	0.0020015	0.0014996
k^2	0.0007214	0.0319	0.0028	0.0025	0.0031
f - Hz	6214.5	1537.7	5102.7	1001.1	1802.5
Q	55.98	4.9137	4.8971	1.8219	5.4376
$\bar{s}$ - N/m	881	11600	53000	1820	8950
1/s	0.00113507	0.000086207	0.000018868	0.00054945	0.00011173
S - m^2	0.000025	0.00017671	0.00033	0.00024	0.0003
m - kg	5.7783E-07	1.2427E-04	5.1560E-05	4.6000E-05	6.9777E-05
b - kg/s	0.00040304	0.24434	0.33756	0.15881	0.14533
ψ^2 - N^2/V^2	1.7444E-08	7.7102E-06	1.1903E-05	3.6427E-09	1.3421E-08

Table 4.1.2 Comparison of samples for closed conditions

Table 4.1.2 shows the properties for all samples with closed conditions. As described for the open conditions, all of the electrical and mechanical properties are listed for comparison. It is worth noting that for all samples except the P3 PZT, the fully constrained conditions result in stiffness figures which are on the order of 100-200 times more than the open conditions. This translates to an increase in the resonant frequency, although these are closer to the order of 10 times.

4.2 Thin-Film PZT

A pre-existing project at WSU produces a micro-heat engine called the P3 engine (Palouse Piezoelectric Power Engine) [1]. One component of this engine is a piezoelectric generator membrane fabricated on-site using MEMS processes. This sample

is a thin-film PZT membrane which can produce electric power from source mechanical vibrations. This device is produced in 3mm, 5mm and 8mm versions. These dimensions refer to side length of a square membrane, so the areas are $9mm^2$, $25mm^2$, and $64mm^2$ respectively. The resonant frequency is 6000 Hz for the 5mm membrane as seen in Figure 4.2.1.

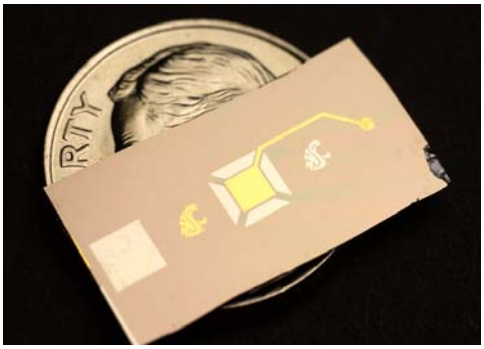

Figure 4.2.1 5x5mm thin film PZT sample

Because this sample is a fully constrained membrane on a Silicon wafer, the open and closed conditions are the same. From the tables above, the 5x5mm thin film PZT was found to have a resonant frequency of 6214.5 Hz, an electromechanical coupling coefficient of 0.00072, a mechanical quality factor of 55.98, and a stiffness of 881 N/m. This sample was characterized in this study, but it was not used for power data.

4.3 PZT Disk

Another sample chosen is a commercially available piezoelectric disk from APC International [2]. This product is available in a range of sizes from 10mm diameter to 20 mm diameter, with resonant frequencies from 3000 Hz to 9000 Hz. These consist of a layer of PZT with a silver electrode bonded to a brass disk and have a total thickness of

0.23mm. The sample that is used for all tests and results here has an electrode area of 15mm diameter and an overall diameter of 20 mm. As stated in Chapter 1, PZT is widely used because of its high electromechanical coupling. Because this is a bulk ceramic, it is fairly stiff, and this sample was chosen for its circular geometry and close size match to the closed sound tube size.

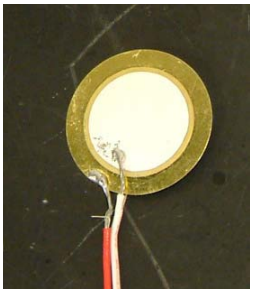

Figure 4.3.1 15mm PZT disk

For open conditions, the PZT disk has a resonant frequency of 333 Hz, an electromechanical coupling coefficient of 0.0125, a mechanical quality factor of 17.12, and a stiffness of 253 N/m.

For closed conditions, it has a resonant frequency of 1500 Hz, an electromechanical coupling coefficient of 0.0319, a mechanical quality factor of 4.9137, and a stiffness of 11600 N/m.

4.4 PZT Bender

Another sample chosen is a commercially available piezoelectric cantilever from APC International [3]. It consists of a central substrate of brass covered on both sides by a layer of PZT with an outer silver electrode layer and is 0.62mm thick. A wide variety of dimensions are available; the sample that is used in all tests has an electrode area of

11mm wide by 30mm long. This is the only sample with 2 layers of piezoelectric material or bimorph in the study. It was chosen to complement the PZT disk as another geometry available with this material.

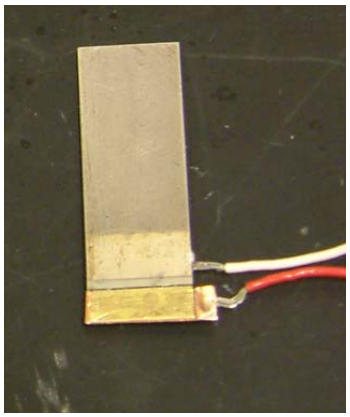

Figure 4.4.1 11x30mm PZT bender

For open conditions, the PZT bender has a resonant frequency of 210 Hz, an electromechanical coupling coefficient of 0.0083, a mechanical quality factor of 25.40, and a stiffness of 258.7 N/m.

For closed conditions, the PZT bender has a resonant frequency of 3100 Hz, an electromechanical coupling coefficient of 0.0028, a mechanical quality factor of 4.8971, and a stiffness of 53000 N/m.

4.5 Piezoelectric Fiber Composite

Another sample is a commercially available piezoelectric fiber composite or PFC from Advanced Cerametrics Incorporated [4]. It consists of bulk PZT extruded into fibers that are then embedded in an epoxy matrix and layered with interdigitated electrodes. A

unique feature about this construction is that it allows the manufacturer to pole domains along the fibers. This means that when used in a cantilever configuration, the sample operates in d_{33} mode because the mechanical force is in the 1 direction and the voltage is now harvested in the 1 direction [5]. These are available in a variety of sizes, and for these tests the sample used has an electrode area of 10mm wide by 30mm long. This sample was chosen because it has a medium stiffness and a unique electrode arrangement. Because the PZT has been formed into fibers, it is much more compliant than the other PZT samples in this study.

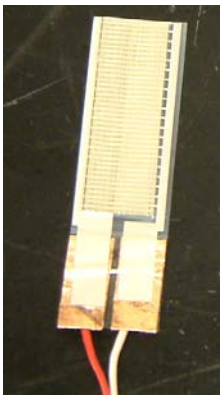

Figure 4.5.1 10x30mm PFC

For open conditions, the PFC has a resonant frequency of 135 Hz, an electromechanical coupling coefficient of 0.00077, a mechanical quality factor of 38.64, and a stiffness of 67.6 N/m.

For closed conditions, the PFC has a resonant frequency of 2000 Hz, an electromechanical coupling coefficient of 0.0031, a mechanical quality factor of 5.4376, and a stiffness of 8950 N/m.

4.6 PVDF

The final sample tested is a commercially available piezoelectric polymer polyvinylidene fluoride (PVDF) from Measurement Specialties [6]. It consists of the PVDF film which is 25 μm thick with a silver electrode on each side. This is bonded to a 125 μm thick polyester film on one face. This moves the PVDF film to one side of the center axis of the membrane which promotes straining of the film when used in bending mode (d_{31}). It is available in many sizes; for these tests the sample has an electrode area of 12mm wide by 20mm long. As stated in Chapter 1, PVDF is a unique and promising material. Its ferroelectric properties are desirable and because it is a polymer it is inexpensive to manufacture and is easily shaped. It is also unique in that its impedance closely matches water and biological tissue. It was chosen for this study because of its high compliance.

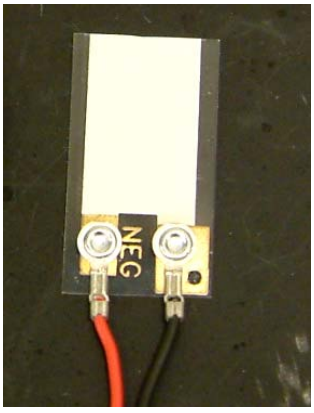

Figure 4.6.1 12x20mm PVDF

For open conditions, the PVDF has a resonant frequency of 140 Hz, an electromechanical coupling coefficient of 0.0014, a mechanical quality factor of 16.84, and a stiffness of 15.5 N/m.

For closed conditions, it has a resonant frequency of 1000 Hz, an electromechanical coupling coefficient of 0.0025, a mechanical quality factor of 1.8219, and a stiffness of 1820 N/m.

4.7 References:

[1] S. Whalen, M. Thompson, D. Bahr, C. Richards and R. Richards, "Design, fabrication and testing of the P^3 micro heat engine", Sensors and Actuators, A: Physical, vol. 104, No. 3, pp. 290-298, 2003.

[2] Product website: http://americanpiezo.com/products_services/disc_benders.html

[3] Website: http://americanpiezo.com/products_services/stripe_actuators.html

[4] Website: http://advancedcerametrics.com/pages/energy_harvesting_components/

[5] H. Sodano, J. Lloyd, and D. Inman, An experimental comparison between several active composite actuators for power generation, Smart Materials and Structures Vol. 15 (2006) pp. 1211-1216

[6] Website: http://www.meas-spec.com/myMeas/sensors/filmElements.asp

CHAPTER 5

ANALYSIS OF PROPERTIES –

COMPARISON OF NUMERICAL TO EXPERIMENTAL

In this chapter the procedure for validating the experimental results with a numerical model is presented. The numerical model is described and integrated into MATLAB. The procedure for running the numerical simulation and its comparison to the experimental results is outlined. Comparisons for all samples are given.

5.1 Numerical Model

The numerical model for energy conversion with a piezoelectric component is given in [1]. The equation for calculating electric impedance Z_e for a vacuum is as follows:

$$Z_e = \left[\frac{1}{j\omega C_o + \frac{1}{Z_L}} + j\omega \frac{m}{\psi^2} + \frac{R}{\psi^2} + \frac{\bar{s}}{j\omega\psi^2} \right] \tag{5.1}$$

This equation is used as the basis for a computer simulation run in MATLAB. The parameters C_o, $\bar{s}$, m, b, ψ^2 and sample area are used as inputs to the numerical model. The MATLAB program then calculates the impedance over a user specified frequency range and compares this numerical model to the experimental results graphically.

5.2 Procedure

Parameters for all samples are obtained as described in Chapter 3. Each sample is first tested in the vacuum chamber using the impedance analyzer. A separate test is then run to obtain stiffness. Next all parameters are calculated and recorded. The parameters for the sample are then entered into the MATLAB code as described in the previous section. The program is then executed and the results are reported graphically. The results from this procedure for all samples are shown in the next section.

5.3 Comparison

The output plot from the computer simulation for each sample is given which compares graphically the experimental results to the numerical model.

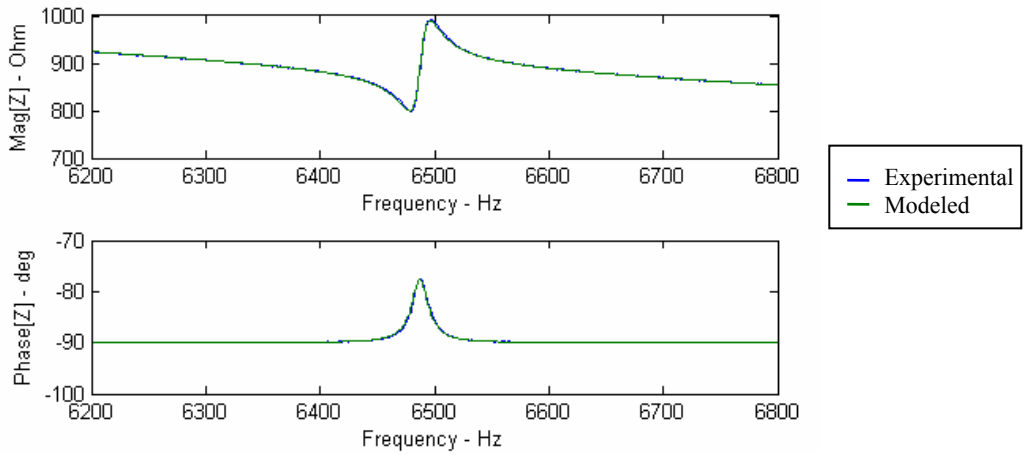

Figure 5.3.1 Comparison of numerical to experimental results for P3 PZT

Figure 5.3.1 shows the comparison of the numerical simulation to the experimental results from the impedance analyzer for the P3 PZT sample. The first graph

shows the magnitude of the impedance in Ω, the second graph shows the phase in degrees. The experimental results are shown by the blue line, the modeled electrical response is shown by the green line and the modeled mechanical response is shown by the red line. There is very good agreement between the experimental result and the numerical model for the P3 PZT which is evident by the very close match of the lines. This strong correlation gives confidence in the parameters as measured and calculated.

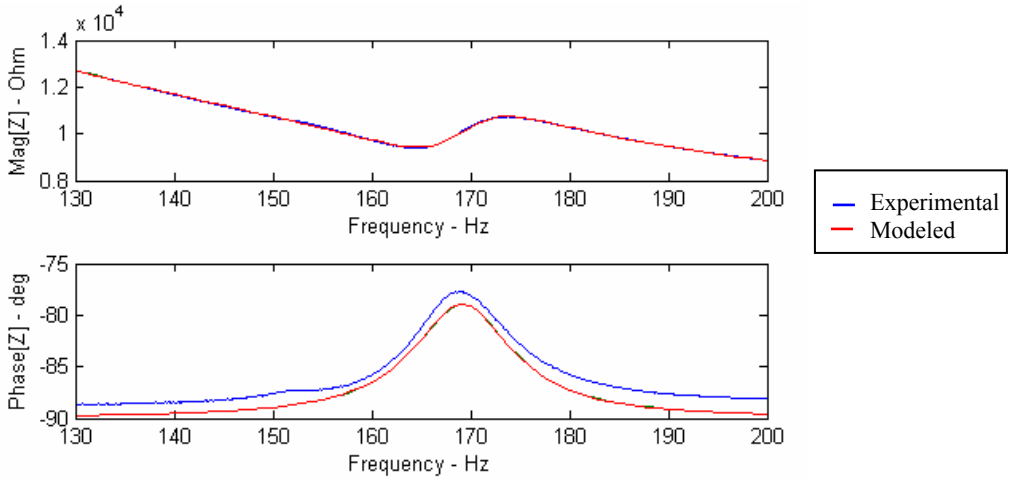

Figure 5.3.2 Comparison of numerical to experimental results for PZT bender

Figure 5.3.2 shows the comparison of the numerical simulation to the experimental results from the impedance analyzer for the PZT bender sample. The first graph shows the magnitude of the impedance in Ω, the second graph shows the phase in degrees. As above, the experimental results are shown by the blue line, the modeled electrical response is shown by the green line and the modeled mechanical response is shown by the red line. There is very good agreement between the experimental result and the numerical model for the PZT bender which is evident by the very close match of the

lines. This strong correlation gives confidence in the parameters as measured and calculated.

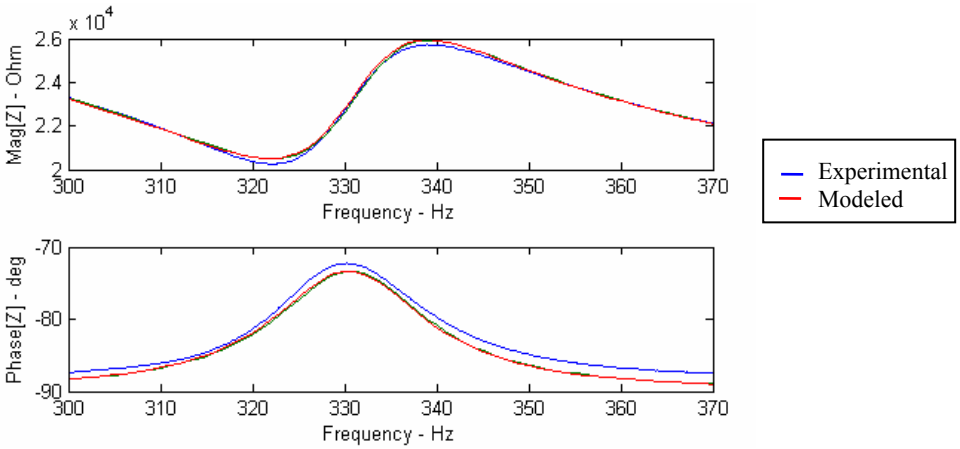

Figure 5.3.3 Comparison of numerical to experimental results for PZT disk

Figure 5.3.3 shows the comparison of the numerical simulation to the experimental results from the impedance analyzer for the PZT disk sample. The first graph shows the magnitude of the impedance in Ω, the second graph shows the phase in degrees. The first graph shows the magnitude of the impedance in Ω, the second graph shows the phase in degrees. As above, the experimental results are shown by the blue line, the modeled electrical response is shown by the green line and the modeled mechanical response is shown by the red line. There is good agreement between the experimental result and the numerical model for the PZT disk which is evident by the close match of the lines. There is some deviation, but overall the correlation gives confidence in the parameters as measured and calculated.

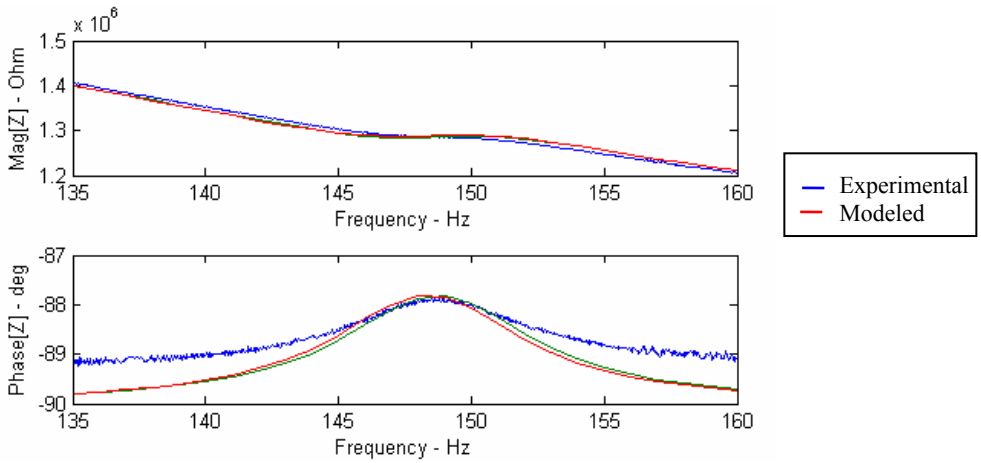

Figure 5.3.4 Comparison of numerical to experimental results for PVDF

Figure 5.3.4 shows the comparison of the numerical simulation to the experimental results from the impedance analyzer for the PVDF sample. The first graph shows the magnitude of the impedance in Ω, the second graph shows the phase in degrees. As above, the experimental results are shown by the blue line, the modeled electrical response is shown by the green line and the modeled mechanical response is shown by the red line. There is good agreement between the experimental result and the numerical model for the PVDF which is evident by the match of the lines. There is some deviation, but overall the correlation gives confidence in the parameters as calculated.

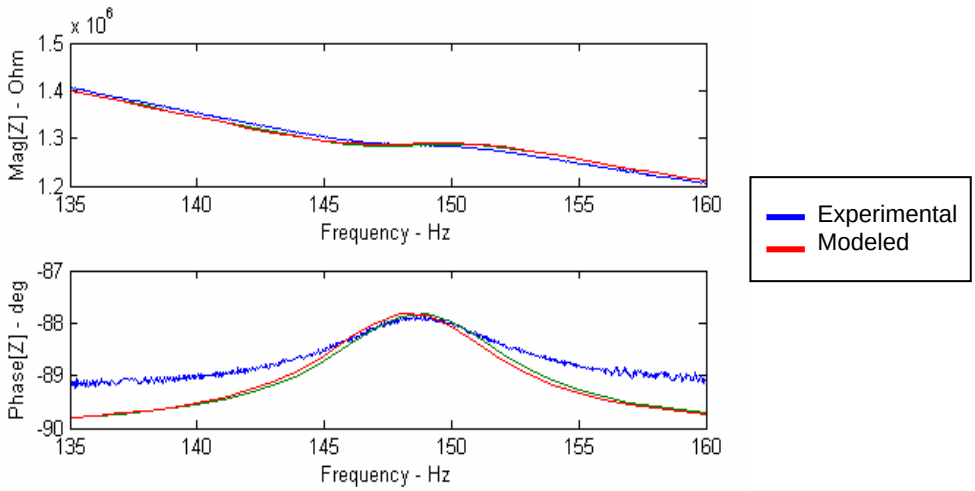

Figure 5.3.5 Comparison of numerical to experimental results for PFC

Figure 5.3.5 shows the comparison of the numerical simulation to the experimental results from the impedance analyzer for the PFC sample. The first graph shows the magnitude of the impedance in Ω, the second graph shows the phase in degrees. As above, the experimental results are shown by the blue line, the modeled electrical response is shown by the green line and the modeled mechanical response is shown by the red line. There is good agreement between the experimental result and the numerical model for the PFC which is evident by the match of the lines. There is some deviation, but overall the correlation gives confidence in the parameters as calculated.

5.4 References:

[1] C.D. Richards, M.J. Anderson, D.F. Bahr, and R.F. Richards, Efficiency of energy conversion for devices containing a piezoelectric component. *Journal of Micromechanics and Microengineering, 14* (2004) 717-721.

CHAPTER 6

RESULTS

In this chapter, experimental results are presented from the sound tube with both open and closed conditions and also from the open and closed thermoacoustic engines. The power output results are then normalized by surface area to facilitate comparison between samples. Conversion efficiency calculations are shown by comparing the electric power measured against the calculated acoustic power. Based on the experimental results, a simple numerical model is constructed which models the power output for a range of acoustic pressures. Finally, the results of the samples are compared and discussed.

6.1 Open Condition Sound Tube and Thermoacoustic Engine

As described in Chapter 2 each sample was clamped on one edge creating a cantilever and placed in front of the open sound tube at a distance of 5mm, simulating the conditions of a standing wave closed-open thermoacoustic engine with a pressure release termination. Under these conditions, frequency was varied to find the resonant frequency of the sample, and pressure was also varied to find the power output increase due to increasing acoustic pressure. This pressure was measured with the microphone in the same plane as the sample. With this experimental setup, the frequency range of interest was between 80 Hz and 1000 Hz and the acoustic pressures were fixed at 6.4 Pa, 19.1 Pa and 38.2 Pa RMS. The large open thermoacoustic engine was then used as the acoustic driver for all of the samples. As stated in Chapter 3, this engine consisted of a test tube

measuring 22.5mm in diameter and 200mm long with a porous ceramic stack 15mm in length located 140mm from the end with the sample. It produced a standing acoustic wave of 430 Hz with an acoustic pressure of 89 Pa RMS which equates to an SPL of 133 dB re 20μPa. An error analysis was performed for each setup and was found to be 23.1%. Error bars are displayed on power output graphs of each sample. The complete error calculation is given in Appendix A. Results for each sample under these open conditions are reported below.

6.1.1 Open PFC

Piezoelectric Fiber Composite material, or PFC, was cantilevered 5mm from the opening of the sound tube and power measurements were made with the variable load resistor. Under resonant conditions, it was found that peak power was produced with a 9 MΩ load.

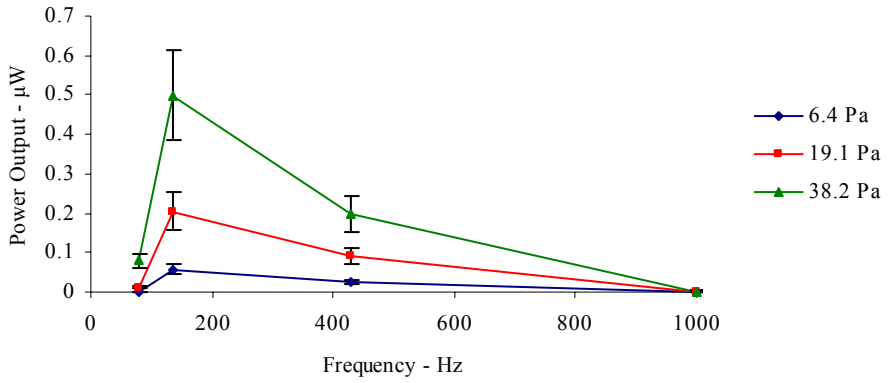

Figure 6.1.1 Frequency Response for PFC open conditions

Figure 6.1.1 shows the power output data for PFC over a range of frequencies below and above resonance. As the graph shows, below 80 Hz the PFC sample produces less than 0.1 μW for all acoustic pressures. Between 80-135 Hz, power output increases noticeably. The power output peak at a frequency of 135 Hz corresponds with the resonant frequency for the PFC 13x30mm sample under these conditions. At frequencies above this, power drops off the same as it did below resonant condition, so that above 400Hz the power output is less than 0.2 μW for all acoustic pressures tested. The data shows that a peak power of 0.5 μW was produced at the resonant frequency of 135 Hz with an acoustic pressure of 38.2 Pa.

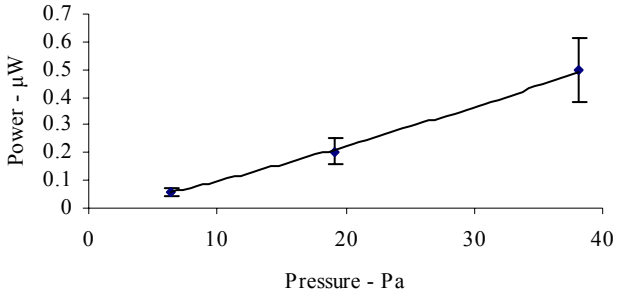

Figure 6.1.2 Pressure Response for PFC at resonant frequency

Figure 6.1.2 shows the power output for the PFC at 135 Hz with increasing acoustic pressure amplitudes. The points represent the data collected experimentally. This pressure response curve shows how the PFC sample responds to changes in acoustic pressure. Using the least squares fit method referred to in Chapter 3 the solid line is obtained given by the following equation:

$$\Pi = 0.006p^{1.2} \qquad (6.1)$$

Where Π is time averaged power in Watts and p is acoustic pressure in Pa. This result is indicative of the pressure response curves for the other frequencies tested.

The PFC sample was then tested on the large open thermoacoustic engine operating at 430 Hz. The sample produced 0.54 μW of electric power at an acoustic pressure of 89 Pa. This was compared to the results from the sound tube as seen below.

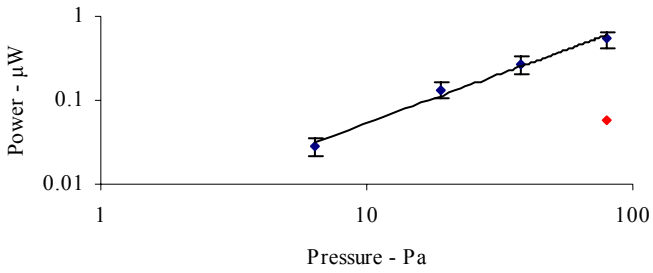

Figure 6.1.3 Pressure Response for PFC at 430 Hz

Figure 6.1.3 shows the power output for the PFC at 430 Hz on a logarithmic scale. This compares the experimental results from the open sound tube operating between 6.4 Pa and 89 Pa shown in blue to the results from the open thermoacoustic engine operating at 89 Pa shown in red. As the graph shows, there is very good agreement between all of the values obtained on the sound tube, but there is a discrepancy between those values and the thermoacoustic engine. These tests were run multiple times and were shown to be repeatable results. The PFC sample may change the operating conditions of the thermoacoustic engine, but it is unclear what this effect may be. The PFC sample was also tested on two experimental thermoacoustic engines: one operating at 850 Hz and one operating at 1250 Hz. At 830 Hz the sample produced 116 nW of electric power at an acoustic pressure of 60 Pa and at 1250 Hz the sample produced 30.2 nW at 62 Pa.

All of the data points for PFC were then plotted on a 3D mesh which shows the interpolation of power output for any combination of frequency and acoustic pressure within the dynamic range of the experimental setup. This is shown graphically below.

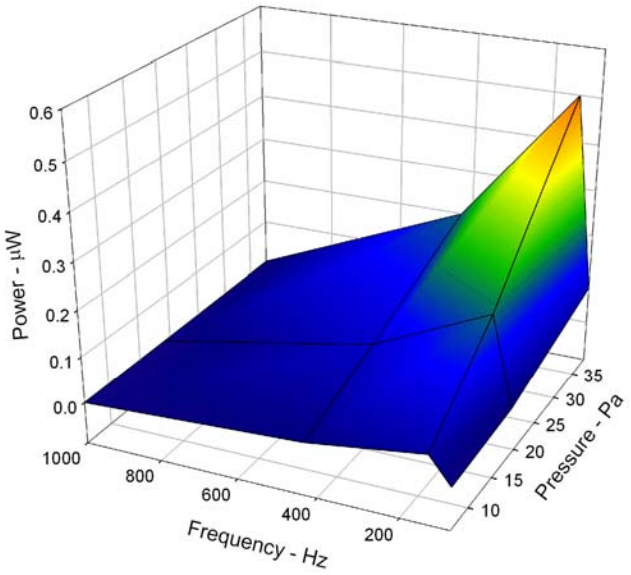

Figure 6.1.4 Power Output Plot for PFC open conditions

As Figure 6.1.4 shows, power output increases significantly as the driving frequency approaches the natural resonance of the sample. The sharp peak of power output at resonance indicates that there is a very narrow range of resonance conditions. As was previously stated the peak power of 0.5 µW is generated at a frequency of 135 Hz, with an electrical load of 9 MΩ at an acoustic pressure of 38.2 Pa. This pressure is significantly less than the pressures in a closed thermoacoustic engine, but these results give a good indication of the power that can be obtained from an acoustic source. To extrapolate what may be expected by coupling the PFC sample to an open standing wave

thermoacoustic engine, the power output formula that was generated from the pressure response curves was used to generate a numerical model of power output for a wider range of pressures. This is shown in Section 5.

6.1.2 Open PVDF

Polyvinylidene fluoride, or PVDF, material was cantilevered 5mm from the opening of the sound tube and power measurements were made with the variable load resistor. Under resonant conditions, it was found that peak power was produced with a 3 MΩ load.

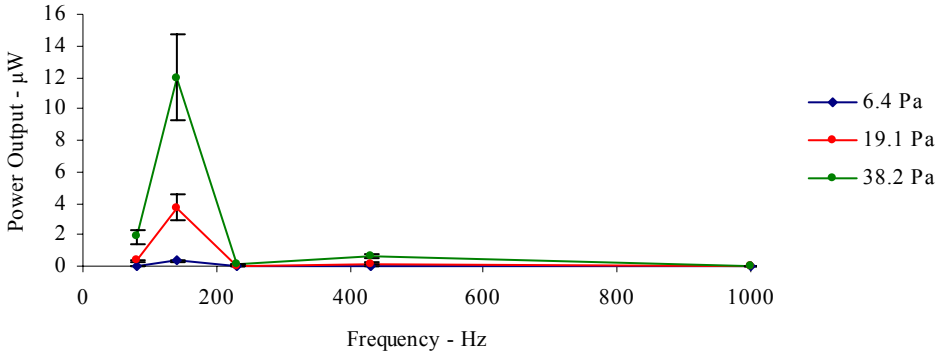

Figure 6.1.5 Frequency Response for PVDF open conditions

Figure 6.1.5 shows the power output data for PVDF over a range of frequencies below and above resonance. As the graph shows, below 80 Hz the PVDF sample produces less than $6x10^{-6}$ W for all acoustic pressures. Between 80-140 Hz, power output increases dramatically. The power output peak at a frequency of 140 Hz corresponds with the resonant frequency for the PVDF 12x20mm sample under these conditions. At frequencies above this, power drops off the same as it did below resonant condition, so

that above 230Hz the power output is less than $3x10^{-7}$ W for all acoustic pressures tested. The data shows that a peak power of 12 μW was produced at 140 Hz with an acoustic pressure of 38.2 Pa.

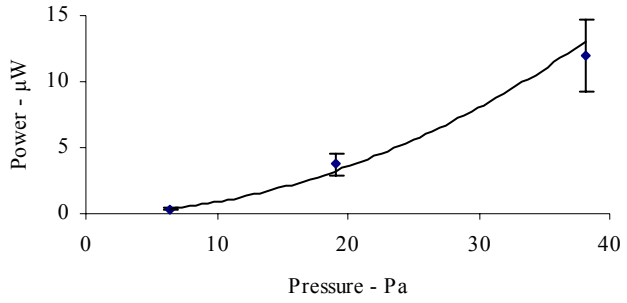

Figure 6.1.6 Pressure Response for PVDF at resonant frequency

Figure 6.1.6 shows the power output for the PVDF at 140 Hz with increasing acoustic pressure amplitudes. The points represent the data collected experimentally. This pressure response curve shows how the PVDF sample responds to changes in acoustic pressure. Using the least squares fit method referred to in Chapter 3 the solid line is obtained given by the following equation:

$$\Pi = 0.0087 p^{2.0} \qquad (6.2)$$

Where Π is time averaged power in Watts and p is acoustic pressure in Pa. This result is indicative of the pressure response curves for the other frequencies tested.

This equation shows that the PVDF sample produces power proportional to a square of the acoustic pressure as $\Pi \approx p^2$. This is reasonable, since acoustic power itself is related to acoustic pressure squared for a given area, medium and impedance [6.1].

The PVDF sample was then tested on the large open thermoacoustic engine operating at 430 Hz. The sample produced 2.3 μW of electric power at an acoustic pressure of 89 Pa. This was compared to the results from the sound tube as seen below.

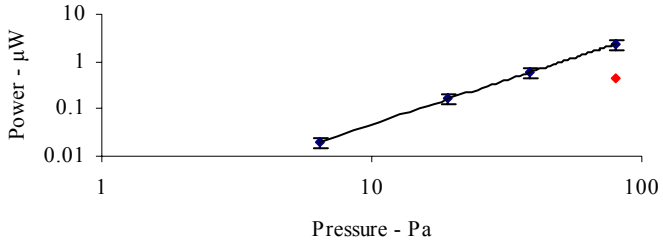

Figure 6.1.7 Pressure Response for PVDF at 430 Hz

Figure 6.1.7 shows the power output for the PVDF at 430 Hz on a logarithmic scale. This compares the experimental results from the open sound tube operating between 6.4 Pa and 89 Pa to the results from the open thermoacoustic engine operating at 89 Pa shown in red. As the graph shows, there is good agreement between all of the values obtained on the sound tube, but there is a discrepancy between that and the thermoacoustic engine. These tests were run multiple times and were shown to be repeatable results. The PVDF sample may change the operating conditions of the thermoacoustic engine, but it is unclear what this affect may be. The PVDF sample was also tested on an experimental thermoacoustic engine operating at 1250 Hz and produced 1.65 μW of electric power at an acoustic pressure of 62 Pa.

All of the data points for PVDF from the sound tube were then plotted on a 3D mesh which shows the interpolation of power output for any combination of frequency

and acoustic pressure within the dynamic range of the experimental setup. This is shown graphically in Figure 6.1.8.

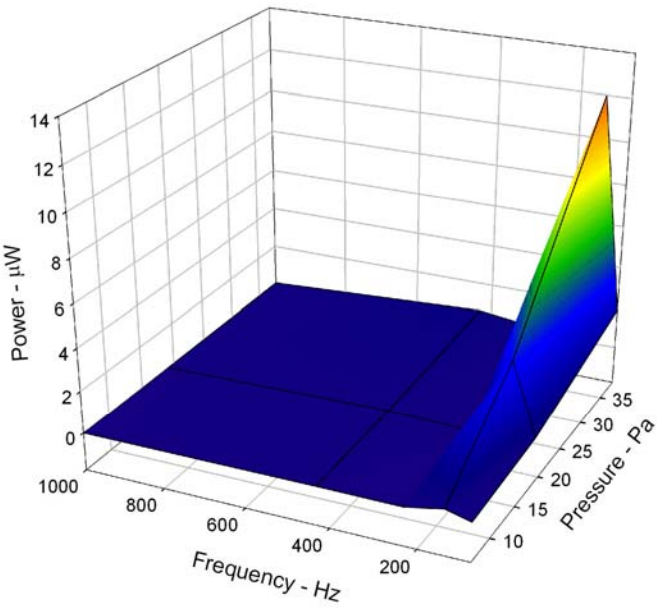

Figure 6.1.8 Power Output Plot for PVDF open conditions

As Figure 6.1.8 shows, power output increases significantly as the driving frequency approaches the natural resonance of the sample. The sharp apparent peak of power output at resonance indicates that there is a very narrow range of resonance conditions. As was previously stated, the peak power of 12 µW is generated at a frequency of 140 Hz with an electrical load of 3 MΩ at an acoustic pressure of 38.2 Pa. This pressure is significantly less than the pressures in a closed thermoacoustic engine, but these results give a good indication of the power that can be obtained from an acoustic source. To extrapolate what may be expected by coupling the PVDF sample to an open standing wave thermoacoustic engine, the power output formula that was

generated from the pressure response curves was used to generate a numerical model of power output for a wider range of pressures. This is shown in Section 5.

6.1.3 Open PZT Disk

A disk of lead zirconate titanate, or PZT, material was cantilevered 5mm from the opening of the sound tube and power measurements were made with the variable load resistor. Under resonant conditions, it was found that peak power was produced with a 30 kΩ load.

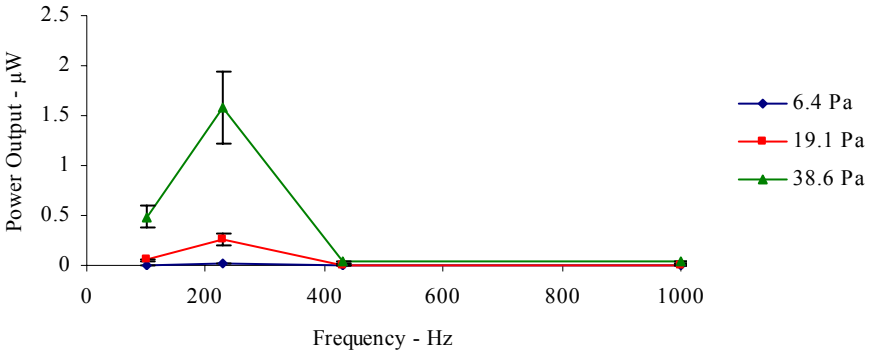

Figure 6.1.9 Frequency Response for PZT disk open conditions

Figure 6.1.9 shows the power output data for the PZT disk over a range of frequencies below and above resonance. As the graph shows, below 100 Hz the sample produces less than $5x10^{-7}$ W for all acoustic pressures. Between 100-230 Hz, power output increases dramatically. The power output peak at a frequency of 230 Hz corresponds with the resonant frequency for the 15mm PZT disk under these conditions. At frequencies above this, power drops off the same as it did below resonant condition, so that above 430 Hz the power output is less than $4x10^{-8}$ W for all acoustic pressures

tested. The data shows that a peak power of 1.6 μW was produced at 230 Hz with an acoustic pressure of 38.2Pa.

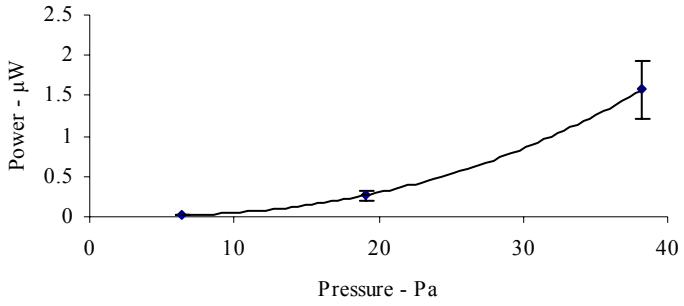

Figure 6.1.10 Pressure Response for PZT disk at resonant frequency

Figure 6.1.10 shows the power output for the PZT disk at 230 Hz with increasing acoustic pressure amplitudes. The points represent the data collected experimentally. This pressure response curve shows how the sample responds to changes in acoustic pressure. Using the least squares fit method referred to in Chapter 3 the solid line is obtained given by the following equation:

$$\Pi = 0.0001p^{2.56} \qquad (6.3)$$

Where Π is time averaged power in Watts and p is acoustic pressure in Pa. This result is indicative of the pressure response curves for the other frequencies tested.

The PZT disk was then tested on the large open thermoacoustic engine operating at 430 Hz. The sample produced 1.17 μW of electric power at an acoustic pressure of 89 Pa. This was compared to the results from the sound tube as seen below.

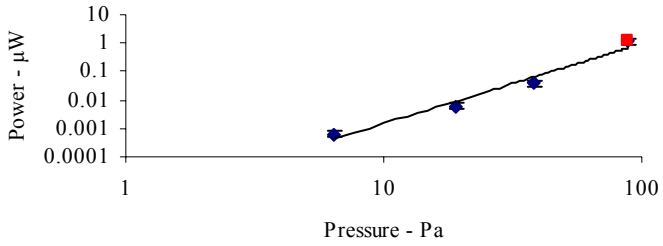

Figure 6.1.11 Pressure Response for PZT disk at 430 Hz

Figure 6.1.11 shows the power output for the PZT disk at 430 Hz on a logarithmic scale. This compares the experimental results from the open sound tube operating between 6.4 Pa and 38.2 Pa to the results from the open thermoacoustic engine operating at 89 Pa shown in red. As the graph shows, there is good agreement between all of the values obtained. The PZT disk sample was also tested on an experimental thermoacoustic engine operating at 1250 Hz and produced 0.16 µW of electric power at an acoustic pressure of 62 Pa.

All of the data points for the PZT disk were then plotted on a 3D mesh which shows the interpolation of power output for any combination of frequency and acoustic pressure within the dynamic range of the experimental setup. This is shown graphically below.

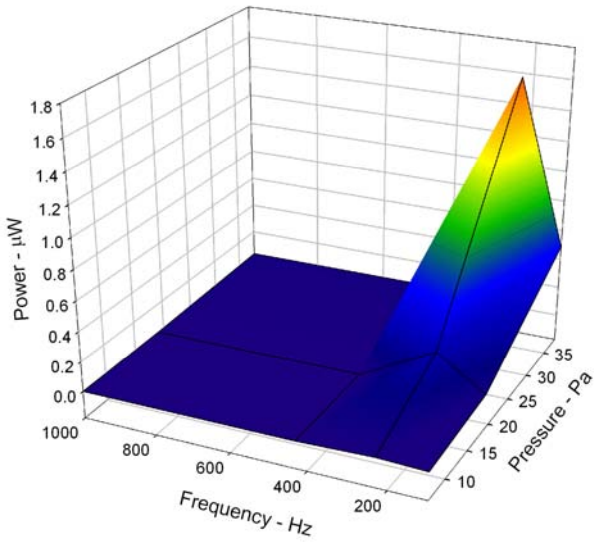

Figure 6.1.12 Power Output Plot for PZT disk open conditions

As Figure 6.1.12 shows, power output increases significantly as the driving frequency approaches the natural resonance of the sample. The sharp apparent peak of power output at resonance indicates that there is a very narrow range of resonance conditions. As was previously stated the peak power of 1.2 µW is generated at a frequency of 230 Hz, with an electrical load of 30 kΩ, and an acoustic pressure of 38.2 Pa. This pressure is significantly less than the pressures in a closed TA engine, but these results give a good indication of the power that can be obtained from an acoustic source. To extrapolate what may be expected by coupling the PZT disk to an open standing wave thermoacoustic engine, the power output formula that was generated from the pressure response curves was used to generate a numerical model of power output for a wider range of pressures. This is shown in Section 5.

6.1.4 Open PZT Bender

A PZT bender was cantilevered 5mm from the opening of the sound tube and power measurements were made with the variable load resistor. Under resonant conditions, it was found that peak power was produced with a 10 kΩ load.

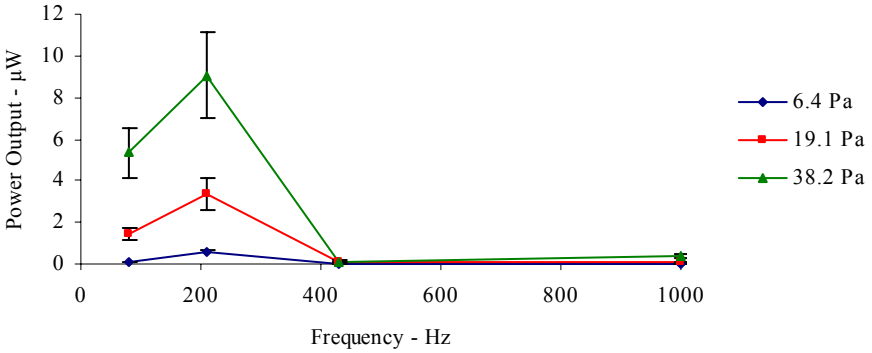

Figure 6.1.13 Frequency Response for PZT bender open conditions

Figure 6.1.13 shows the power output data for PZT bender over a range of frequencies below and above resonance. As the graph shows, below 80 Hz the sample produces less than $5x10^{-6}$ W for all acoustic pressures. Between 100-210 Hz, power output increases dramatically. The power output peak at a frequency of 210 Hz corresponds with the resonant frequency for the 11x30mm PZT bender under these conditions. At frequencies above this, power drops off the same as it did below resonant condition, so that above 430 Hz the power output is less than $4x10^{-7}$ W for all acoustic pressures tested. The data shows that a peak power of 9.1 µW was produced at 210 Hz with an acoustic pressure of 38.2 Pa.

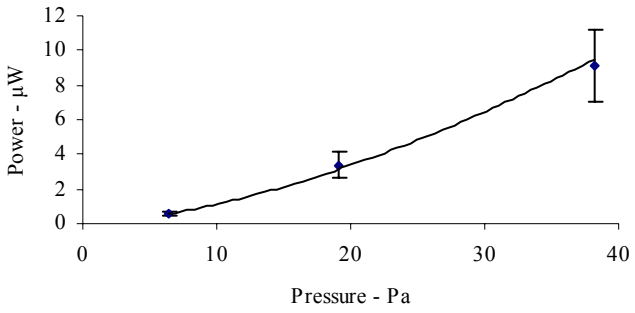

Figure 6.1.14 Pressure response for PZT bender at resonant frequency

Figure 6.1.14 shows the power output for the PZT bender at 210 Hz with increasing acoustic pressure amplitudes. The points represent the data collected experimentally. This pressure response curve shows how the sample responds to changes in acoustic pressure. Using the least squares fit method referred to in Chapter 3 the solid line is obtained given by the following equation:

$$\Pi = 0.028p^{1.6} \qquad (6.4)$$

Where Π is time averaged power in Watts and p is RMS acoustic pressure in Pa. This result is indicative of the pressure response curves for the other frequencies tested.

The PZT bender was then tested on the large open thermoacoustic engine operating at 430 Hz. The sample produced 0.13 μW of electric power at an acoustic pressure of 80 Pa. This was compared to the results from the sound tube as seen below.

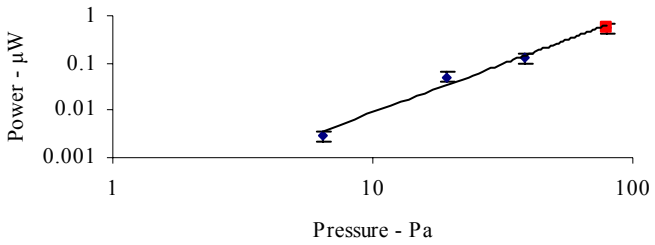

Figure 6.1.15 Pressure response for PZT bender at 430 Hz

Figure 6.1.15 shows the power output for the PZT bender at 430 Hz on a logarithmic scale. This compares the experimental results from the open sound tube operating between 6.4 Pa and 38.2 Pa to the results from the open thermoacoustic engine operating at 79 Pa as shown in red. As the graph shows, there is good agreement between all of the values obtained. The PZT bender sample was also tested on an experimental thermoacoustic engine operating at 1250 Hz and produced 0.22 µW of electric power at an acoustic pressure of 88 Pa.

All of the data points for the PZT bender were then plotted on a 3D mesh which shows the interpolation of power output for any combination of frequency and acoustic pressure within the dynamic range of the experimental setup. This is shown below.

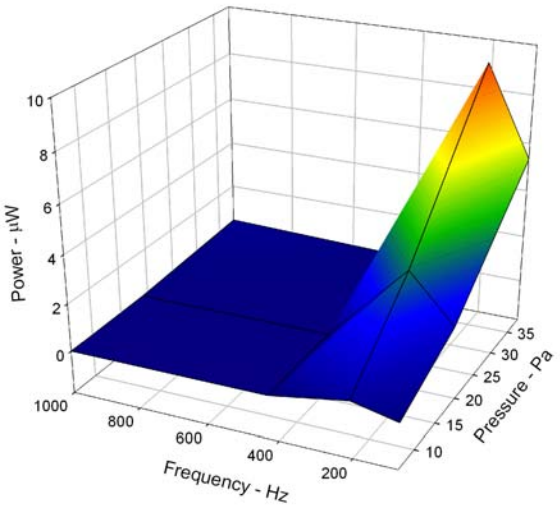

Figure 6.1.16 Power Output Plot for PZT bender open conditions

As Figure 6.1.16 shows, power output increases significantly as the driving frequency approaches the natural resonance of the sample. As was previously stated the peak power of 9.1 µW is generated at a frequency of 210 Hz, with an electrical load of 10 kΩ, and an RMS acoustic pressure of 38.2 Pa. This pressure is significantly less than the pressures in a closed thermoacoustic engine, but these results give a good indication of the power that can be obtained from an acoustic source. To extrapolate what may be expected by coupling the bender sample to an open standing wave thermoacoustic engine, the power output formula that was generated from the pressure response curves was used to generate a numerical model of power output for a wider range of pressures. This is shown in Section 5.

6.2 Closed Condition Sound Tube and Thermoacoustic Engine

As described in Chapter 2, each sample was attached to the end of the sound tube over a 10mm diameter opening, simulating the conditions of a standing wave closed-closed thermoacoustic engine with the sample as the termination. Under these conditions, frequency was varied to find the resonant frequency of the sample, and pressure was also varied to find the power output increase due to increasing acoustic pressure. With this experimental setup, the frequency range of interest was between 430 Hz and 3100 Hz and the acoustic pressures were fixed at 6.4 Pa, 19.1 Pa and 38.2 Pa RMS.

The long closed thermoacoustic engine was used as the acoustic driver for all of the samples. As stated in Chapter 2, this engine consisted of a Pyrex tube measuring 22.5mm in diameter and 375mm long with a porous ceramic stack 15mm in length located 290mm from the end holding the sample. This engine produced a standing acoustic wave of 470 Hz with an acoustic pressure of 726 Pa RMS which equates to an SPL of 151 dB re 20μPa. An error analysis was performed for each setup with the results reported for each sample. The complete calculation is given in appendix. All results for the samples under these conditions are reported below.

6.2.1 Closed PFC

The piezoelectric fiber composite sample, or PFC, was fully constrained over the 10mm diameter opening on the sound tube, and power measurements were made with the variable load resistor. Under resonant conditions, it was found that peak power was produced with a 100 kΩ load.

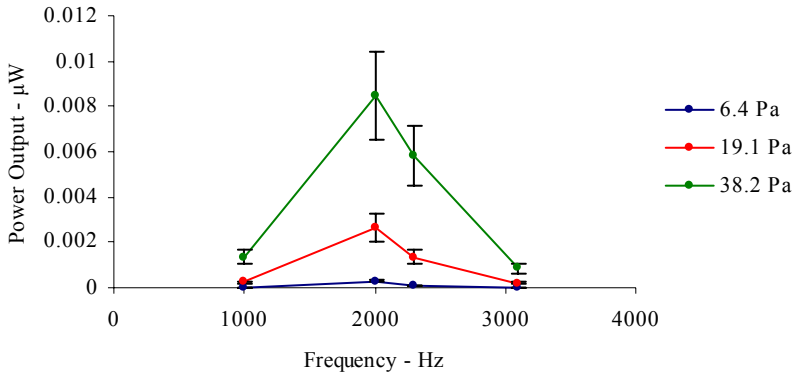

Figure 6.2.1 Frequency Response for PFC closed conditions

Figure 6.2.1 shows the power output data for PFC over a range of frequencies below and above resonance. As the graph shows, below 1000 Hz the PFC sample produces less than $2x10^{-10}$ W for all acoustic pressures. From 1000-2000Hz, power output increases noticeably. The power output peak at a frequency of 2000 Hz corresponds with the resonant frequency for the PFC 13x30mm sample under these conditions. Above resonance frequency, power drops off the same as it did below resonant condition, so that above 3000Hz the power output is again less than $2x10^{-10}$ W for all acoustic pressures tested. The data shows that a peak power of 1.05 nW was produced at 2000 Hz with an acoustic pressure of 38.2 Pa.

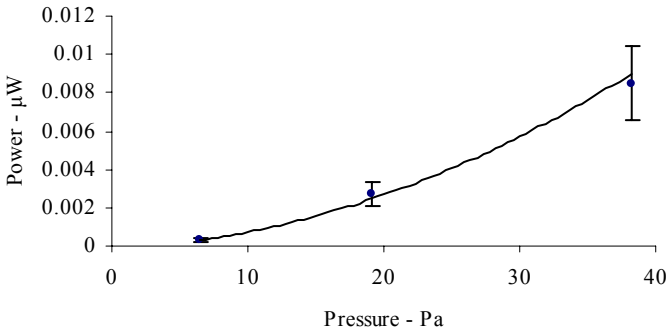

Figure 6.2.2 Pressure Response for PFC at resonant frequency

Figure 6.2.2 shows the power output for the PFC at 2000 Hz with increasing acoustic pressure amplitudes. The points represent the data collected experimentally. This pressure response curve shows how the PFC sample responds to changes in acoustic pressure. Using the least squares fit method referred to in Chapter 3 the solid line is obtained given by the following equation:

$$\Pi = 0.00001p^{1.87} \qquad (6.5)$$

Where Π is time averaged power in Watts and p is acoustic pressure in Pa. This result is indicative of the pressure response curves at the other frequencies tested.

The PFC sample was then tested on the long closed thermoacoustic engine operating at 470 Hz. The sample produced 1.95 μW of electric power at an acoustic pressure of 796 Pa. This was compared to the results from the sound tube as seen below.

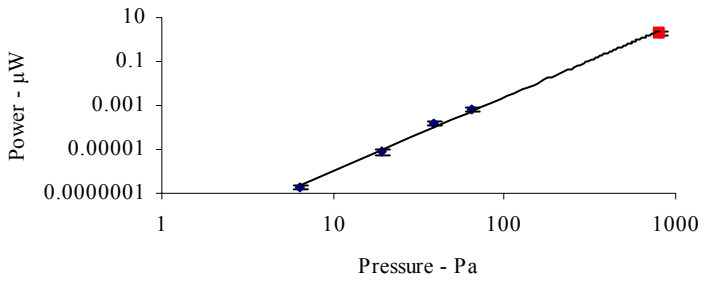

Figure 6.2.3 Pressure Response for PFC at 470 Hz

Figure 6.2.3 shows the power output for the PFC at 470 Hz on a logarithmic scale. This compares the results from the open sound tube operating between 6.4 Pa and 64 Pa to the results from the open thermoacoustic engine operating at 796 Pa as shown in red. As the graph shows, there is very good agreement between all of the values obtained.

All of the data points for PFC were then plotted on a 3D mesh which shows the interpolation of power output for any combination of frequency and acoustic pressure within the dynamic range of the experimental setup. This is shown graphically below.

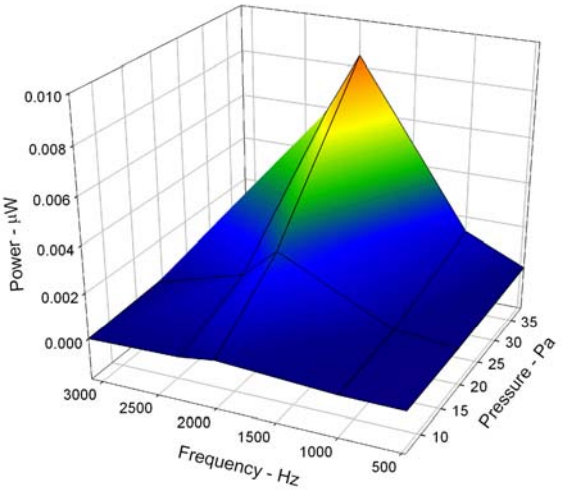

Figure 6.2.4 Power Output Plot for PFC closed conditions

As Figure 6.2.4 shows, power output increases significantly as the driving frequency approaches the natural resonance of the sample, and as was previously stated the peak power of 1.05 nW is generated at a frequency of 2000 Hz, with an electrical load of 100 kΩ, and an acoustic pressure of 38.2 Pa. This pressure is significantly less than the pressures in a closed TA engine, but these results give a good indication of the power that can be obtained from an acoustic source. To extrapolate what may be expected by coupling the PFC sample to a closed standing wave thermoacoustic engine, the power output formula that was generated from the pressure response curves was used to generate a numerical model of power output for a wider range of pressures. This is shown in Section 5.

6.2.2 Closed PVDF

Polyvinylidene fluoride, or PVDF, material was fully constrained over the 10mm diameter opening, and power measurements were made with the variable load resistor. Under resonant conditions, peak power was produced with a 200 kΩ load.

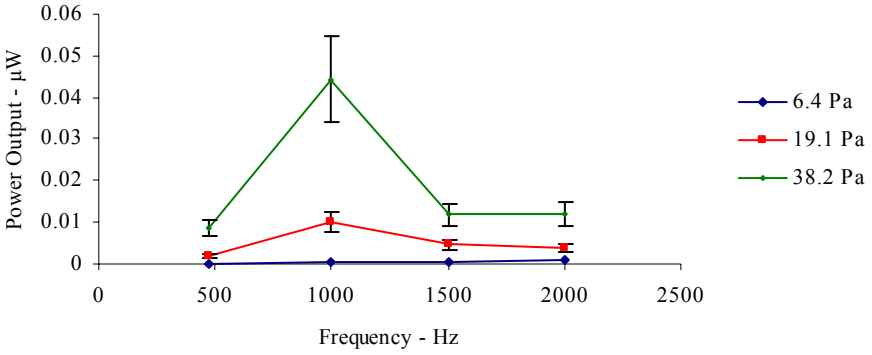

Figure 6.2.5 Frequency Response for PVDF closed conditions

Figure 6.2.5 shows the power output data for PVDF over a range of frequencies below and above resonance. As the graph shows, below 500 Hz the PVDF sample produces less than $1x10^{-8}$ W for all acoustic pressures. From 500-1000Hz, power output increases noticeably. The power output peak at a frequency of 1000 Hz corresponds with the resonant frequency for the PVDF 12x20mm sample under these conditions. Above resonance frequency, power drops off the same as it did below resonant condition, so that above 1500Hz the power output is again less than $1x10^{-8}$ W for all acoustic pressures tested. The data shows that a peak power of 44.4 nW was produced at 1000 Hz with an acoustic pressure of 38.2 Pa.

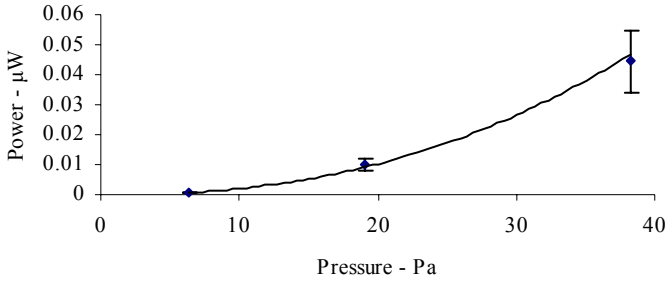

Figure 6.2.6 Pressure Response for PVDF at resonant frequency

Figure 6.2.6 shows the power output for the PVDF at 1000 Hz with increasing acoustic pressure amplitudes. The points represent the data collected experimentally. This pressure response curve shows how the PVDF sample responds to changes in acoustic pressure. Using the least squares fit method referred to in Chapter 3 the solid line is obtained given by the following equation:

$$\Pi = 0.000009p^{2.33} \tag{6.6}$$

Where Π is time averaged power in Watts and p is acoustic pressure in Pa. This result is indicative of the pressure response curves for the other frequencies tested. This shows that the PVDF sample produces power proportional to a square of the acoustic pressure.

The PVDF sample was then tested on the long closed thermoacoustic engine operating at 470 Hz. The sample produced 0.98 μW of electric power at an acoustic pressure of 726 Pa. This was compared to the results from the sound tube as seen below.

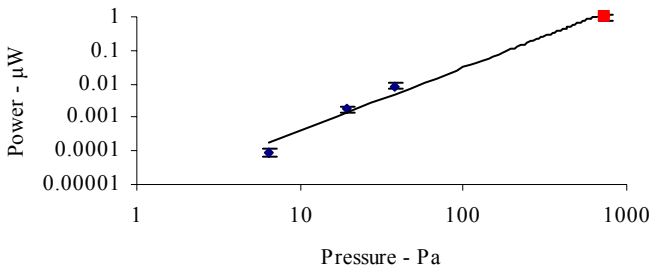

Figure 6.2.7 Pressure Response for PVDF at 470 Hz

Figure 6.2.7 shows the power output for the PVDF at 470 Hz on a logarithmic scale. This compares the experimental results from the open sound tube operating between 6.4 Pa and 38.2 Pa to the results from the open thermoacoustic engine operating at 726 Pa shown in red. The graph shows there is good agreement between all values.

All of the data points for PVDF were then plotted on a 3D mesh which shows the interpolation of power output for any combination of frequency and acoustic pressure within the dynamic range of the experimental setup. This is shown graphically below.

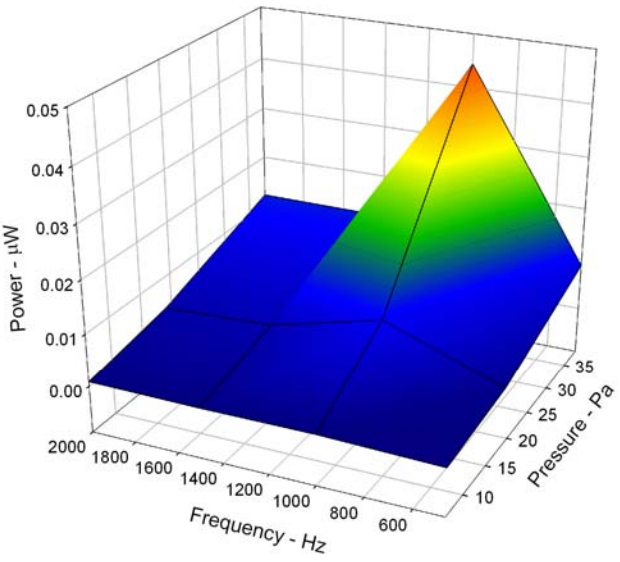

Figure 6.2.8 Power Output Plot for PVDF closed conditions

As this plot shows, power output increases significantly as the driving frequency approaches the natural resonance of the sample, and as was previously stated the peak power of 44.4 nW is generated at a frequency of 1000 Hz, with an electrical load of 200 kΩ at an acoustic pressure of 38.2 Pa. This pressure is significantly less than the pressures generated in a closed thermoacoustic engine, but these results give a good indication of the power that can be obtained from an acoustic source. To extrapolate what may be expected by coupling the PVDF sample to a closed standing wave thermoacoustic engine, the power output formula that was generated from the pressure response curves was used to generate a numerical model of power output for a wider range of pressures. This is shown in Section 5.

6.2.3 Closed PZT Disk

A disk of Lead Zirconate Titanate, or PZT, material was fully constrained over the 10mm diameter opening, and power measurements were made with the variable load resistor. Under resonant conditions, peak power was produced with a 5 kΩ load.

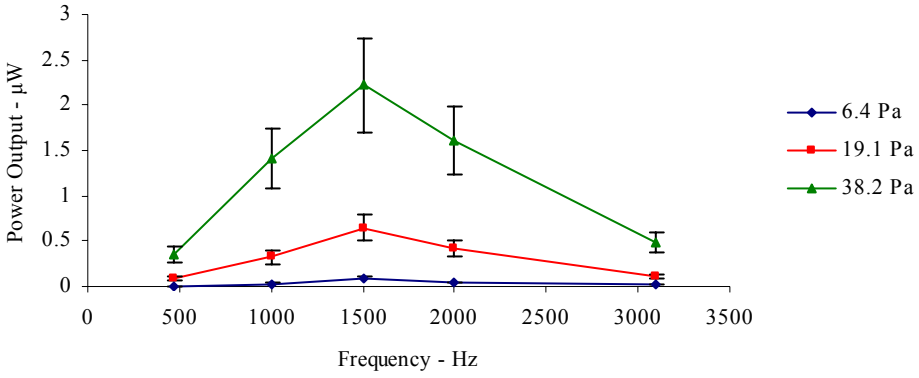

Figure 6.2.9 Frequency Response for PZT disk closed conditions

Figure 6.2.9 shows the power output data for the PZT disk over a range of frequencies below and above resonance. As the graph shows, below 500 Hz the sample produces less than $4x10^{-7}$ W for all acoustic pressures. From 500-1500Hz, power output increases noticeably. The power output peak at a frequency of 1500 Hz corresponds with the resonant frequency for the 15mm PZT disk under these conditions. Above resonance frequency, power drops off the same as it did below resonant condition, so that above 3000Hz the power output is again less than $5x10^{-7}$ W for all acoustic pressures tested. The data shows that a peak power of 2.2 μW was produced at 1500 Hz with an acoustic pressure of 38.2 Pa.

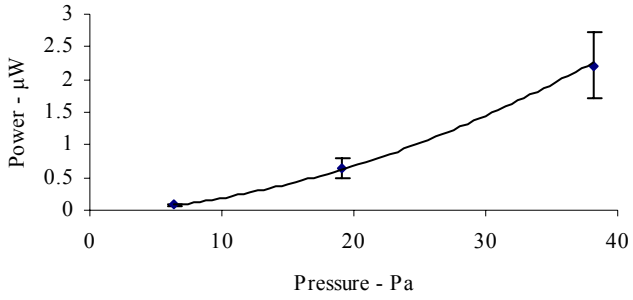

Figure 6.2.10 Pressure Response for PZT disk at resonant frequency

Figure 6.2.10 shows the power output for the PZT disk at 1500 Hz with increasing acoustic pressure amplitudes. The points represent the data collected experimentally. This pressure response curve shows how the PZT disk responds to changes in acoustic pressure. Using the least squares fit method referred to in Chapter 3 the solid line is obtained given by the following equation:

$$\Pi = 0.0026p^{1.9} \qquad (6.7)$$

Where Π is time averaged power in Watts and p is acoustic pressure in Pa. This result is indicative of the pressure response curves for the other frequencies tested. This equation shows that the PZT disk produces power proportional to a square of the acoustic pressure.

The PZT disk was then tested on the long closed TA engine operating at 470 Hz. The sample produced 177 μW of electric power at an acoustic pressure of 796 Pa. This was compared to the results from the sound tube as seen below.

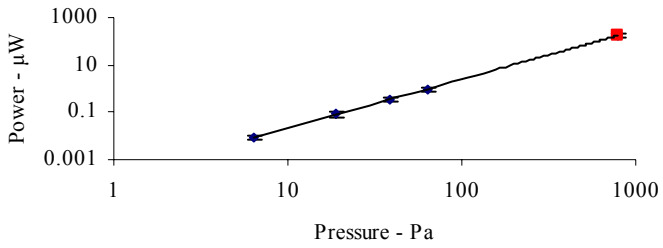

Figure 6.2.11 Pressure Response for PZT disk at 470 Hz

Figure 6.2.11 shows the power output for the PZT disk at 470 Hz on a logarithmic scale. This compares the experimental results from the open sound tube operating between 6.4 Pa and 64 Pa to the results from the open thermoacoustic engine operating at 796 Pa shown in red. As the graph shows, there is very good agreement between all of the values obtained.

All of the data points for the PZT disk were then plotted on a 3D mesh which shows the interpolation of power output for any combination of frequency and acoustic pressure within the dynamic range of the experimental setup. This is shown below.

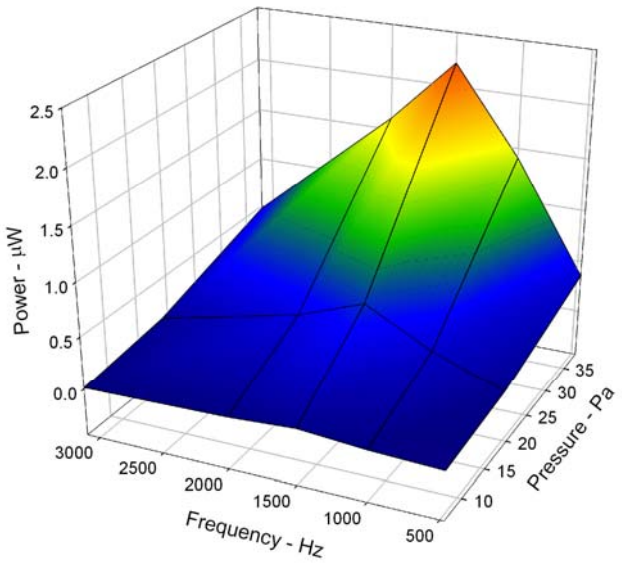

Figure 6.2.12 Power Output Plot for PZT disk closed conditions

As this plot shows, power output increases significantly as the driving frequency approaches the natural resonance of the sample, and as was previously stated the peak power of 2.2 µW was generated at a frequency of 1500 Hz, with an electrical load of 5 kΩ at an acoustic pressure of 38.2 Pa. This pressure is significantly less than the pressures generated in a closed thermoacoustic engine, but these results give a good indication of the power that can be obtained from an acoustic source. To extrapolate what may be expected by coupling the PZT disk to a closed standing wave thermoacoustic engine, the power output formula that was generated from the pressure response curves was used to generate a numerical model of power output for a wider range of pressures. This is shown in Section 5.

6.2.4 Closed PZT Bender

A cantilever of Lead Zirconate Titanate or simply PZT bender was fully constrained over the 10mm diameter opening, and power measurements were made with the variable load resistor. Under resonant conditions, it was found that peak power was produced with a 500 Ω load.

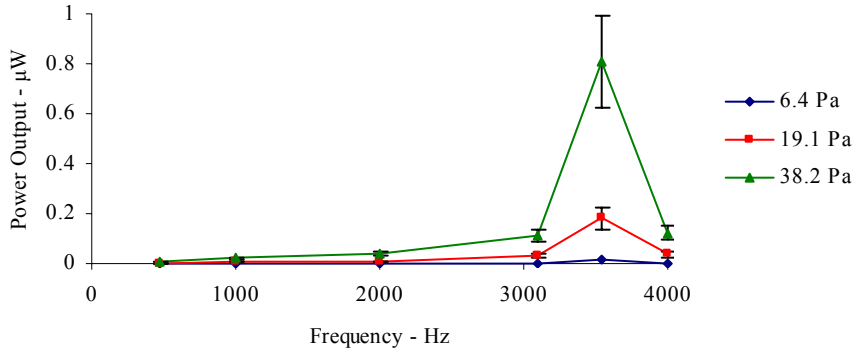

Figure 6.2.13 Frequency Response for PZT Bender closed conditions

Figure 6.2.13 shows the power output data for the PZT bender over a range of frequencies below and above resonance. As the graph shows, below 3000 Hz the sample produces less than $2x10^{-7}$ W for all acoustic pressures. From 3000-3450 Hz, power output increases noticeably. The power output peak at a frequency of 3450 Hz corresponds with the resonant frequency for the sample under these conditions. Above resonance frequency, power drops off the same as it did below resonant condition, so that above 4000 Hz the power output is again less than $2x10^{-7}$ W for all acoustic pressures tested. The data shows that a peak power of 0.8 µW was produced at 3540 Hz with an acoustic pressure of 38.2 Pa.

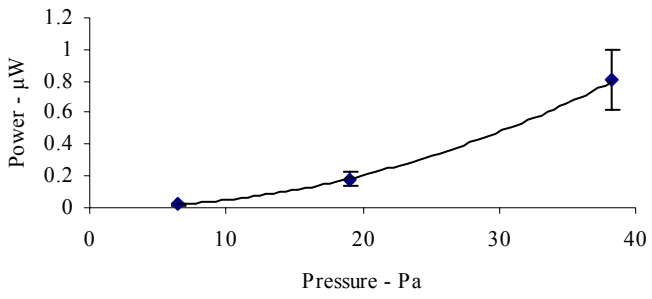

Figure 6.2.14 Pressure Response for PZT Bender at resonant frequency

Figure 6.2.14 shows the power output for the PZT bender at 3450 Hz with increasing acoustic pressure amplitudes. The points represent the data collected experimentally. This pressure response curve shows how the sample responds to changes in acoustic pressure. Using the least squares fit method referred to in Chapter 3 the solid line is obtained given by the following equation:

$$\Pi = 0.0004p^{2.09} \quad (6.8)$$

Where Π is time averaged power in Watts and p is acoustic pressure in Pa. This result is indicative of the pressure response curves for the other frequencies tested. This equation shows that the sample produces power proportional to a square of the acoustic pressure.

The PZT bender sample was then tested on the long closed thermoacoustic engine operating at 470 Hz. The sample produced 1.04 µW of electric power at an acoustic pressure of 726 Pa. This was compared to the results from the sound tube as seen below.

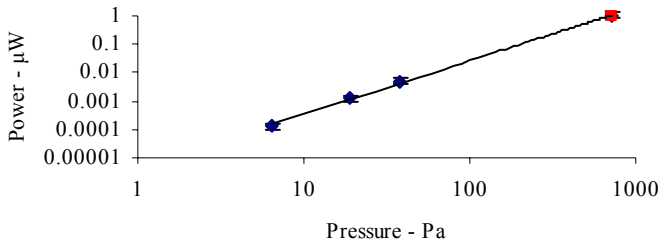

Figure 6.2.15 Pressure Response for PZT Bender at 470 Hz

Figure 6.2.15 shows the power output for the PZT bender at 470 Hz on a logarithmic scale. This compares the experimental results from the open sound tube operating between 6.4 Pa and 38.2 Pa to the results from the open thermoacoustic engine operating at 796 Pa shown in red. The graph shows good agreement between all values.

All of the data points for the PZT bender were then plotted on a 3D mesh which shows the interpolation of power output for any combination of frequency and acoustic pressure within the dynamic range of the experimental setup. This is shown below.

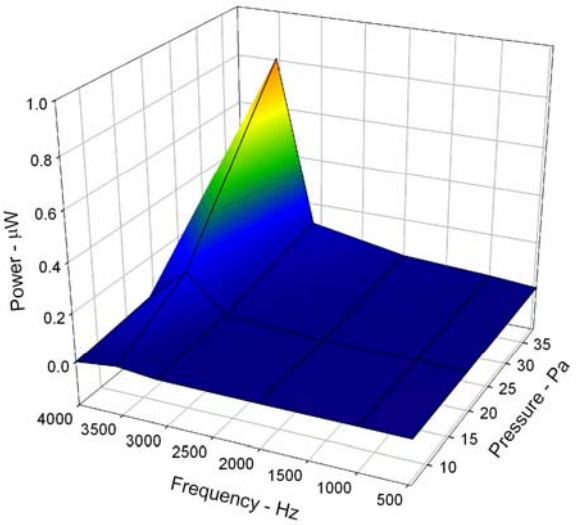

Figure 6.2.16 Power Output Plot for PZT Bender closed conditions

As this plot shows, power output increases significantly as the driving frequency approaches the natural resonance of the sample, and as was previously stated the peak power of 0.8 μW was generated at a frequency of 3450 Hz, with an electrical load of 500Ω at an acoustic pressure of 38.2 Pa RMS. This pressure is significantly less than the pressures generated in a closed thermoacoustic engine, but these results give a good indication of the power that can be obtained from an acoustic source. To extrapolate what may be expected by coupling the PZT sample to a closed standing wave thermoacoustic engine, the power output formula that was generated from the pressure response curves was used to generate a numerical model of power output for a wider range of pressures. This is shown in Section 5.

6.3 Power Density

For the purposes of comparing all of the samples, power output can be normalized by the area or volume of each sample and reported as a power density. Power density for thermoacoustic systems is reported as power per unit area and is given in units W/m^2. For power generation systems, power density is defined as power per unit volume and is given in units W/m^3. For this study, both power densities are reported. This simplifies comparison of the different samples and also facilitates comparison of these samples with other power generation methods.

6.3.1 Open Conditions

For the open sound tube, all samples were simply clamped as a cantilever on one edge. The opening of the sound tube was a larger cross sectional area than any of the

samples, so each sample had acoustic pressure incident on its entire area. To calculate power density for these conditions, it was recognized that power is only generated from the electrodes and so the electrode area is considered the active area. Based on this assumption, the electrode area and thickness was measured for each sample as reported in Chapter 4 and power density was calculated for all the samples at their resonant frequency with an RMS acoustic pressure of 38.2 Pa. This is shown in table 6.3.1.

Sample	Resonance	Volume	Power Output	Area Power Density	Volume Power Density
PFC	135 Hz	$6.9\text{x}10^{-8}$ m^3	0.50 μW	1.67 mW/m^2	4.17 W/m^3
PVDF	140 Hz	$5.5\text{x}10^{-8}$ m^3	12.0 μW	50 mW/m^2	250 W/m^3
PZT disk	230 Hz	$4.06\text{x}10^{-8}$ m^3	1.57 μW	8.88 mW/m^2	38.6 W/m^3
PZT bender	210 Hz	$1.52\text{x}10^{-7}$ m^3	9.07 μW	27.5 mW/m^2	44.3 W/m^3

Table 6.3.1 Power Density for open conditions at 38.2 Pa RMS

Table 6.3.1 shows the peak power output of all samples normalized by volume for the open condition sound tube. Here it is evident that the compliant PVDF sample does very well, generating 250 W/m^3 or nearly five times more power per volume than any other sample.

6.3.2 Closed Conditions

For the closed sound tube, all of the samples were constrained behind a 10mm diameter opening, and so the assumption was made that the incident acoustic power is restricted to this area. Based on this assumption, the area used for all samples under closed conditions is calculated as area = $\pi(0.005\text{m})^2 = 7.85\text{x}10^{-5}$ m^2 and the thickness was

measured for each sample as reported in Chapter 4. Using the calculated area and volume, the power density was calculated for all of the samples at their resonant frequency with an acoustic pressure of 38.1 Pa. This is shown in table 6.3.2.

Sample	Resonance	Volume	Power Output	Area Power Density	Volume Power Density
PFC	2000 Hz	1.81×10^{-8} m^3	8.49 nW	0.11 mW/m^2	0.27 W/m^3
PVDF	1000 Hz	1.57×10^{-8} m^3	44.4 nW	0.57 mW/m^2	2.83 W/m^3
PZT disk	1500 Hz	1.81×10^{-8} m^3	2.22 μW	28.3 mW/m^2	122.8 W/m^3
PZT bender	3100 Hz	4.87×10^{-8} m^3	0.808 μW	10.3 mW/m^2	16.6 W/m^3

Table 6.3.2 Power Density for closed conditions at 38.2 Pa

Table 6.3.2 shows the peak power output of all samples normalized by volume for the closed condition sound tube. Here the performance of the PZT disk is evident, generating 122.8 W/m^3 which is nearly 10 times the density of any other sample.

6.4 Efficiency Calculations

Another figure of merit for a transducer is the efficiency with which it can transfer power from one state to another. For this study, acoustic power is calculated and compared to electric power produced. From [6.1] the equation of acoustic power for a harmonic wave is used to derive the following formula:

$$\Pi = \frac{|\hat{p}|^2}{2}\left[\frac{S^2}{\psi^2}\right]\frac{\mathrm{Re}\left[\hat{Z}_e\right] + j\,\mathrm{Im}\left[\hat{Z}_e\right]}{\left|\hat{Z}_e\right|^2} \tag{6.9}$$

Where Π is time averaged acoustic power in Watts, $\hat{p}$ is acoustic pressure amplitude, $\hat{Z}_0$ is complex acoustic impedance of the transducer, ψ² is calculated for the transducer, S is

the area of the transducer and $\hat{Z}_e$ is the measured electric impedance of the transducer at resonance. Efficiency, η, is given as electric power output divided by acoustic power input multiplied by 100%. The derivation for equation 6.9 along with a more detailed analysis of the efficiency calculation is given in Appendix C. Calculations for all samples on the sound tube with open conditions are shown in Table 6.4.1.

	PZT disk	PZT bender	PVDF	PFC
Area - m^2	0.000177	0.00033	0.00024	0.00025
ψ^2	9.71×10^{-8}	3.36×10^{-7}	2.93×10^{-11}	2.61×10^{-11}
$\mathrm{Re}[\hat{Z}_e]$	3.76×10^{3}	1.33×10^{3}	4.63×10^{4}	6.93×10^{4}
$\lvert\hat{Z}_e\rvert$	2.03×10^{4}	9.38×10^{3}	1.28×10^{6}	2.08×10^{6}
$\Pi_{acoustic}$ - W	2.16×10^{-3}	9.98×10^{-5}	1.01×10^{-2}	7.84×10^{-4}
$\Pi_{electric}$ - W	1.57×10^{-6}	5.33×10^{-7}	3.74×10^{-6}	5.71×10^{-8}
Efficiency - %	0.073	0.534	0.037	0.0073

Table 6.4.1 Open conditions efficiency calculations

Table 6.4.1 shows the calculations of acoustic to electric efficiency for all samples on the open sound tube. The best result was for the PZT bender with a calculated efficiency of 0.5 %.

For closed conditions, it was assumed that the area of the incident acoustic pressure is restricted to the 10mm diameter opening and so area equals 7.85×10^{-5} m^2 for all samples. The incident acoustic power is calculated with the same formulas used for open conditions and efficiency is calculated by comparing electric power output to acoustic power input as before.

	PZT disk	PZT bender	PVDF	PFC
Area - m^2	$7.85x10^{-5}$	$7.85x10^{-5}$	$7.85x10^{-5}$	$7.85x10^{-5}$
ψ^2	$7.71x10^{-6}$	$1.19x10^{-5}$	$3.64x10^{-9}$	$1.34x10^{-8}$
$Re[\hat{Z}_e]$	$7.38x10^{2}$	$6.28x10^{1}$	$3.53x10^{3}$	$2.57x10^{3}$
$\lvert\hat{Z}_e\rvert$	$5.07x10^{3}$	$4.89x10^{2}$	$1.83x10^{5}$	$1.64x10^{5}$
$\Pi_{acoustic}$ - W	$4.70x10^{-7}$	$9.93\ x10^{-5}$	$1.30x10^{-4}$	$8.99x10^{-7}$
$\Pi_{electric}$ - W	$8.08x10^{-8}$	$8.08x10^{-7}$	$4.44x10^{-8}$	$3.06x10^{-10}$
Efficiency - %	17.186	0.814	0.034	0.034

Table 6.4.2 Closed conditions efficiency calculations

Table 6.4.2 shows the calculations of acoustic to electric efficiency for all samples on the closed sound tube. The best result was for the PZT disk with a calculated efficiency of 17.2 %.

6.5 Modeled Power Output

A simple numerical model was derived for all of the samples. This was constructed based on curve fitting the pressure response data from the sound tube for each sample as shown in Sections 1 and 2. This model was then used to extrapolate beyond the dynamic range of the experimental setup and predict what power output can be expected from a sample for a given thermoacoustic engine with known pressure and frequency. An optimized Hofler tube generates an acoustic pressure of 564 Pa RMS [6.3] so for this analysis, 600 Pa is chosen as the upper limit of the pressure amplitude in the model for open conditions. The closed long thermoacoustic engine produced 789 Pa RMS so 1000 Pa is chosen as the upper pressure limit for closed conditions.

6.5.1 Open Conditions

For the same conditions as the open sound tube, the modeled power output plots are shown below for acoustic pressures up to 600 Pa RMS.

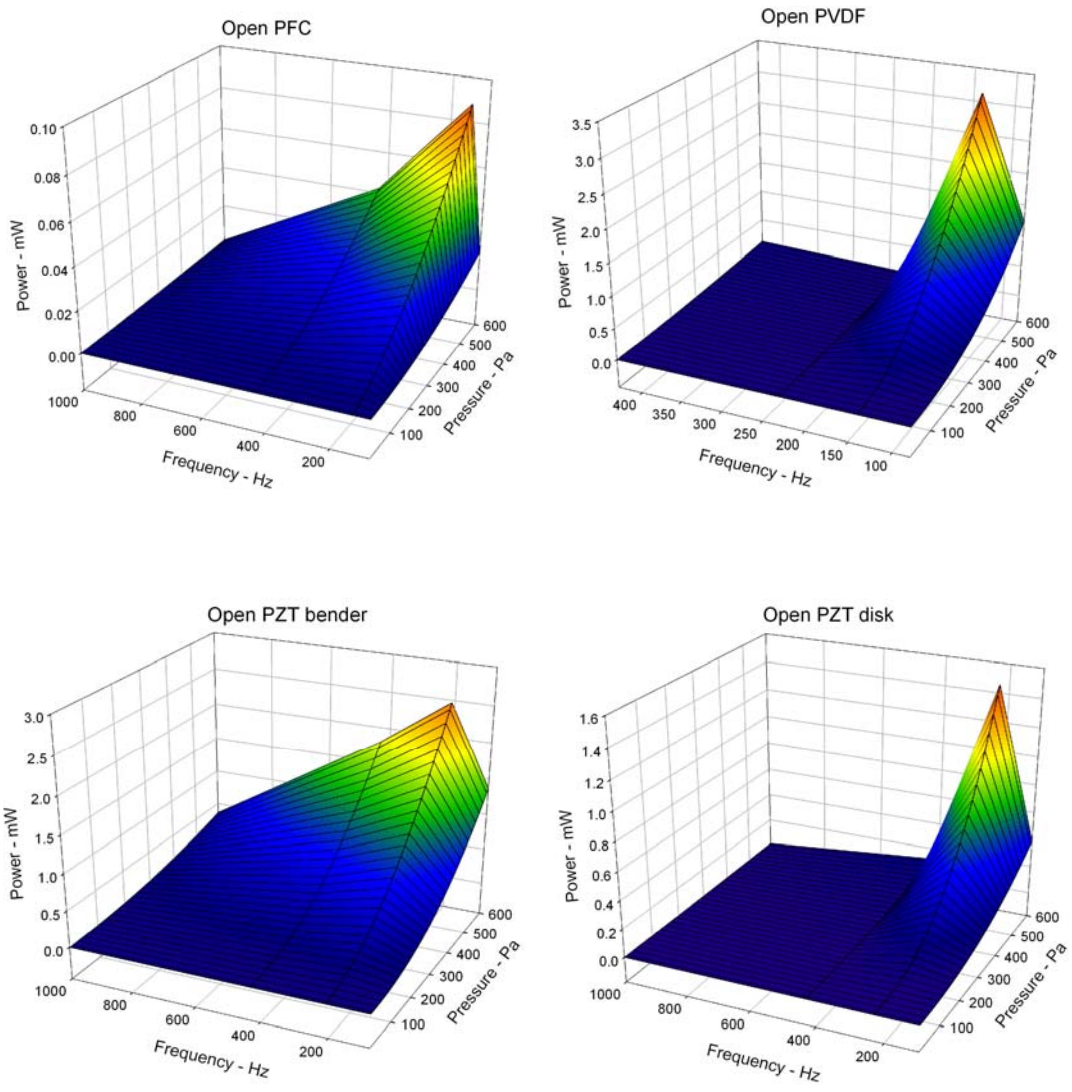

Figure 6.5.1 (a) (b) (c) (d) Modeled power output for Open conditions

As is seen in Figure 6.5.1, the power output for each sample has been extrapolated from the sound tube results to include acoustic pressures that are attainable using an open thermoacoustic engine. All of the samples except for the PFC should produce over 1mW of power at these acoustic pressures. The PVDF is expected to produce the most power from the experimental results and here it is projected to generate 3 mW at a frequency of 140 Hz and an acoustic pressure of 600 Pa RMS. Taking into account the experimental error, this calculation may be off by 23%, or ± 0.7 mW.

6.5.2 Closed Conditions

For the same conditions as the closed sound tube, the modeled power output plots are shown below for acoustic pressures up to 1000 Pa RMS.

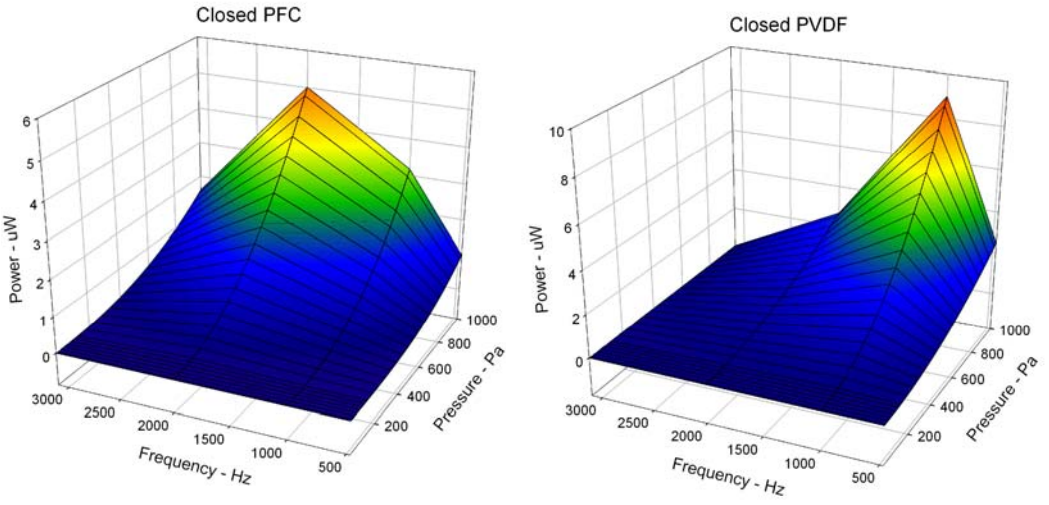

Figure 6.5.2 (a) (b) Modeled Power Output for closed conditions

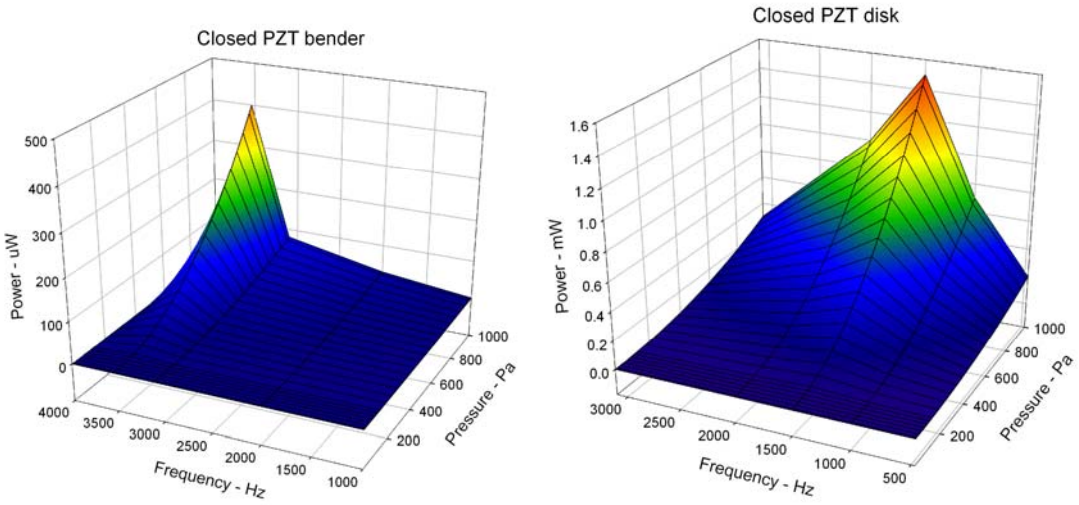

Figure 6.5.2 (c) (d) Modeled Power Output for closed conditions

As seen in Figure 6.5.2, the power output for each sample has been extrapolated from the sound tube results to include acoustic pressures that are attainable using a thermoacoustic engine. The PZT disk is expected to produce the most power from the experimental results and here it is projected to generate 1.5 mW at a frequency of 1500 Hz and an acoustic pressure of 1000 Pa RMS. Taking into account the experimental error, this calculation may be off by 23%, or ± 0.35 mW.

6.6 Comparison

As described in Chapter 2, all samples are fully characterized and the parameters are recorded below for comparison. These include the electrical parameters measured on the impedance analyzer, the electromechanical parameters calculated from the MATLAB code, the stiffness calculation performed and the other derived parameters that are calculated. All electrical and mechanical properties are tabulated, first for the open conditions and then for the closed conditions.

6.6.1 Properties

Sample	P3 PZT	PZT disk	PZT bender	PVDF	PFC
Area	5x5mm	15mm	11x30mm	12x20mm	10x30mm
Co – nF	27.427	20.814	93.819	0.832	0.504
R – kΩ	23.105	107.51	61.458	53436.0	70690.0
L – H	33.126	891.02	1919.3	962640	2885000
Cm - nF	0.0198	0.26304	0.78732	0.0018900	0.00038669
k^2	0.0007214	0.0125	0.0083	0.0014	0.0007663
f_n – Hz	6214.5	328.75	129.47	148.74	150.67
Q	55.98	17.12	25.4	16.84	38.64
$\bar{s}$ – N/m	881	258.7	253	15.5	67.6
S - m²	0.000025	0.00017671	0.00033	0.00024	0.0003
m – kg	5.78E-07	6.04E-05	2.2523E-04	1.77E-05	7.54E-05
b - kg/s	0.00040304	0.00768372	0.017598	0.00098488	0.001848
ψ^2- N^2/V^2	1.74E-08	9.71E-08	3.36E-07	2.93E-11	2.61E-11

Table 6.6.1 Comparison of samples for open conditions

Sample	P3 PZT	PZT disk	PZT bender	PVDF	PFC
Area	5x5mm	15mm	11x30mm	12x20mm	10x30mm
Co - nF	27.427	20.1	79.7	0.81	0.4802
R - kΩ	23.105	31.7	28.4	43597.0	10828.0
L - H	33.126	16.1169	4.3318	12628.0	5198.9
Cm - nF	0.0198	0.665	0.225	0.0020015	0.0014996
k^2	0.0007214	0.0319	0.0028	0.0025	0.0031
f - Hz	6214.5	1537.7	5102.7	1001.1	1802.5
Q	55.98	4.9137	4.8971	1.8219	5.4376
$\bar{s}$ - N/m	881	11600	53000	1820	8950
S - m²	0.000025	0.00017671	0.00033	0.00024	0.0003
m - kg	5.7783E-07	1.2427E-04	5.1560E-05	4.6000E-05	6.9777E-05
b - kg/s	0.00040304	0.24434	0.33756	0.15881	0.14533
ψ^2 - N^2/V^2	1.7444E-08	7.7102E-06	1.1903E-05	3.6427E-09	1.3421E-08

Table 6.6.2 Comparison of samples for closed conditions

Table 6.6.1 shows the properties for all samples with open conditions. Table 6.6.2 shows the properties for all samples with closed conditions. As described in Chapter 3, all of the electrical and mechanical properties are listed for comparison.

6.6.2 Sound Tube Peak Power Output

To facilitate comparison of the power output for all samples, the results are summarized below. Each sample is reported at the apparent resonant frequency for those conditions along with the electromechanical coupling coefficient, the quality factor and the stiffness, and all are reported at an acoustic pressure of 38.2 Pa RMS.

Sample	Frequency	k^2	Q	Stiffness	Power	Density
PFC	135 Hz	0.00077	38.64	67.6 N/m	0.50 μW	8.33 W/m^3
PVDF	140 Hz	0.0014	16.84	15.5 N/m	12.0 μW	250 W/m^3
PZT disk	333 Hz	0.0125	17.12	253 N/m	1.57 μW	38.6 W/m^3
PZT bender	210 Hz	0.0083	25.40	258.7 N/m	9.07 μW	44.3 W/m^3

Table 6.6.4 Comparison of power output at 38.2 Pa RMS open conditions

Table 6.6.4 reports the peak power output for all samples on the open sound tube at 38.2 Pa RMS and the power density as calculated in Section 3. The PVDF has the greatest power output of all samples at 12.0 μW and the highest power density of 250 W/m^3 despite having the lowest quality and second lowest coupling. It would appear that the compliance (low stiffness) of the PVDF enables it to perform so well. It is interesting that the PZT bender generates nearly as much power at 9.07 μW as the PVDF despite having the highest stiffness. This may be due to a high quality and a relatively high coupling.

Sample	Frequency	k^2	Q	Stiffness	Power	Density
PFC	2000 Hz	0.0031	5.4376	8950 N/m	8.49 nW	0.54W/m^3
PVDF	1000 Hz	0.0025	1.8219	1820 N/m	44.4 nW	2.83 W/m^3
PZT disk	1500 Hz	0.0319	4.9137	11600 N/m	2.22 μW	122.8 W/m^3
PZT bender	3450 Hz	0.0028	4.8971	53000 N/m	0.8 μW	1.66 W/m^3

Table 6.6.5 comparison of power output at 38.2 Pa RMS closed conditions

Table 6.6.5 reports the peak power output for all samples on the closed sound tube at 38.2 Pa RMS and the power density as calculated in Section 3. The PZT disk has the greatest power output of all samples at 2.22 μW and the greatest power density of 122.8 W/m^3. It would appear that the high coupling coefficient of the PZT disk enables it to perform so well and there does not appear to be a correlation between stiffness and power for these conditions. It should be noted that the PZT disk is the only sample specifically designed to operate under these fully clamped conditions, which may lead to the high coupling.

6.6.3 Thermoacoustic Engine Power Output

Two of the demonstration thermoacoustic engines were chosen as representative of two possible thermoacoustic setups as described in Chapter 2. In addition, an experimental small-scale standing wave thermoacoustic engine was tested [6.2]. All samples were tested for power output using these thermoacoustic engines as the prime mover as described in Chapter 3. Results are shown in Table 6.6.3.

TA engine	Frequency	Pressure	PFC	PVDF	PZT disk	PZT bender
Closed long	470 Hz	796 Pa	1.88 μW	0.98 μW	177 μW	1.04 μW
Open large	430 Hz	89 Pa	0.54 μW	2.30 μW	1.17 μW	0.56 μW
Open short	1250 Hz	62 Pa	43.2 nW	0.14 μW	0.16 μW	0.89 μW
Open long	830 Hz	60 Pa	32.0 nW	58.3 nW	0.23 μW	45.1 nW

Table 6.6.3 Power output comparison for thermoacoustic engines

Table 6.6.3 reports the power output for all samples on each of the thermoacoustic engines. The PZT disk generates the most power with a maximum of 177 μW. This is two orders of magnitude larger than any other power output reported. The PZT disk generated more power than all of the other samples on each of the engines. It should be noted that the closed thermoacoustic engine generated nearly ten times the RMS acoustic pressure of the open engines. It should also be noted that none of the resonant frequencies of the samples matched with the operating frequencies of the thermoacoustic engines used for this test. It is left for a future study to match these resonant frequencies.

6.7 Discussion

The results show some interesting trends in performance and properties between the open and closed conditions. The mechanical quality factor Q is significantly lower for closed conditions for all samples. The coupling coefficient k^2 is improved in the PZT disk and the PVDF for closed conditions, but otherwise is decreased in the closed condition. The mechanical damping b, the stiffness $\bar{s}$ and the resonant frequency f_n is increased for all samples in the closed condition. Despite generating less power in general for the closed conditions, the efficiency of transducing acoustic to electric power was increased

for all samples but PVDF for those closed conditions. These results show the need for future investigations as outlined below in Section 8.

For open conditions on the sound tube, the PVDF sample gives the largest total power output of 12.0 μW at 38.2 Pa RMS with a power density of 250 W/m^3. This indicates that the most compliant piezoelectric material is the best choice for acoustic transduction. However, for closed conditions on the sound tube, the PZT sample gives the largest total power output of 2.22 μW at 38.2 Pa RMS with a power density of 122.8 W/m^3 despite being stiffer than other samples. This indicates that the highest coupling coefficient is the best choice for these conditions. It should also be noted that the PZT sample is the only sample in the study designed to be fully clamped which favors the closed condition. All other samples are designed to be operated as a simply clamped cantilever which corresponds to the open condition.

The peak power output from the thermoacoustic engines was the long closed engine operating at 470 Hz and 796 Pa RMS. The PZT disk coupled to this produced 177 μW of power. This closed engine was operating at an acoustic pressure nearly ten times that of the open engines.

Power output for a piezoelectric transducer coupled to a thermoacoustic engine operating at the resonant frequency of the transducer can be predicted from the experimental data.

One open thermoacoustic engine in the literature is the optimized Hofler tube. This is an open standing wave engine which generates acoustic power at an SPL of 149 dB which equals 564 Pa RMS [6.3]. The PVDF sample coupled to this engine would produce approximately 2.77 mW of electrical power at 140 Hz. Further, this engine has a

flared opening 42mm in diameter for an area of 1385mm^2. If the PVDF sample covered that total area, then the total power output would be 5.77 times greater which would produce 16 mW. Taking into account the experimental error, this calculation may be off by 23%, or ± 3.7 mW.

The closed thermoacoustic engine operates at 796 Pa RMS. The PZT disk operating at resonance and coupled to this engine would produce approximately 647 μW of electrical power at 1500 Hz. This calculation may be off by ± 148.8 μW.

6.8 Limitations and Future Study

It should be noted that this study was focused only on characterization of these samples. It has been left for a future study to optimize the operating conditions for the coupling of a thermoacoustic engine and a piezoelectric transducer. One parameter to optimize would be resonant frequency matching. The resonant frequency of the thermoacoustic engines are strongly correlated to their geometry, so it is conceivable to design and build an engine to match the resonant frequency of a given piezoelectric sample. Another more difficult parameter to optimize would be impedance matching of the engine to the transducer.

Additionally, the area of the samples should be optimized along with optimization of operating conditions. Most of the samples can be ordered by a specific size and geometry and some can be modified by the user. This size and shape should closely match the engine to maximize the incident acoustic power. For example, for closed conditions the electrode area should be circular with a 10mm diameter to match the opening. It is also important to remove excess electrode area as this will reduce the

parasitic capacitance of the sample. In addition, the closed clamping conditions were chosen for convenience to be used in this study. It is left for future work to design and implement a better clamping system for closed conditions that would maintain the mechanical quality factor Q that is present in the open clamping conditions, which should improve the coupling coefficient k^2 and lead to increases in power output and efficiency.

One more important point is to note that all samples exhibited additional resonances at higher frequencies. For this study, only the fundamental frequency was characterized and tested for power output. However, as thermoacoustic engine sizes are reduced to smaller length scales, they will have operating frequencies in the kilohertz range and so it is noted that these samples may be found to have resonance frequencies to match those engines. This is another area for future study.

6.9 References

[6.1] L. Kinsler, A. Frey, A. Coppens and J. Sanders, Fundamentals of Acoustics Fourth Edition, 2000

[6.2] N. Shafiei-Tehrany Masters thesis WSU Development of small-scale thermoacoustic engine and thermoacoustic cooling demonstrator (2008)

[6.3] T. Hofler and J. Adeff, An Optimized miniature Hofler tube Acoustics Research Letters Online Vol. 2(1) pp 37-42 (2001)

CHAPTER 7

CONCLUSIONS

This study presents four piezoelectric candidates for generating electric power from small scale thermoacoustic engines. First, piezoelectric materials are chosen to represent a range of stiffness and electromechanical properties. Those samples are tested to characterize their electrical and mechanical parameters. Each sample is then driven by an acoustic device over a range of frequencies and acoustic pressures. Power output is measured for each sample for this range of conditions to determine maximum power output. Three thermoacoustic engines are also employed to generate power with each sample. These results are shown to correlate with the power output data from the sound tube. All results are tabulated to facilitate prediction of power output for any sample under given conditions.

The materials chosen for consideration are bulk lead zirconate titanate, or PZT, in both disk and bender configurations, polyvinylidene fluoride, or PVDF, and piezoelectric fiber composite, or PFC. PZT is chosen for its high quality and coupling, PVDF is chosen for its high compliance, and PFC is chosen as a hybrid of these characteristics. One sample of each material is fully characterized for all electrical and mechanical properties with both open and closed conditions.

7.1 Properties

For open conditions, the samples have the following defining characteristics: the 10x30mm PFC has a resonant frequency f_n of 135 Hz, an electromechanical coupling

coefficient k^2 of 0.00077, a mechanical quality factor Q of 38.64, and a stiffness of 67.6 N/m; the 12x20mm PVDF has a f_n of 140 Hz, k^2 of 0.0014, Q of 16.84, and a stiffness of 15.5 N/m; the 15mm PZT disk has a f_n of 333 Hz, k^2 of 0.0125, Q of 17.12, and a stiffness of 253 N/m; the 11x30mm PZT bender has a f_n of 210 Hz, k^2 of 0.0083, Q of 25.40, and a stiffness of 258.7 N/m.

For closed conditions, the samples have the following defining characteristics: the 10x30mm PFC has a f_n of 2000 Hz, k^2 of 0.0031, Q of 5.4376, and a stiffness of 8950 N/m; the 12x20mm PVDF has a f_n of 1000 Hz, k^2 of 0.0025, Q of 1.8219, and a stiffness of 1820 N/m; the 15mm PZT disk has a f_n of 1500 Hz, k^2 of 0.0319, Q of 4.9137, and a stiffness of 11600 N/m; the 11x30mm PZT bender has a f_n of 3100 Hz, k^2 of 0.0028, Q of 4.8971, and a stiffness of 53000 N/m.

7.2 Power Output

All samples are also tested on the acoustic sound tube to determine frequency and pressure response. At resonant frequency of the sample, maximum electrical power output is calculated for open and closed conditions.

For open conditions, the samples generate the following power at an acoustic pressure of 38.2 Pa RMS: the 10x30mm PFC at 135 Hz generates 0.5 μW, the 12x20mm PVDF at 140 Hz generates 12 μW, the 15mm PZT disk at 230 Hz generates 1.57 μW, and the 11x30mm PZT bender at 210 Hz generates 9.07 μW.

For closed conditions, the samples generate the following power at an acoustic pressure of 38.2 Pa RMS: the 10x30mm PFC at 2000 Hz generates 8.49 nW, the

12x20mm PVDF at 1000 Hz generates 44.4 nW, the 15mm PZT disk at 1500 Hz generates 2.22 μW, and the 11x30mm PZT bender at 3100 Hz generates 0.11 μW.

All samples are also tested on an open standing wave thermoacoustic engine to calculate the power output. The samples generate the following power at a frequency of 430 Hz and an acoustic pressure of 89 Pa RMS: the 10x30mm PFC generates 0.54 μW, the 12x20mm PVDF generates 2.3 μW, the 15mm PZT disk generates 18.9 μW, and the 11x30mm PZT bender generates 0.56 μW.

All samples are also tested on a closed standing wave thermoacoustic engine to calculate the power output. The samples generate the following power at a frequency of 470 Hz at an acoustic pressure of 796 Pa RMS: the 10x30mm PFC generates 1.88 μW, the 12x20mm PVDF generates 0.98 μW, the 15mm PZT disk generates 177 μW, and the 11x30mm PZT bender generates 1.04 μW.

7.3 Best Results

From the data, the best results from each setup are identified and correlated with the defining property of that sample. These are reported below.

For open conditions, the most compliant sample generates the highest power output. On the open sound tube, the PVDF generates 12 μW at 38.2 Pa RMS with a power density of 250 W/m^3. Interestingly the stiffest sample, PZT bender, is a close second by producing 9.07 μW. This is likely due to its high coupling.

For closed conditions, the sample with the highest coupling generates the highest power output. On the closed sound tube, the PZT disk generates 2.22 μW at 38.2 Pa RMS with a power density of 122.8 W/m^3 and an acoustic to electric efficiency of 17.2%. The

PZT disk also generates the most power from the closed thermoacoustic engine by producing 177 μW at 470 Hz and 796 Pa RMS.

The results show some interesting trends in the properties between the open and closed conditions. The mechanical Q is significantly lower for closed conditions for all samples. The coupling coefficient k^2 is higher for the closed conditions for the PZT disk and the PVDF samples but lower for the other samples. The stiffness, resonant frequency, and damping of all samples are significantly higher in the closed conditions.

7.4 Future Work

It has been left for a future study to optimize the operating conditions for the coupling of a thermoacoustic engine and a piezoelectric transducer. This can include matching the resonant conditions and the impedance for the engine and the transducer and improving the clamping method for both open and closed conditions.

Another area for future study is a characterization of all samples at higher frequencies and acoustic pressures. The limitation of the experimental setup and the error in the measurements leads to an incomplete understanding of how the samples will perform under very high frequencies and pressures.

APPENDIX A

Error Analysis

Accuracy of instruments

Digital multimeter Fluke 189 for AC voltage measurements:

Resolution: 0.001mV at 50mV, 0.01mV at 500mV, and 0.1mV at 5V

Accuracy: 0.4% at 45-1000 Hz, 5% at 1-10kHz

Fluke 189 has 10MΩ internal resistance for voltage measurements

All data from Fluke Model 187 & 189 Users Manual Rev. 2, June 2002

Oscilloscope GDS-2000 accuracy (3% x readout + 0.05 div x volts/div + 0.8mV)

TDS 220 3% (4% at 2-5mV)

Bruel and Kjaer Microphone 4134 has a calibrated accuracy of 1.5dB = 1.88 V/Pa

Decade Resistor Box AEMC BR07 accuracy 1%

Error analysis for power measurement

The formula to calculate power is the following:

$$P = \frac{V^2}{R} \tag{A.1}$$

$$(\Delta P)^2 = \left(\frac{\partial P}{\partial V}\Delta V\right)^2 + \left(\frac{\partial P}{\partial R}\Delta R\right)^2 \tag{A.2}$$

$$\Delta P = \sqrt{\left(2\frac{V}{R}\Delta V\right)^2 + \left(-\frac{V^2}{R^2}\Delta R\right)^2} \tag{A.3}$$

Where ΔV is the resolution of the voltage measurement and ΔR is the resolution of the resistance measurement. This is the weighted average of the errors of V and R.

For the power measurements voltage was measured on the Fluke 189 but the readings were truncated due to fluctuations in the signal. For this analysis, ΔV is assumed to be 1mV. The resistance used was the AEMC BR07 decade box which has an accuracy of 1% so for this analysis, ΔR is calculated as 1% of the resistance of the measurement (ex. 1% of 100kΩ gives ΔR of 1000Ω). Sample error calculation for PVDF at $4.4x10^{-8}$ W is shown in Table A.1.

ΔV	ΔR	ΔP	% error
0.001 V	1000 Ω	9.58044E-10 W	2.16

Table A.1 Error calculation for power measurement

There were other experimental uncertainties which were much more difficult to quantify. For example, all samples for open conditions were securely clamped on a fixture set at 4mm from the sound tube opening. The samples themselves however had some angle to them and so the actual distance from the opening varied by 0.5mm, or roughly 10%. There were also pressure and frequency fluctuations in the source signal. It was observed that pressures would vary on the order of 1.44 Pa for the 19.1 Pa reading and 2.7 Pa for the 38.2 Pa reading. This is roughly 7.5% and 7% respectively. This variability in the source signal had an influence on the power produced by the samples which was hard to measure directly so a repeatability test was conducted. The PFC sample was used with

open conditions and data was taken on three different days to determine experimentally how much variation the signal variation and the distance variation had on the measurements. The measured results are shown below.

Pa	Test 1	Test 2	Test 3	Average	Std dev	% error
6.4	2.31E-08	2.84E-08	1.78E-08	2.31052E-08	5.32E-09	23.01
19.1	8.99E-08	1.35E-07	1.35E-07	1.19717E-07	2.58E-08	21.53

Table A.2 Experimental measurement error

Table A.2 shows the measured power output for PFC for three tests taken. The average, standard deviation and percent error is calculated. From these results, it is found that experimental error is between 21-23%. It is assumed for this analysis that this calculated error is representative of all of the samples. To calculate total error a weighted average of the two errors is taken.

$$\Delta E = \sqrt{\Delta P^2 + StdDev^2} \tag{A.4}$$

From this formula, total experimental error is calculated to be 23.1%. This value is used for all samples.

APPENDIX B

Power Calculation

Power is measured in all tests by attaching the sample to a variable load resistor (decade box) and measuring the voltage across the sample as seen in Figure B.1.

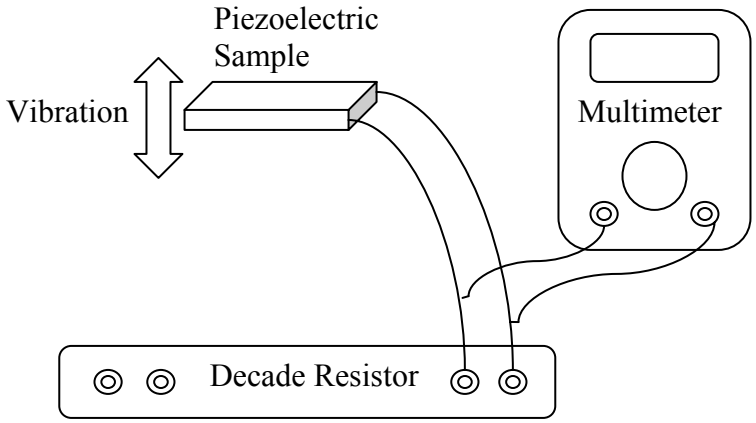

Figure B.1 Schematic of power measurement

The sample to be tested is fixed in the experimental setup and the electric leads are attached to the decade box. The Fluke 189 True RMS multimeter is then attached in parallel to measure the voltage generated by the sample with the given load.

The sound tube or thermoacoustic engine is turned on to give a driving signal to the sample and the change in AC RMS voltage output from ambient is measured. To calculate the power produced, the formula is derived from Ohm's law V=IR and the power law P=VI [B.1]. By manipulating and substitution of the equations, this becomes the following:

$$P = \frac{V_{rms}^2}{R} \tag{B.1}$$

Here P is electric power in Watts, V_{rms} is voltage in Volts and R is resistance in Ohms. With the known resistance and the measured RMS voltage, power is calculated. Because the Fluke 189 multimeter has an internal resistance of 10 MΩ and was used in parallel with the decade box to measure the voltage, the total resistance is adjusted for this parallel resistor [B.1].

$$\frac{1}{R_{total}} = \frac{1}{R_{load}} + \frac{1}{R_{meter}} \tag{B.2}$$

The error of these measurements is also calculated. The decade box has an accuracy of 1% and the multimeter has an accuracy of 0.4%. Because of the fluctuations in the voltage readings from the sample, the measurements were generally truncated and rounded to the nearest 1mV. Based on these numbers and using a weighted average formula, error is calculated for each sample. The formula to calculate power is given by equation B.1. Where V is the voltage measurement and R is the resistance measurement.

Figure B.2 shows a sample graph of calculated power output with varying load resistance. This graph is for PVDF on the open conditions sound tube at an acoustic pressure of 7 Pa. This graph is representative of the other samples power output curves.

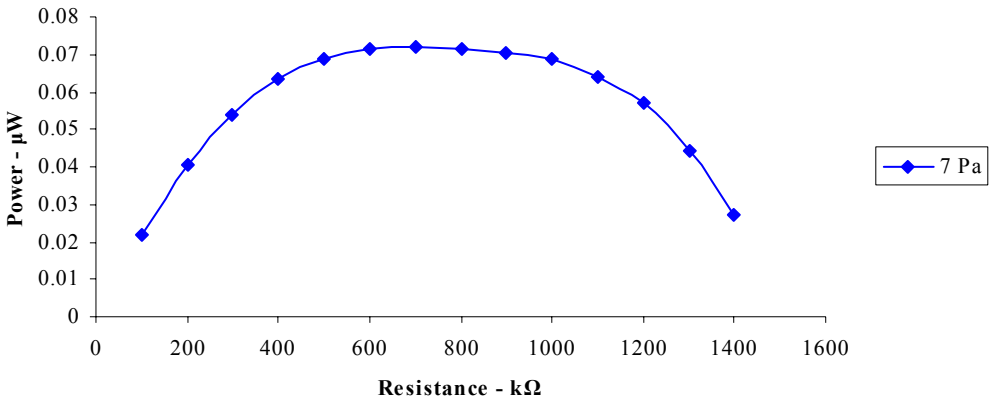

Figure B.2 Power output with varying load resistance

As is seen in Figure B.2 as the load resistance is increased, power (V^2/R) increases to a maximum, after which it decreases. For each sample at a given frequency and acoustic pressure, the peak power output was calculated.

References

[A.1] T. Trick, Introduction to Circuit Analysis, John Wiley & Sons, 1977

APPENDIX C

Efficiency Calculation

One figure of merit for a transducer is the efficiency with which it can transfer power from one state to another. For this study, acoustic power is generated by a sound tube that is designed and fabricated to generate plane waves. Piezoelectric transducers of various materials are placed normal to the acoustic waves with an incidence of zero degrees in the acoustic field. A B&K 4134 microphone is used to measure the acoustic field. Acoustic power is calculated and compared to electric power produced. From Fundamentals of Acoustics by Kinsler et al, the equation of acoustic power for a standing acoustic field is:

$$\Pi = \frac{1}{2}\mathrm{Re}\left[\hat{p}\hat{U}\right] \qquad \text{where} \qquad \hat{Z}_0 = \frac{\hat{p}}{\hat{U}} \tag{C.1}$$

Some rearranging and algebra give:

$$\Pi = \frac{\left|\hat{p}\right|^2}{2}\mathrm{Re}\left[\frac{1}{\hat{Z}_0}\right] \qquad \hat{Z}_0 = \frac{\psi^2}{S^2}\hat{Z}_e \qquad \frac{1}{\hat{Z}_0} = \frac{S^2}{\psi^2\hat{Z}_e} = \frac{S^2}{\psi^2}\left[\frac{\mathrm{Re}\left[\hat{Z}_e\right]}{\left|\hat{Z}_e\right|^2} - j\frac{\mathrm{Im}\left[\hat{Z}_e\right]}{\left|\hat{Z}_e\right|^2}\right] \tag{C.2}$$

$$\Pi = \frac{\left|\hat{p}\right|^2}{2}\left[\frac{S^2}{\psi^2}\right]\frac{\mathrm{Re}\left[\hat{Z}_e\right]}{\left|\hat{Z}_e\right|^2} \tag{C.3}$$

Where Π is time averaged acoustic power in Watts, $\hat{p}$ is acoustic pressure amplitude, $\hat{Z}_0$ is the complex acoustic impedance of the transducer, ψ² is calculated for the transducer, S is the area of the transducer and $\hat{Z}_e$ is the measured electric impedance of the transducer. Efficiency is given as electric power output divided by acoustic power input multiplied by 100%.

$$\eta = \frac{\Pi_{out}}{\Pi_{in}} * 100\% \qquad \text{(C.4)}$$

For the PZT disk with open conditions,

$\mathrm{Re}[\hat{Z}_e] = 3.76\text{x}10^{3}$

$|\hat{Z}_e| = 2.03\text{x}10^{4}$

$\psi^2 = 9.71\text{x}10^{-8}$

$S = 0.000177\ \mathrm{m}^2$

$\hat{p} = 38.2$ Pa

Then acoustic power is calculated as $\Pi = 0.00216$ W

Measured electric power is $1.57\text{x}10^{-6}$ W so efficiency is 0.073%

One concern is the power radiated beyond the transducer as an outward traveling acoustic wave. A simple energy balance for the system gives: total power in is equal to the total power out which consists of electric power out, acoustic power out and losses.

$$Total\ \Pi_{in} = Total\ \Pi_{out} = \Pi_{electric} + \Pi_{acoustic} + \Pi_{losses} \qquad \text{(C.5)}$$

Total power input is the incident acoustic power calculated. Electric power is calculated, acoustic power output can be calculated and the difference will be assumed to be mechanical and conversion losses in the transducer.

From Kinsler, we can model the transducer as a simple source if ka<<1 and λ>>2a. Using the plane piston approximation for a simple source and with a measurement of the pressure amplitude, we can calculate the source velocity and then acoustic power from:

$$p(r,t) = j\rho_o c\, U_o \frac{a}{r} ka\, e^{j(\omega t - kr)} \qquad \text{which becomes} \qquad U_o = \frac{|\hat{p}|\, r}{\rho_o c\, ka^2} \tag{C.6}$$

$$\Pi = \frac{1}{2}\rho_o c\, U_o^2 4\pi a^2 \frac{(ka)^2}{(ka)^2 + 1} \tag{C.7}$$

Measurements of the pressure amplitude are made at 5mm and 130mm from the transducer. For the PVDF sample, measurements and calculations are made for an incident acoustic field of f = 140 Hz at 6.4 Pa RMS and 19.1 Pa RMS (at the transducer). For an incident field of 6.4 Pa RMS, at 5mm behind the transducer, acoustic pressure was measured to be 4.4 Pa RMS and at a distance of 130mm, the acoustic pressure was 0.5 Pa RMS. For the PVDF sample, an effective radius (a) is calculated using the area 240mm^2 so a = 8.74mm. To show that simple source assumptions are met, calculations are made and it is found that λ=2.45m and ka = 0.022, which satisfy the criteria. The medium is air, so ρ_o=1.21 kg/m^3 and c=343m/s. Now the source velocity can be calculated. For r=5mm, U_o=0.2757m/s and for r=130mm, U_o=1.12787m/s. Now acoustic power can be calculated. For r=5mm, Π=7.32 μW and for r=130mm, Π=0.1226 mW. Acoustic power radiated from a simple source should be a constant, but in this case the discrepancy can be attributed to acoustic power escaping past the transducer from the sound tube and also reflected acoustic waves from the bench and walls.

These results show that the outward traveling acoustic field is two orders of magnitude less than the incident acoustic field, and so the loss of acoustic power due to radiated sound from the transducer is considered negligible for the efficiency calculations.

Efficiency calculations for all samples for open conditions are shown below.

	PZT disk	PZT bender	PVDF	PFC
Area – m^2	0.000177	0.00033	0.00024	0.00025
Ψ^2	9.71×10^{-8}	3.36×10^{-7}	2.93×10^{-11}	2.61×10^{-11}
$\mathrm{Re}[\hat{Z}_e]$	3.76×10^{3}	1.33×10^{3}	4.63×10^{4}	6.93×10^{4}
$\lvert\hat{Z}_e\rvert$	2.03×10^{4}	9.38×10^{3}	1.28×10^{6}	2.08×10^{6}
$\Pi_{acoustic}$ – W	2.16×10^{-3}	9.98×10^{-5}	1.01×10^{-2}	7.84×10^{-4}
$\Pi_{electric}$ – W	1.57×10^{-6}	5.33×10^{-7}	3.74×10^{-6}	5.71×10^{-8}
Efficiency - %	0.073	0.534	0.037	0.0073

Figure C.1 Open conditions efficiency calculations

Figure C.1 shows the calculations of acoustic to electric efficiency for all samples on the open sound tube. The best result is the PZT bender with a calculated efficiency of 0.5 %.

For closed conditions, it is assumed that the area of the incident acoustic pressure is restricted to the 10mm diameter opening and so area equals 7.85×10^{-5} m^2 for all samples. The incident acoustic power is calculated the same as for open conditions, and efficiency is calculated by comparing electric power to acoustic power as before.

	PZT disk	PZT bender	PVDF	PFC
Area – m^2	$7.85x10^{-5}$	$7.85x10^{-5}$	$7.85x10^{-5}$	$7.85x10^{-5}$
Ψ^2	$7.71x10^{-6}$	$1.19x10^{-5}$	$3.64x10^{-9}$	$1.34x10^{-8}$
$Re[\hat{Z}_e]$	$7.38x10^{2}$	$6.28x10^{1}$	$3.53x10^{3}$	$2.57x10^{3}$
$\lvert\hat{Z}_e\rvert$	$5.07x10^{3}$	$4.89x10^{2}$	$1.83x10^{5}$	$1.64x10^{5}$
$\Pi_{acoustic}$ – W	$4.70x10^{-7}$	$9.93\ x10^{-5}$	$1.30x10^{-4}$	$8.99x10^{-7}$
$\Pi_{electric}$ – W	$8.08x10^{-8}$	$8.08x10^{-7}$	$4.44x10^{-8}$	$3.06x10^{-10}$
Efficiency - %	17.186	0.814	0.034	0.034

Figure C.2 Closed conditions efficiency calculations

Figure C.2 shows the calculations of acoustic to electric efficiency for all samples on the closed sound tube. The best result is the PZT disk with an efficiency of 17.2 %.

An efficiency of 17% for energy harvesting is quite good, but it is left for future study to improve on the accuracy of this calculation and discover where the energy losses occur.

APPENDIX B

MATLAB CODE FOR ELECTRICAL PARAMETERS

%Original code by Dirk Robinson%

```
clc
clear

function [Co,R,L,Cm]=freq_impedance()

%Load impedance file data
[FILENAME, PATHNAME]=uigetfile('*.*','Choose impedance file');
fid=fopen([PATHNAME, FILENAME]);
while ~strcmp(fscanf(fid,'%s',[1,1]),'POINTS:')
end
N=fscanf(fid,'%d"',[1,1]);
while ~strcmp(fscanf(fid,'%s',[1,1]),'"Frequency"')
end
S=fgetl(fid);
A=zeros(N,2);
for r=(1:N)
   A(r,:)=fscanf(fid,'%f',[1,2]);
   fgetl(fid);
end
%Defines variables for each column of data (frequency and impedance)
f=A(:,1);
Zm=A(:,2);

%First guess at the parameters
plot(f,Zm)
%user clicks resonant frequency on graph to give program starting point
[X,Y]=ginput(1);
fr=X(length(X));
Zr=Y(length(Y));
%Equivalent circuit parameters defined which help to make the best fit
R=8e3;
Co=1/(2*pi*fr)*sqrt(1/Zr^2-1/R^2);
Rs=7.5;
w=2*pi*f;
L=400;
Cm=1/(4*pi^2*L*fr^2);
%L=value that gives minimum value between Z and Zm
min_diff=inf;
for R=logspace(1,8,50)%logspace(min 10^,max 10^ ,num points per 10^1)
   for L=logspace(1,8,50)%logspace(min,max,num)
    Cm=1/(4*pi^2*L*fr^2);
        Co=1/(2*pi*fr)*sqrt(1/Zr^2-1/R^2);
    Z=abs(1./(1./(R+i*w*L-i./w./Cm)+i*w*Co)+Rs);
    if sum((Z-Zm).^2)<min_diff;
        min_diff=sum((Z-Zm).^2);
         min_R=R;
         min_L=L;
    end
   end
```

```
end
L=min_L;
Cm=1/(4*pi^2*L*fr^2);
R=min_R;
Co=1/(2*pi*fr)*sqrt(1/Zr^2-1/R^2);
Z=abs(1./(1./(R+i*w*L-i./w./Cm)+i*w*Co)+Rs);

%Plot of fit over data curve
plot(f,abs(Z),f,Zm)
%Functions called to improve fit
p=zeros(4,5);
p(:,1)=[Co R L Cm]';
p(:,2)=p(:,1)+.01*[Co 0 0 0]';
p(:,3)=p(:,1)+.01*[0 R 0 0]';
p(:,4)=p(:,1)+.01*[0 0 L 0]';
p(:,5)=p(:,1)+.01*[0 0 0 Cm]';

y=zeros(1,5);
y(1)=fun(p(:,1),Rs,Zm,w);
y(2)=fun(p(:,2));
y(3)=fun(p(:,3));
y(4)=fun(p(:,4));
y(5)=fun(p(:,5));

function y=fun(p,varargin)
persistent Rs Zm w
if nargin==4
    Rs=varargin{1};
    Zm=varargin{2};
    w=varargin{3};
end
Co=p(1);
R=p(2);
L=p(3);
Cm=p(4);
Z=abs(1./(1./(R+i*w*L-i./w./Cm)+i*w*Co)+Rs);
y=sqrt(sum((Zm-Z).^2)/length(Zm));

function [pmin,nfunk]=amoeba(p,y,ndim,ftol,funk)
NMAX=500000;
ALPHA=1.0;
BETA=0.5;
GAMMA=2.0;
psum=sum(p')';  %all points added together
nfunk=0;  %number of function evaluations
mpts=ndim+1;
ilo=1;
ihi=mpts;
inhi=mpts-1;

while 1
   [y,I] = sort(y);  %sorts points into ascending order
   p=p(:,I);         % by function value

   %computes the range from highest to lowest
   rtol=2.0*abs(y(ihi)-y(ilo))/(abs(y(ihi))+abs(y(ilo)));
```

```
   if (rtol<ftol)
      break
   end

   %reflect
   [ytry,p,y,psum,nfunk]=amotry(p,y,psum,ndim,funk,ihi,nfunk,-ALPHA);
   if(ytry<=y(ilo)) %extend
      [ytry,p,y,psum,nfunk]=amotry(p,y,psum,ndim,funk,ihi,nfunk,GAMMA);
   elseif (ytry>=y(inhi))
      ysave=y(ihi);
      [ytry,p,y,psum,nfunk]=amotry(p,y,psum,ndim,funk,ihi,nfunk,BETA);
%contract
      if(ytry>=ysave)
         for i=1:mpts %contract all about lowest point
            if(i~=ilo)
               p(:,i)=0.5*(p(:,i)+p(:,ilo));
               y(i)=feval(funk,p(:,i));
            end
         end
         nfunk=nfunk+ndim;
        psum=sum(p')';
      end
   end
end
pmin=p(:,ilo);

function
[ytry,p,y,psum,nfunk]=amotry(p,y,psum,ndim,funk,ihi,nfunk,fac);
fac1=(1.0-fac)/ndim;
fac2=fac1-fac;
ptry=psum*fac1-p(:,ihi)*fac2;
ytry=feval(funk,ptry);
nfunk=nfunk+1;
if(ytry<y(ihi))
   y(ihi)=ytry;
   p(:,ihi)=ptry;
    psum=sum(p')';
end

[pmin,nfunk]=amoeba(p,y,4,1e-10,'fun');

%Output variables
nfunk
Co=pmin(1)
R=pmin(2)
L=pmin(3)
Cm=pmin(4)
k2=Cm/(Co+Cm)
fr=1/(2*pi*sqrt(L*Cm))
Qe=2*pi*fr*L/R

Z=1./(1./(R+i*w*L-i./w./Cm)+i*w*Co)+Rs;
%Final plot showing best fit over curve
plot(f,abs(Z),f,Zm)
```

APPENDIX E

MATLAB Code for comparison of experimental to numerical

%Original code written by Dr. Konstantin Matveev%

```
%function y = impedance(r);

clc
clear

%impedance

load impedancebimorph.mat
%create variables f Zr Zi
%electrical, measured
Zr = Zr;
Z = Zr+i*Zi;
Za = abs(Z);
Zf = angle(Z);
F = f;

figure(1)
subplot(311)
plot(F,Zr)
xlabel('Frequency [Hz]')
ylabel('Re[Z_e_x_p]')
subplot(312)
plot(F,Zi)
xlabel('Frequency [Hz]')
ylabel('Im[Z_e_x_p]')
subplot(313)
plot(F,Zf/pi*180)
xlabel('Frequency [Hz]')
ylabel('Phase[Z_e_x_p], deg')

F1 = 130:1:200; %frequency - Hz
w = 2*pi*F1;
%parameters in vacuum
b = .017598; %damping coefficient - kg/s
m = 2.252e-4; %effective mass - kg
s = 253; %stiffness - N/m
c = 9.3098e-08; %Co
ps2 = 3.36465e-07; %psi squared

wr = sqrt(s/m);
fr = wr/2/pi

%mechanical
Z1 = i*w*m+b+s/i./w;
Z1r = real(Z1);
Z1i = imag(Z1);
Z1f = angle(Z1);
Z1m = abs(Z1);
```

```
%electrical, modeled
ZL = Z1./(i*w*c.*Z1+ps2);
ZLr = real(ZL);
ZLi = imag(ZL);
ZLf = angle(ZL);
ZLm = abs(ZL);

%with air loading
c0 = 343;%speed of sound in air
k = w/c0;
rh = 1.21;%density of air
a = 0.00033; %area of sample
A = a;

n = length(w);
for j = 1:n,
    x = 2*k(j)*a;
    J1 = besselj(1,x);
    J0 = besselj(0,x);
    H1 = 2/pi-J0+(16/pi-5)*sin(x)/x+(12-36/pi)*(1-cos(x))/x^2;
    Zp(j) = rh*c0*(1-J1/x*2+i*2*H1/x);
    x1(j) = x;
    R1(j) = 1-J1/x;
    R2(j) = 1-J1/x*2;
    X1(j) = -2*H1/x;
    X2(j) = 2*H1/x;
end

k1 = 1;
ZE = (Z1+k1*Zp*A)./(i*w*c.*(Z1+k1*Zp*A)+ps2);
ZEr = real(ZE);
ZEi = imag(ZE);
ZEf = angle(ZE);
ZEm = abs(ZE);

figure(2)
subplot(211)
plot(F,Za,F1,ZLm,F1,ZEm)
xlabel('Frequency - Hz')
ylabel('Mag[Z] - Ohm')
subplot(212)
plot(F,Zf/pi*180,F1,ZLf/pi*180,F1,ZEf/pi*180)
xlabel('Frequency - Hz')
ylabel('Phase[Z] - deg')
```